The Use of Cylinder Pressure for Estimation of the In-Cylinder Air/Fuel Ratio of an Internal Combustion Engine

by

Per Anders Tunestal

CIVIN (Lund University, Sweden) 1993

A dissertation submitted in partial satisfaction of the
requirements for the degree of
Doctor of Philosophy

in

Engineering-Mechanical Engineering

in the

GRADUATE DIVISION
of the
UNIVERSITY OF CALIFORNIA, BERKELEY

Committee in charge:

Professor John Karl Hedrick, Chair
Professor Andrew K. Packard
Professor Pravin P. Varaiya

2000

The Use of Cylinder Pressure for Estimation of the In-Cylinder Air/Fuel Ratio of an Internal Combustion Engine

Copyright 2000
by
Per Anders Tunestal

Abstract

The Use of Cylinder Pressure for Estimation of the In-Cylinder Air/Fuel Ratio of an Internal Combustion Engine

by

Per Anders Tunestal

Doctor of Philosophy in Engineering-Mechanical Engineering

University of California, Berkeley

Professor John Karl Hedrick, Chair

This thesis investigates the use of cylinder pressure for estimating the in-cylinder air/fuel Ratio in a spark ignited internal combustion engine.

An estimation model which uses the net heat release profile for estimating the cylinder air/fuel ratio of a spark ignition engine is developed. The net heat release profile is computed from the cylinder pressure trace and quantifies the conversion of chemical energy of the reactants in the charge into thermal energy. The net heat release profile does not take heat- or mass transfer into account. Cycle-averaged air/fuel ratio estimates over a range of engine speeds and loads show an RMS error of 4.1 % compared to measurements in the exhaust.

A thermochemical model of the combustion process in an internal combustion engine is developed. It uses a simple chemical combustion reaction, polynomial fits of internal energy as function of temperature, and the first law of thermodynamics to derive a relationship between measured cylinder pressure and the progress of the combustion process. Simplifying assumptions are made to arrive at an equation which relates the net heat release to the cylinder pressure.

Two methods for estimating the sensor offset of a cylinder pressure transducer are developed. Both methods fit the pressure data during pre-combustion compression to a polytropic curve. The first method assumes a known polytropic exponent, and the other estimates the polytropic exponent. The first method results in a linear least-squares problem, and the second method results in a nonlinear least-squares problem. The nonlinear

least-squares problem is solved by separating out the nonlinear dependence and solving the single-variable minimization problem. For this, a finite difference Newton method is derived. Using this method, the cost of solving the nonlinear least-squares problem is only slightly higher than solving the linear least-squares problem. Both methods show good statistical behavior. Estimation error variances are inversely proportional to the number of pressure samples used for the estimation.

To my wife,

Christina,

who has put up with me even though this little report took a little longer to produce than expected.

Contents

List of Figures

Acknowledgements

I have many people to thank for finally being able to produce this thesis, which has been hanging over my head as a dark cloud for several years now.

Professors Rolf Johansson and Gunnar Lundholm, my advisors back in the Swedish days, are responsible for putting me here in the first place. They brought to my attention the possibility of applying for a scholarship, from the Swedish Research Council for Engineering Sciences. A scholarship, which I was subsequently awarded. Said generous scholarship supported me during the major part of my studies here at UC Berkeley.

My advisor Karl Hedrick was kind enough to accept me as his student, and has since, provided me with guidance and financial means for performing the work that eventually led to this thesis.

My coworkers Mark Wilcutts, Albert Lee, Gerry Fischer, and Byron Shaw have all contributed with something unique and valuable.

Mark has put a lot of time into setting up the engine test cell. He has also been very valuable as the ultimate skeptic. Whenever I think I have the idea that is going to revolutionize the world, I first have to explain it to Mark, and if he doesn't "buy it" then it probably won't work.

Albert has shared the programming load with me, and we have been able to exchange ideas on this subject to allow faster progress.

Gerry brought a lot of good ideas (and engine parts) from Darmstadt. His extensive experience with engine testing has been very useful.

Byron's experience with engines was very valuable in the initial planning of the test cell.

Ford Motor Company was generous enough to provide us with an engine, and some money to go with it.

Jan-Ola Olsson let me participate in his HCCI project in Lund, just as things were starting to come together. We had a very productive fall.

I could make the list even longer ...

Chapter 1

Introduction

1.1 Short History of Automotive Engine Pollution and Control

During the course of the past six decades, the internal combustion engine has been under ever tighter scrutiny, regarding its role as a major source of air pollution. The smog problem due to automobile traffic was first observed in the early 1940s in the Los Angeles basin. In 1952 Haagen-Smit [18] showed that the smog problems in Los Angeles were caused by reactions between oxides of nitrogen and hydrocarbon compounds in the presence of sunlight. It was later concluded that the oxides of nitrogen and the hydrocarbons, causing the photochemical smog, originated from combustion in automotive engines.

In 1959, the state of California legislature took, as a consequence of the smog problems in Los Angeles, the first legislative steps towards a reduction of the automotive air pollution, by setting emissions standards for automotive engines [27]. The state of California initiative was followed, first by the federal government of the United States, then by Japan, Europe, and the rest of the world. Ever since this first initiative, the state of California has been leading the way, in terms of setting ever stricter standards on vehicle pollutant emissions.

The two-way catalytic converter (oxidizing catalytic converter) was introduced in 1975 as a means of reducing tail-pipe emissions of hydrocarbons and carbon monoxide. In 1976 Volvo introduced its "smog-free" 1977 model year car, as the first car featuring a three-way catalytic converter (oxidizing/reducing catalytic converter), able to drastically reduce

tail-pipe emissions of all three controlled pollutants; hydrocarbons, carbon monoxide, and oxides of nitrogen.

The introduction of the three-way catalytic converter (TWC) caused a revolution in the combustion engine industry and research community. In order to get high conversion efficiency for all three pollutants, the ratio of the masses of air and fuel in the combustion chamber has to stay within a very narrow band surrounding the stoichiometric ratio (just enough oxygen to oxidize all the fuel). The carburetor, which had thus far been used to meter the amount of fuel going in to the cylinders, proved to be insufficient for such accurate Air/Fuel-Ratio (AFR) control.

The introduction of the Exhaust Gas Oxygen sensor (EGO), and Electronic Fuel Injection (EFI) provided a means of solving this problem. The EGO provided the necessary feedback about whether the engine was operating under lean (not enough fuel) or rich (too much fuel) conditions. The EFI system could then compensate for this, by adjusting the rate of fuel injection to the cylinders. AFR control with the purpose of reducing pollutant emissions has been an active research topic ever since.

1.2 The State of The Art of Cylinder-Pressure Based Control of Internal Combustion Engines

1.2.1 Thermodynamic Modeling of Combustion in Internal Combustion Engines

The first attempt at a cylinder-pressure based model of combustion in an internal combustion engine was made by Rassweiler and Withrow in 1938 [42]. They develop an empirical model, which states that the amount of mass burnt, is proportional to the difference between the measured cylinder pressure, and the cylinder pressure obtained from polytropic compression/expansion. This model was the standard model for computing mass fraction burnt for 50 years.

In [2], Blizard and Keck use thermodynamics, a turbulence model, and chemical kinetics to predict the flame propagation in a spark-ignition engine. The predictions are compared with cylinder pressure measurements, and ionization current sensors throughout the combustion chamber detecting the flame propagation.

In [15], a one-zone model based on the first law of thermodynamics is used to

compute the heat release in a spark-ignition engine from crank-angle resolved cylinder pressure measurements. In the analysis, it is assumed that the specific internal energy of the charge is a function of temperature only. The conversion of chemical energy into thermal energy by combustion, is considered as a separate heat-addition process, and the cylinder-gas composition is modeled as being constant during the whole cycle.

1.2.2 Cylinder-Pressure Offset Estimation

Existing methods of estimating the sensor offset in cylinder-pressure measurements (pressure pegging) can be divided into two groups; methods which require an additional absolute pressure reference, and methods which utilize the polytropic compression curve. These methods are compared in [41].

Additional Absolute Pressure Reference Methods

The idea behind these methods is that during some part of the cycle, the pressure in the intake manifold and the pressure in the cylinder are equal. Thus, the method is to take an average of a number of consecutive pressure measurements near this point in the cycle, and compare them to an averaged pressure measurement in the intake manifold at the same time. Since the pressures should be equal, the sensor offset can be determined.

One problem associated with this method is how to determine at which point in the cycle the pressures are equal. This will most likely have to be done experimentally over the whole load/speed range of the engine, which would be most time consuming. Another drawback with the approach, if cost is an issue, is that it requires another sensor. The sensor has to be reasonably high bandwidth also, since it has to resolve the relevant part of the cycle.

Polytropic Compression Methods

These methods utilize the fact that the part of the compression stroke of a four-stroke engine after the intake valve has closed, and before combustion has started, is accurately represented by a polytropic compression curve.

There are two existing methods, both described in [41], one which uses a fixed polytropic exponent, and one which uses a varying polytropic exponent. Both methods use two pairs of matching values of cylinder pressure and combustion chamber volume, and fit

a polytropic compression curve to these values. Polytropic compression can be defined by

$$pV^{\kappa} = p_0 V_0^{\kappa} = C \tag{1.1}$$

where κ is the polytropic exponent, and C is a constant during the compression process. Now if the sensor measurement is denoted p_m, and the offset is denoted Δp, the cylinder pressure can be expressed as

$$p = p_m - \Delta p \tag{1.2}$$

Combine (1.1) and (1.2) to yield

$$(p_m - \Delta p)V^{\kappa} = C \tag{1.3}$$

Assuming κ is known, there are two unknowns, Δp and C. These unknowns can be precisely determined using two matching pairs of pressure/volume measurements.

When using a time-varying polytropic exponents, the value of κ is usually assumed to be a function of charge composition and temperature.

A drawback with this method is that it relies on only two pressure measurements, and fits an exponential curve to them. Thus, as will be shown in chapter 5, the noise present in these measurements will be present in the estimates of C and Δp also. In fact, the variance of the Δp estimate will be slightly higher than the variance of the pressure measurements. In this case, since the volume is constantly changing during compression, one cannot use an average of consecutive measurements to reduce the noise level either.

1.2.3 Cylinder-Pressure Based AFR Estimation

Cylinder-Pressure Moment Approach

Gilkey and Powell [16], develop an empirical relationship between various moments of crank-angle resolved cylinder-pressure traces and cylinder AFR. Changes in input variables (engine speed, throttle angle, EGR, and AFR) are correlated with changes in the output (cylinder pressure). Pattern recognition is then applied to obtain a relationship between cylinder pressure moments and AFR.

Molecular Weight Approach

In [39], Patrick and Powell develop a model-based method of estimating AFR from cylinder-pressure measurements. The model relies on the fact that the number of

moles in the cylinder increases with combustion. The ratio of the number of moles before and after combustion can be obtained from cylinder pressure and temperature before and after combustion by applying the ideal gas law. Indeed, if $i = 1$ denotes before combustion, and $i = 2$ after combustion, the ideal gas law dictates

$$p_i V_i = n_i \tilde{R} T_i, \qquad i = 1, 2 \tag{1.4}$$

Then, if pressure and temperature are collected symmetrically about the Top Dead Center (TDC), $V_1 = V_2$. Dividing the two equations yields

$$\frac{n_1}{n_2} = \frac{p_1 T_2}{p_2 T_1} \tag{1.5}$$

Now, since the mass in the cylinder stays the same throughout compression, combustion, and expansion, this ratio is the same as the ratio of average molecular weights after compared to before combustion.

$$\frac{M_2}{M_1} = \frac{m/n_2}{m/n_1} = \frac{n_1}{n_2} \tag{1.6}$$

Now, since the average molecular weights of burned and unburned charge at chemical equilibrium, are functions of AFR [19], the AFR can be determined.

Equivalent Heat Release Duration Approach

Leisenring and Yurkovich [32] take an approach similar to Gilkey and Powell [16], when they correlate cylinder AFR with the Equivalent Heat Release Duration (EHRD). The EHRD is extracted from the zeroth and first crank-angle moments, Q and M, of the cylinder-pressure based heat release profile as

$$\text{EHRD} = \frac{M}{Q} \tag{1.7}$$

The EHRD is interpreted as the crank angle at which instantaneous release of Q Joules of heat would result in a heat release moment of M, and is thus a measure of the combustion duration.

The EHRD is correlated with cylinder AFR through experiments, and an empirical AFR-estimation model is obtained.

1.3 Contributions and Thesis Outline

In this thesis three different problems, all related to using cylinder pressure measurements for internal-combustion engine control, are addressed. First, a thermodynamic model, which includes a simple chemical model of the combustion process is derived. Then, the inherent problem of unknown, and time-varying sensor offsets, when measuring cylinder pressure is addressed, and methods are derived which estimate this offset. Finally, an estimation model which estimates cylinder Air/Fuel Ratio from cylinder-pressure measurements is derived.

1.3.1 Thermodynamic Modeling of Combustion in Internal Combustion Engines

Chapter 4 develops a thermodynamic model of the combustion process in an internal combustion engine. The model is a one-zone model, which means it assumes homogeneous conditions throughout the combustion chamber.

The model uses a simple chemical reaction which describes the combustion, polynomial fits of the internal energy of the components as function of temperature [44], and the first law of thermodynamics, to relate the progress of combustion to measured cylinder pressure. It is shown that using this model as opposed to a model which does not include the chemistry [15], can make a significant difference when estimating the mass fraction burned.

Simplifications of the model for control purposes are suggested and motivated.

1.3.2 Cylinder-Pressure Offset Estimation

Chapter 5 derives a new method to estimate the unknown and time-varying offset always present in cylinder pressure measurements. This offset is an undesirable property, which all pressure transducers, suitable for cylinder pressure measurement share. The method utilizes the fact that the equation for polytropic compression depends linearly on pressure offset and reference state, and derives the linear least-squares solution for these parameters based on an arbitrary number of cylinder pressure measurements during the compression stroke. The method is in fact a generalization of the polytropic-compression based method presented in [41] for more than two measurements, and it is shown that in the presence of measurement noise, the variances of the estimates drop drastically with the number of measurements.

Solving the least-squares problem requires knowledge of the polytropic exponent, which also varies with time, and operating conditions. An analytic expression for the least-squares loss function, as a function of the polytropic exponent is derived. Analytic expressions for the first and second derivatives are also derived, which would technically allow the usage of the Newton method for finding the minimum of the loss function. The second derivative is however, computationally, too expensive for use in a real-time application. Consequently, a finite difference Newton method is derived. Superlinear convergence is proved, and verified experimentally.

The statistical properties of this method are investigated by simulation. It is found that the variances of the estimates are quite high when estimating all three parameters simultaneously, and therefore it is suggested that a low-pass filtered version of the κ estimate is used for the offset estimation.

The method presented in chapter 5 can actually be applied to any nonlinear least-squares problem, for which the residual is affine with respect to all variables but one, and the total derivative of the least-squares loss function with respect to this variable is known.

1.3.3 Cylinder-Pressure Based AFR Estimation

Chapter 6 develops a model for cylinder-pressure based AFR estimation. It is shown, subject to some assumptions on flame geometry, that the cylinder AFR is proportional to the heat-release rate during the rapid burn phase of combustion in a Spark Ignition (SI) engine. A flame-speed model is incorporated into the model to account for changes in intake pressure, temperature, and engine speed. Experimental data is used for parameter identification and model validation. The RMS error of averaged AFR estimates is 4 %, which is slightly better than the result in [39]. The quantitative AFR feedback provided by the estimator can be used for individual cylinder AFR control as well as control of AFR during cold-starting conditions, when the exhaust gases are too cold for the EGO.

This estimator has the advantage over the pressure-moment based estimator, [16], and the EHRD estimator, [32], of being based on a physical model. This means that its applicability to a different kind of engine can be predicted.

An advantage compared to the molecular weight model [39] is that it is equally sensitive over the whole operating range of air/fuel ratios of the engine. The molecular weight model suffers from the fact that the dependence of the burned-gas molecular weight

on AFR is very weak for air/fuel ratios lean of stoichiometric. Furthermore, the AFR dependence of the unburned-gas molecular weight is very weak over the whole operating range. An AFR increase of 25 % from stoichiometric results in a 1.3 % increase in molecular weight ratio, and a 29 % decrease in AFR from stoichiometric results in a 9 % drop in molecular weight ratio. This results in a large variance in the estimate around stoichiometric AFR, which is exactly where a more accurate estimate is desired.

Chapter 2

Internal Combustion Engine Basics

2.1 Introduction

This chapter introduces some basic concepts relating to reciprocating internal-combustion engines. Knowledge of these concepts will be assumed in later chapters. The treatment in this text is limited to four-stroke cycle engines

2.2 Heat Engines

A heat engine converts thermal energy to mechanical work, by letting a work fluid go through a thermodynamic cycle. This involves coordinated heat transfer and volume change of the work fluid. The simplest type of heat engine accepts heat from a high-temperature reservoir, outputs mechanical work, and expels waste heat to a low-temperature reservoir (see figure 2.1). An example of a heat engine is the Stirling engine.

A combustion engine is a heat engine in which the thermal energy is produced by combustion. Here, the chemical energy of the fuel is converted to thermal energy which powers the heat engine. A steam engine is an example of a combustion engine.

An internal-combustion (IC) engine is a combustion engine in which the combusting mixture of fuel and oxidant (usually air) acts as the work fluid. This necessarily involves a flow of fresh fuel-oxidant mixture into the engine, and a flow of exhaust out of the engine. A gas turbine provides an example of an internal combustion engine.

A reciprocating internal-combustion engine utilizes a cylinder-piston-crank arrangement (see figure 2.2) in order to, for each cycle, draw a fresh batch of fuel-oxidant

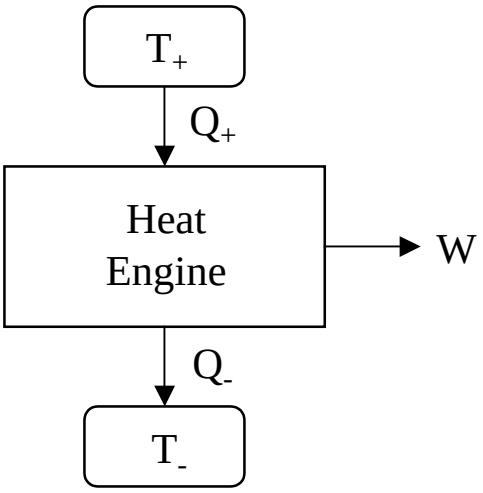

Figure 2.1: Schematics of a simple heat engine. The engine accepts Q_+ J of heat from the thermal reservoir at T_+ K, and expels Q_- J of heat to the thermal reservoir at T_- K. The engine outputs $W = Q_+ - Q_-$ Nm of mechanical work.

mixture, have it undergo combustion, and then push the exhaust out. Some important examples of reciprocating internal-combustion engines are Otto-cycle (Spark-Ignition) engines, Diesel-cycle engines, and Homogeneous-Charge Compression-Ignition (HCCI) engines.

2.3 Engine Geometry

The basic geometry of a reciprocating internal-combustion engine is shown in figure 2.2. The figure includes cylinder, piston, crank shaft, and connecting rod, and most geometric and kinematic properties of the engine can be derived from this simple schematics.

2.3.1 Piston Position and Speed

Piston Position

The vertical position of the piston is completely determined by the crank angle α. This section derives an expression for the vertical piston position as a function of crank angle. Subsequently this expression is used to derive an expression for the instantaneous piston speed.

The cosine theorem can be applied to the triangle formed by the connecting rod,

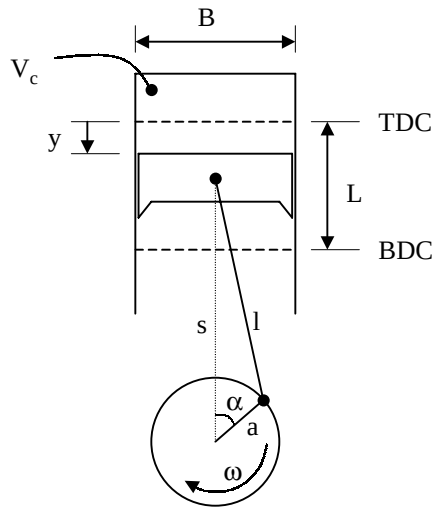

Figure 2.2: Basic geometry of a reciprocating internal-combustion engine, with B=Bore, L=Stroke, l=Connecting rod length, V_c=Clearance volume, a=Crank radius, and α=Crank angle.

the crank, and the vertical line connecting the piston bolt and the center of the crank shaft.

$$l^2 = s^2 + a^2 - 2as\cos(\alpha) \tag{2.1}$$

Rearranging and completing squares yields

$$l^2 - a^2 + a^2\cos^2(\alpha) = s^2 - 2a\cos(\alpha)\cdot s + a^2\cos^2(\alpha) \tag{2.2}$$

Applying the trigonometric identity to the left-hand side, and collecting the square on the right-hand side yields

$$l^2 - a^2\sin^2(\alpha) = (s - a\cos(\alpha))^2 \tag{2.3}$$

Now, an expression for s can be obtained by taking square roots and rearranging

$$s = a\cos(\alpha) \pm (l^2 - a^2\sin^2(\alpha))^{1/2} \tag{2.4}$$

where only the positive square root makes sense, since the negative square root renders a negative s. Thus,

$$s = a\cos(\alpha) + (l^2 - a^2\sin^2(\alpha))^{1/2} \tag{2.5}$$

Now, the vertical piston position relative to the Top Dead Center (TDC) can be expressed as

$$z = l + a - s \tag{2.6}$$

Thus, using (2.5)

$$z(\alpha) = l + a(1 - \cos(\alpha)) - (l^2 - a^2 \sin^2(\alpha))^{1/2} \tag{2.7}$$

Piston Speed

The instantaneous piston speed, v_p, is given by

$$v_p = \frac{\mathrm{d}z}{\mathrm{d}t} = \frac{\mathrm{d}z}{\mathrm{d}\alpha}\frac{\mathrm{d}\alpha}{\mathrm{d}t} = \frac{\mathrm{d}z}{\mathrm{d}\alpha}\omega_e \tag{2.8}$$

where ω_e is the crank shaft angular velocity. Now using (2.7)

$$\begin{aligned}\frac{\mathrm{d}z}{\mathrm{d}\alpha} &= a\sin(\alpha) - \frac{1}{2}(l^2 - a^2\sin^2(\alpha))^{-1/2} \cdot [-2a^2\sin(\alpha)\cos(\alpha)] \\ &= a\sin(\alpha)\left[1 + a\cos(\alpha)(l^2 - a^2\sin^2(\alpha))^{-1/2}\right]\end{aligned} \tag{2.9}$$

2.3.2 Combustion Chamber Volume

At TDC, the volume of the combustion chamber is the clearance volume, V_c. For any other crank position, the combustion chamber volume is the sum of the clearance volume and a cylindrical volume with diameter B and height y. So, the combustion chamber volume can be expressed as a function of the crank angle

$$V(\alpha) = V_c + \frac{\pi B^2}{4} z(\alpha) \tag{2.10}$$

The difference between the maximum and the minimum combustion chamber volume is called the displacement volume, V_d, and is given by

$$\begin{aligned}V_d = V(\pi) - V(0) &= \left(V_c + \frac{\pi B^2}{4} z(\pi)\right) - \left(V_c + \frac{\pi B^2}{4} z(0)\right) \\ &= \left(V_c + \frac{\pi B^2}{4} \cdot 2a\right) - V_c = \frac{\pi B^2}{4} \cdot 2a = \frac{\pi B^2}{4} L\end{aligned} \tag{2.11}$$

where L is the stroke.

The derivative of the combustion chamber volume with respect to crank angle can now be calculated by differentiating (2.10) with respect to α

$$\frac{\mathrm{d}V}{\mathrm{d}\alpha} = \frac{\pi B^2}{4} \cdot 2z\frac{\mathrm{d}z}{\mathrm{d}\alpha} = \frac{\pi B^2}{2} z\frac{\mathrm{d}z}{\mathrm{d}\alpha} \tag{2.12}$$

where z and $\frac{\mathrm{d}z}{\mathrm{d}\alpha}$ are given by (2.7) and (2.9) respectively.

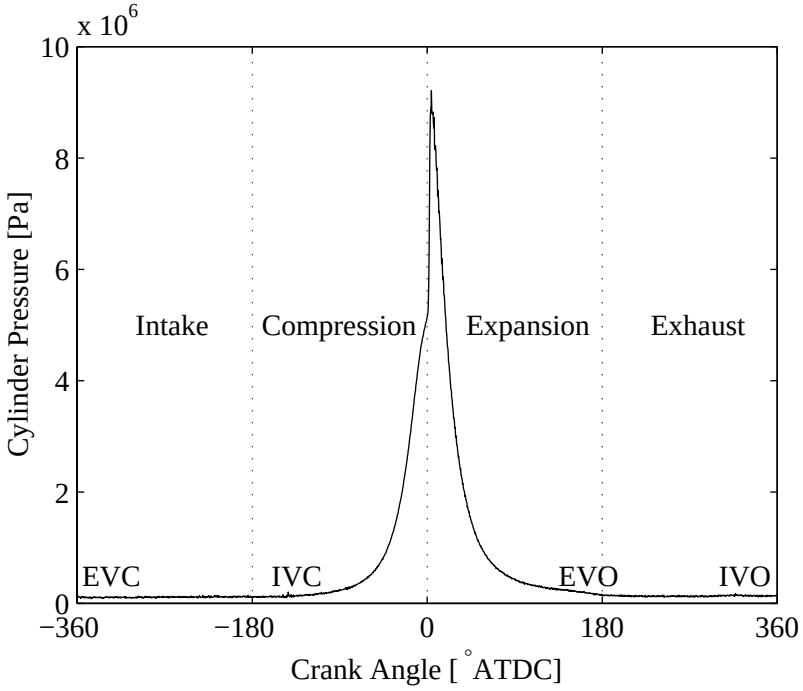

Figure 2.3: Major engine cycle events. EVC = Exhaust valve closing, IVC = Intake valve closing, EVO = Exhaust valve opening, and IVO = Intake valve opening.

2.4 The Thermodynamic Cycle of an Engine

The thermodynamic cycle of a four-stroke cycle engine spans two full revolutions of the crank shaft, and consists of four distinct strokes; intake, compression, expansion, and exhaust. The flow of gases is controlled by intake and exhaust valves, which are actuated by cams on the camshaft. The camshaft rotational speed is half of the engine speed, and thus allows for the two-revolution (720 crank-angle degrees) thermodynamic cycle. The sequence of events in a four-stroke engine is indicated by figure 2.3.

The mechanical work transferred from the cylinder gases to the piston during the course of one thermodynamic cycle is called the indicated work, and is given by

$$W_{c,i} = \int_{\alpha=-2\pi}^{2\pi} p(\alpha)\mathrm{d}V(\alpha) \tag{2.13}$$

An indicator diagram plots cylinder pressure versus combustion chamber volume (see figure 2.4), and clearly indicates the work as the area encircled clockwise by the trajectory. Any area which is encircled counterclockwise is counted as negative work.

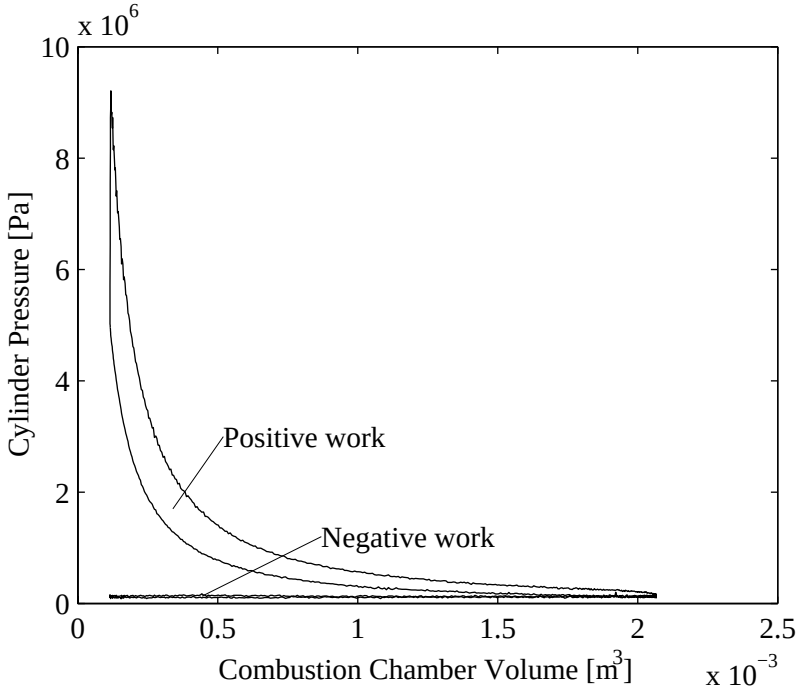

Figure 2.4: Indicator diagram. The area which is encircled clockwise represents the positive work produced by combustion. The very narrow area which is encircled counterclockwise represents the work required to pump gases through the cylinder.

2.5 Engine Combustion

Combustion in a reciprocating internal-combustion engine is initiated at some point towards the end of the compression stroke, and ends during the expansion stroke, when most of the fuel has been oxidized. It is the combustion, i.e. the conversion of reactants into products and chemical energy into thermal energy, which is responsible for most of the pressure difference between the expansion stroke and the compression stroke. This pressure difference results in the positive part of the indicated work defined in (2.13).

2.5.1 Combustion in Spark-Ignition Engines

Combustion in a spark-ignition engine is initiated by an electric discharge between the electrodes of a spark plug. The energy added by the spark plug is sufficient to dissociate some of the molecules in the spark-plug gap, and the local temperature and radical concentration is raised to such a level that a chain reaction starts. The chain reaction prop-

agates as a flame radially outward from the spark-plug gap until it reaches the combustion chamber walls, where it is extinguished.

The spark is fired late in the compression stroke, and the basic idea is to fire the spark at such a crank angle that the mechanical work is maximized. This spark timing is called MBT (Maximum Brake Torque) timing, and varies with operating conditions. In practice the spark is delayed somewhat from this optimum in order to avoid knock and excessive nitric oxide production.

2.5.2 Combustion in HCCI Engines

Combustion in a Homogeneous-Charge Compression-Ignition (HCCI) engine is initiated spontaneously by the high combustion-chamber temperature and pressure caused by compression (possibly assisted by heated inlet air). In an HCCI engine, like in a spark-ignition engine, the fuel and air is premixed in the intake before it is inducted into the cylinder. This results in spontaneous initiation of combustion simultaneously in many places throughout the combustion chamber. Thus, in an HCCI engine there is no propagating flame, but instead combustion is thought of as being homogeneously distributed throughout the combustion chamber.

Since combustion in an HCCI engine is spontaneous, there is no obvious way of controlling the combustion timing. There are however indirect ways of controlling it, e.g. by varying the inlet-air temperature, varying the compression ratio, or by recirculating exhaust gas. An additional method involves using two different fuels, which have different ignition characteristics. By varying the composition of the fuel mixture, the ignition timing can be controlled [38]. The control of ignition timing for HCCI engines is an open problem, and is currently an active area of research.

Chapter 3

Experimental Facilities

The experimental work for this dissertation has been performed on two different locations. The experiments for the air/fuel-ratio estimation (chapter 6) were performed in the Hesse Hall facility at the University of California, Berkeley, whereas the experiments for the pressure sensor offset estimation (chapter 5) were performed at the Lund Institute of Technology engine lab, Lund, Sweden.

3.1 The Berkeley Facility

The Berkeley facility features a Ford 3.0 liter V6 engine, which was donated by Ford Motor Company. The engine had previously been used in the Ford research labs in Dearborn, Michigan.

This setup was designed for investigating the control issues associated with cold starting of automotive engines.

3.1.1 Mechanical Setup

Power Dissipation and Motoring

A universal eddy current dynamometer is used for engine power dissipation and motoring. The dynamometer utilizes electromagnetic eddy currents to dissipate the mechanical power produced by the engine. For motoring, the dynamometer has a constant-speed AC motor, and an eddy-current clutch connecting the AC motor to the output shaft. This allows the engine to be motored at any speed lower than or equal to the AC-motor speed.

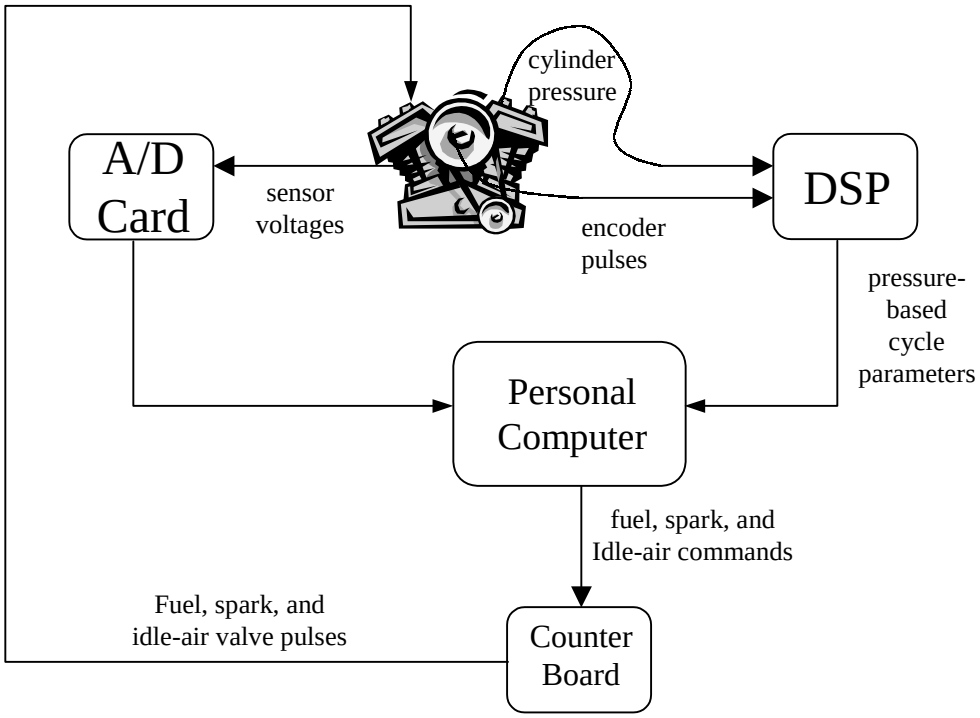

Figure 3.1: Schematics of the Berkeley measurement and control setup.

3.1.2 Data Acquisition

All data acquisition except for cylinder pressure acquisition is handled by a standard 16-bit data acquisition card connected to the ISA bus of a personal computer. Cylinder pressure acquisition, and pressure-based cycle analysis is handled by a dedicated Digital Signal Processor (DSP), also connected to the ISA bus. The reason for the distinction is the difference in bandwidth between the pressure signal and the other measured signals. The cylinder pressure signal has to be crank-angle resolved, whereas all other signals are treated as cycle-mean values. The measurement, and actuation setup is shown in figure 3.1.

Crank Position

The crank position is measured using an optical encoder mounted on the belt side of the crank shaft. The encoder provides two phase-shifted pulse channels, A and B, and one index channel, Z. Only the A and Z channels are used. The A and B channels each provide 360 pulses per revolution, and the Z channel provides one pulse per revolution for

crank-angle reference.

Cam Shaft Position

The cam shaft position is indicated once per revolution by an inductive pick-up. This information is combined with the Z-channel reference from the crank-shaft encoder in order to provide a 720° reference. This is necessary since a four-stroke thermodynamic cycle spans two revolutions (see section 2.4).

Cylinder Pressure

Cylinder pressure is measured using an optical pressure transducer. The sensing element is located in a hole drilled through the cylinder head into the combustion chamber. The sensing element consists of a metal diaphragm which deflects under pressure, and is connected by an optical fiber to a light source and a detector. The intensity of the reflected light is converted to a voltage which is proportional to the pressure.

Temperatures

The setup allows measurement of temperatures in the cooling system, engine oil, exhaust and catalytic converters, and in the intake manifold. The temperatures are measured using thermocouples connected to a multiplexing thermocouple amplifier. The multiplexed amplifier output is connected to a data acquisition board on the ISA bus.

Mass Airflow

The mass airflow into the intake manifold is measured using the standard hot-wire anemometer which comes with the engine. A hot-wire anemometer keeps the temperature of a thin wire constant by adjusting the current flowing through the wire. The current required to keep the temperature constant depends on the convective heat transfer, which depends on the mass airflow past the wire.

Exhaust

The engine is equipped with oxygen sensors upstream and downstream of the catalytic converters, and a linear oxygen sensor has been fitted in the exhaust upstream of

one of the catalytic converters. The information provided by the linear oxygen sensor is used for verification of the Air/Fuel ratio estimation in chapter 6.

A Flame Ionization Detecting (FID) Hydrocarbon analyzer is connected to one of the cylinder banks. It can be switched between measuring hydrocarbon concentration upstream or downstream of the catalytic converter.

3.1.3 Computation

All computational analysis of cylinder pressure is taken care of by a Digital Signal Processor (DSP) board. The DSP collects full 720° cycles of pressure data to perform cycle analysis on. The result is transferred to the control program on the host computer over the ISA bus.

3.1.4 Actuation

Fuel Injection

Fuel injection is done by solenoid-actuated fuel injectors. The solenoids are pulse-width controlled, and the pulses are generated by hardware counters located on a counter board connected to the ISA bus. Two counters are used for each fuel injector. The first counter counts crank-encoder pulses, to control the start of injection. The second counter is triggered by the first counter, and controls the time (in 10 μs units) that the injector is open. The TTL pulses generated by the counters are conditioned by fuel-injection drivers and fed to the injectors.

Spark Timing

The spark coils are actuated by spark modules which require a voltage pulse on the input. The pulse width controls the dwell time. The dwell time is the time the coil is energized before the spark fires.

The input pulses to the spark modules are generated using hardware counters, one counter per spark module. The counter first counts the proper number of crank-encoder pulses

Idle Air Control

The idle-air control valve is a pulse-width modulated valve which controls the amount of air entering the cylinders when the throttle is closed. The valve is designed mainly for controlling the engine speed while idling.

In this setup, the idle-air control valve is used as the only means of controlling the amount of air entering the engine, even at mid-range loads. This is possible since the valve has a large overcapacity at idle.

The pulse-width modulation of the valve is taken care of by a hardware counter.

3.2 The Lund Facility

The Lund facility features a Scania DSC-12, a 12 liter in-line 6-cylinder diesel engine, converted for Homogeneous Charge Compression Ignition (HCCI). The engine was donated by Scania in Södertälje, Sweden.

This setup is part of a project investigating the control issues with HCCI operation.

3.2.1 Mechanical Setup

Power Dissipation and Motoring

An AC dynamometer is used for engine power dissipation and motoring. The dynamometer can dissipate the engine power over the full speed-load range of the engine. It can also motor the engine over its full speed range.

A dynamometer controller keeps the engine at a constant user-selected speed.

The dynamometer is also used for starting the engine.

3.2.2 Instrumentation

Crank Position

The crank position is measured using an optical encoder mounted on the belt side of the crank shaft. The encoder provides two phase-shifted pulse channels, A and B, and one index channel, Z. Only the A and Z channels are used. The A and B channels each provide 1800 pulses per revolution, and the Z channel provides one pulse per revolution for crank-angle reference.

Cam Shaft Position

The cam shaft position is indicated once per revolution by an inductive proximity sensor. This information is combined with the Z-channel reference from the crank-shaft encoder in order to provide a 720° reference. This is necessary since a four-stroke thermodynamic cycle spans two revolutions (see section 2.4).

Cylinder Pressure

Cylinder pressure is measured using piezoelectric pressure transducers on all six cylinders. The sensing elements are located in a holes drilled through the cylinder head into the combustion chamber. The elements are cooled with a separate water cooling system in order to reduce the effect of thermal shock.

The outputs from the piezoelectric elements are fed to charge amplifiers, which convert the charge output of a piezoelectric crystal to a voltage. These voltages are fed to a stand-alone data acquisition board capable of simultaneous sample and hold on all channels, and 1 MSample/s sample rate per channel. The data acquisition board communicates with the personal computer using the parallel port.

Temperatures

Thermocouples are used to measure inlet air temperature before and after heater and cooler, and before and after the compressor. Exhaust temperature is measured before and after the exhaust turbine.

Exhaust

A full exhaust analyzing system is connected to the combined exhaust from all six cylinders. The analyzing system measures concentrations of hydrocarbons, carbon monoxide, carbon dioxide, oxygen, and oxides of nitrogen.

The exhaust concentration measurements are stored by a logger for post processing analysis.

3.2.3 Computation

All computation is performed by a personal computer. A computational thread performs cycle analysis on full 720° cycles of pressure data, and makes the data available to a control thread through a status object.

3.2.4 Actuation

Fuel Injection

The engine is equipped with two fuel injectors per cylinder. One injector injects a high-octane fuel, and the other a low-octane fuel. This is to allow control of the combustion timing. The pulses which control the injector solenoids are generated by a custom device, which communicates with a personal computer through a serial port. Injection commands specifying injector, injection time, and injection duration are sent to the device to control fuel injection. The device uses crank encoder pulses for injection timing, and an internal time base for injection duration.

Inlet Air Temperature Control

Inlet air heating provides an additional control of combustion timing. The inlet air is heated using electrical heaters downstream of the compressor.

The inlet air can be cooled down using a heat exchanger. This allows for better volumetric efficiency at high loads.

Chapter 4

Thermodynamic Analysis of Combustion in an Internal Combustion Engine using Cylinder Pressure

4.1 Background

4.1.1 Cylinder Pressure Measurement

The primary source of information about the combustion that takes place inside the cylinders of a reciprocating Internal Combustion (IC) engine, is the cylinder pressure. The cylinder pressure can be measured using piezoelectric or optical pressure transducers. The output from a piezoelectric transducer is in the form of a charge, and if a voltage output is desired, the transducer has to be connected to a charge amplifier.

One problem associated with all pressure transducers suited for cylinder pressure measurement is that they show an offset, which varies with time. This offset has to be estimated for each cycle, and a method for doing this is presented in chapter 5.

4.1.2 Thermodynamics

This chapter uses fundamental thermodynamics and combustion chemistry to derive a differential equation, which relates the progress of the combustion process to the measured cylinder pressure. The model derived here is a one-zone model, i.e. it assumes homogeneous conditions throughout the combustion chamber. This is a good approximation for e.g. a Homogeneous Charge Compression Ignition (HCCI) Engine [45], where spontaneous ignition occurs in many locations throughout the combustion chamber. In a Spark-Ignition (SI) engine however, where a flame propagates radially outward from the spark plug(see chapter 6), the combustion chamber can, at any time, be divided into one region which contains contains unburned gas, and one region which contains burned gas. The one-zone approach is still valuable as an approximation, though, due to its simplicity compared to a two-zone model.

In a two-zone model, the heat transfer between the two zones has to be modeled, and this requires a model for the surface area of the interface between the two zones. It also requires a model for the heat-transfer coefficient for the interface between the two zones. Both of these models are very difficult to obtain due to the turbulent nature of combustion in an SI engine.

Finally, the differential equation derived from the one-zone assumption, is simplified further to make it suitable for real-time control applications. Some combustion parameters, which are based on the solution to the simplified equation are defined, and the sensitivity of these parameters to various sources of error is evaluated.

4.2 System Definition

The system of interest, when analyzing the thermodynamics of combustion in an IC engine, is the gas trapped in the combustion chamber during compression, combustion, and expansion, see figure (4.1). This gas is a mixture of fuel, air, residual gases, and possibly EGR. During combustion, reactants (fuel and air) will be converted to products ($\mathbf{CO_2}$, $\mathbf{H_2O}$, $\mathbf{CO}$, etc.,) and chemical energy will be converted into thermal energy.

The first law of thermodynamics for this system states

$$\mathrm{d}U = \delta Q - \delta W \tag{4.1}$$

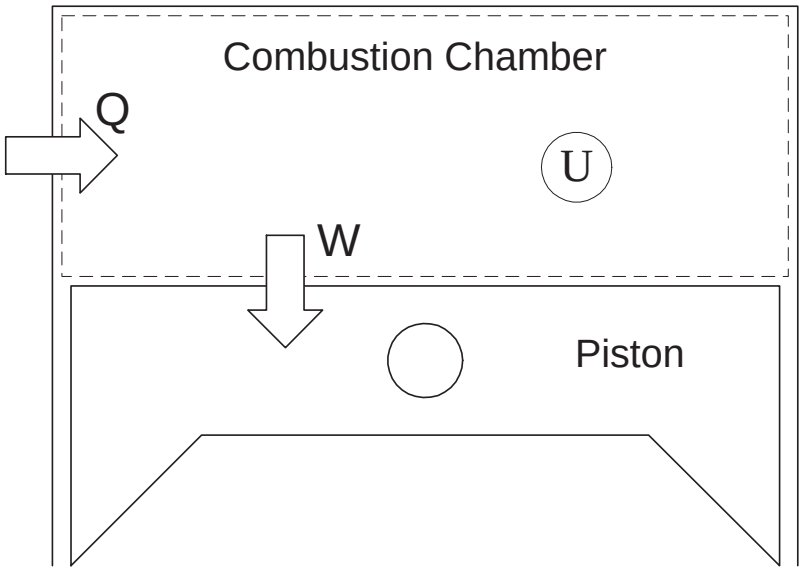

Figure 4.1: System used for thermodynamic analysis of combustion. U represents the internal energy of the gas contained in the cylinder, W represents mechanical work performed on the piston by the gas, and Q represents heat transfered from the cylinder wall to the gas.

where dU is the change in internal energy, δQ is heat added to the system, and δW is the mechanical work done by the system.

4.3 Thermodynamic Analysis

4.3.1 Thermodynamic Model

Combustion in a reciprocating internal combustion engine is often analyzed using a heat release approach [19]. In this approach, the conversion of chemical energy into thermal energy is modeled as heat. In essence,

$$n\tilde{c}_v \mathrm{d}T = \delta Q - p\mathrm{d}V$$

with

$$\delta Q = \delta Q_{ht} + \delta Q_{ch}$$

δQ_{ht} represents heat transfer and δQ_{ch} represents conversion of chemical energy to thermal energy. The composition of the gas is assumed to be constant throughout the combustion

process.

The model presented here takes into account the change in composition of the cylinder contents as combustion is taking place. The model uses the first law of thermodynamics (4.1), the ideal gas law

$$pV = n\tilde{R}T \tag{4.2}$$

and the stoichiometry of the overall chemical reaction, which describes the combustion process

$$\mathbf{C_xH_y} + \left(x + \frac{y}{4}\right)\mathbf{O_2} \rightarrow x\mathbf{CO_2} + \frac{y}{2}\mathbf{H_2O} \tag{4.3}$$

where the fuel is assumed to be a hydrocarbon with a H/C-ratio of y/x.

4.3.2 Analysis

The total number of moles in the combustion chamber can, at any time be described by

$$n = \sum_i n_i \tag{4.4}$$

where i can take any of the values $\mathbf{C_xH_y}$, $\mathbf{O_2}$, $\mathbf{H_2O}$, $\mathbf{CO_2}$, or $\mathbf{N_2}$[1]. The internal energy of the gas in the combustion chamber can then be expressed using the molar specific internal energies according to

$$U = U\left(n_{\mathbf{C_xH_y}}, n_{\mathbf{O_2}}, n_{\mathbf{CO_2}}, n_{\mathbf{H_2O}}, n_{\mathbf{N_2}}, T\right) = \sum_i n_i \tilde{u}_i(T) \tag{4.5}$$

Now, the left-hand side of equation (4.1) can be expressed as

$$\mathrm{d}U = \sum_i \tilde{u}_i \mathrm{d}n_i + n\tilde{c}_v \mathrm{d}T \tag{4.6}$$

where $\tilde{c}_v$ is the molar specific heat at constant volume of the gas mixture.

The stoichiometric relationship defined in (4.3) provides a means of relating the

[1] Other species are present, e.g. $\mathbf{CO}$, $\mathbf{H_2}$, $\mathbf{NO}$, $\mathbf{OH}$, $\mathbf{O}$, and $\mathbf{H}$, but if a lean or stoichiometric mixture is assumed, the mole fractions of these species are negligible from an internal-energy point of view [19].

mole differentials at any intermediate state during the combustion process.

$$\mathrm{d}n_{\mathbf{O_2}} = \left(x + \frac{y}{4}\right) \mathrm{d}n_{\mathbf{C_xH_y}} \tag{4.7a}$$

$$\mathrm{d}n_{\mathbf{CO_2}} = -x\mathrm{d}n_{\mathbf{C_xH_y}} \tag{4.7b}$$

$$\mathrm{d}n_{\mathbf{H_2O}} = -\frac{y}{2}\mathrm{d}n_{\mathbf{C_xH_y}} \tag{4.7c}$$

$$\mathrm{d}n_{\mathbf{N_2}} = 0 \tag{4.7d}$$

Differentiation of (4.4) yields

$$\begin{aligned} \mathrm{d}n = \mathrm{d}n_{\mathbf{C_xH_y}} + \mathrm{d}n_{\mathbf{O_2}} + \mathrm{d}n_{\mathbf{CO_2}} + \mathrm{d}n_{\mathbf{H_2O}} + \mathrm{d}n_{\mathbf{N_2}} = \\ \left[1 + \left(x + \frac{y}{4}\right) - x - \frac{y}{2}\right] \mathrm{d}n_{\mathbf{C_xH_y}} = \left(1 - \frac{y}{4}\right) \mathrm{d}n_{\mathbf{C_xH_y}} \end{aligned} \tag{4.8}$$

Combining (4.7) and (4.8), an equation relating each mole differential, $\mathrm{d}n_i$, to the total mole differential, $\mathrm{d}n$ is obtained.

$$\mathrm{d}n_{\mathbf{C_xH_y}} = -\frac{4}{y-4}\mathrm{d}n \tag{4.9a}$$

$$\mathrm{d}n_{\mathbf{O_2}} = -\frac{4x+y}{y-4}\mathrm{d}n \tag{4.9b}$$

$$\mathrm{d}n_{\mathbf{CO_2}} = \frac{4x}{y-4}\mathrm{d}n \tag{4.9c}$$

$$\mathrm{d}n_{\mathbf{H_2O}} = \frac{2y}{y-4}\mathrm{d}n \tag{4.9d}$$

$$\mathrm{d}n_{\mathbf{N_2}} = 0 \tag{4.9e}$$

Differentiating (4.2), yields

$$\mathrm{d}T = \frac{T}{p}\mathrm{d}p + \frac{T}{V}\mathrm{d}V - \frac{T}{n}\mathrm{d}n \tag{4.10}$$

and the last term of (4.6) can be rewritten as

$$n\tilde{c}_v\mathrm{d}T = \frac{\tilde{c}_v nT}{p}\mathrm{d}p + \frac{\tilde{c}_v nT}{V}\mathrm{d}V - \tilde{c}_v T\mathrm{d}n \tag{4.11}$$

Combining (4.6), (4.9), and (4.11) finally yields

$$\begin{aligned} \mathrm{d}U = &\left(-\frac{4}{y-4}\tilde{u}_{\mathbf{C_xH_y}} - \frac{4x+y}{y-4}\tilde{u}_{\mathbf{O_2}} + \frac{4x}{y-4}\tilde{u}_{\mathbf{CO_2}} + \frac{2y}{y-4}\tilde{u}_{\mathbf{H_2O}} - \tilde{c}_v T\right)\mathrm{d}n \\ &+ \frac{\tilde{c}_v nT}{p}\mathrm{d}p + \frac{\tilde{c}_v nT}{V}\mathrm{d}V \end{aligned} \tag{4.12}$$

for the internal energy.

Next, it is assumed that all work is $p\mathrm{d}V$ work, which yields a first law of the form

$$\mathrm{d}U = \delta Q - p\mathrm{d}V \tag{4.13}$$

Putting (4.12) and (4.13) together yields a differential equation describing the combustion process

$$\left(-\frac{4}{y-4}\tilde{u}_{\mathbf{C_xH_y}} - \frac{4x+y}{y-4}\tilde{u}_{\mathbf{O_2}} + \frac{4x}{y-4}\tilde{u}_{\mathbf{CO_2}} + \frac{2y}{y-4}\tilde{u}_{\mathbf{H_2O}} - \tilde{c}_v T\right)\mathrm{d}n + \frac{\tilde{c}_v n T}{p}\mathrm{d}p + \frac{\tilde{c}_v n T}{V}\mathrm{d}V = \delta Q - p\mathrm{d}V \tag{4.14}$$

Application of the ideal gas law, (4.2), and the identity $\tilde{c}_p - \tilde{c}_v = \tilde{R}$, simplifies (4.14) into

$$\left(-\frac{4}{y-4}\tilde{u}_{\mathbf{C_xH_y}} - \frac{4x+y}{y-4}\tilde{u}_{\mathbf{O_2}} + \frac{4x}{y-4}\tilde{u}_{\mathbf{CO_2}} + \frac{2y}{y-4}\tilde{u}_{\mathbf{H_2O}} - \tilde{c}_v T\right)\mathrm{d}n + \frac{\tilde{c}_v}{\tilde{R}}V\mathrm{d}p + \frac{\tilde{c}_p}{\tilde{R}}p\mathrm{d}V - \delta Q = 0 \tag{4.15}$$

4.4 Comparison with Standard Heat Release Analysis

If standard heat release analysis is performed on the system described in section 4.2, the equation one arrives at is

$$\tilde{Q}_{LHV}\mathrm{d}n_{\mathbf{C_xH_y}} + \frac{\tilde{c}_v}{\tilde{R}}V\mathrm{d}p + \frac{\tilde{c}_p}{\tilde{R}}p\mathrm{d}V - \delta Q = 0 \tag{4.16}$$

Here, $\tilde{Q}_{LHV}$ is the lower heating value of the fuel, which is a constant representing how much chemical energy is converted into thermal energy, per mole of fuel.

Equation (4.15) can be rewritten as

$$\tilde{Q}_{hr}\mathrm{d}n_{\mathbf{C_xH_y}} + \frac{\tilde{c}_v}{\tilde{R}}V\mathrm{d}p + \frac{\tilde{c}_p}{\tilde{R}}p\mathrm{d}V - \delta Q = 0 \tag{4.17}$$

with $\tilde{Q}_{hr}$ defined as

$$\tilde{Q}_{hr} = \left(-\frac{4}{y-4}\tilde{u}_{\mathbf{C_xH_y}} - \frac{4x+y}{y-4}\tilde{u}_{\mathbf{O_2}} + \frac{4x}{y-4}\tilde{u}_{\mathbf{CO_2}} + \frac{2y}{y-4}\tilde{u}_{\mathbf{H_2O}} - \tilde{c}_v T\right)\frac{\mathrm{d}n}{\mathrm{d}n_{\mathbf{C_xH_y}}} = \tilde{u}_{\mathbf{C_xH_y}} + \frac{4x+y}{4}\tilde{u}_{\mathbf{O_2}} - x\tilde{u}_{\mathbf{CO_2}} - \frac{y}{2}\tilde{u}_{\mathbf{H_2O}} + \frac{y-4}{4}\tilde{c}_v T \tag{4.18}$$

It is observed that (4.17) has the same form as (4.16), with $\tilde{Q}_{LHV}$ replaced by $\tilde{Q}_{hr}$.

Figure 4.2 shows $\tilde{Q}_{hr}/\tilde{Q}_{LHV}$ as a function of temperature. The figure shows that the relative difference between the two methods increases with temperature, and at 3000K the difference is 8%. The observed difference between $\tilde{Q}_{LHV}$ and $\tilde{Q}_{hr}$ is quite significant, when e.g. computing the combustion efficiency of an engine.

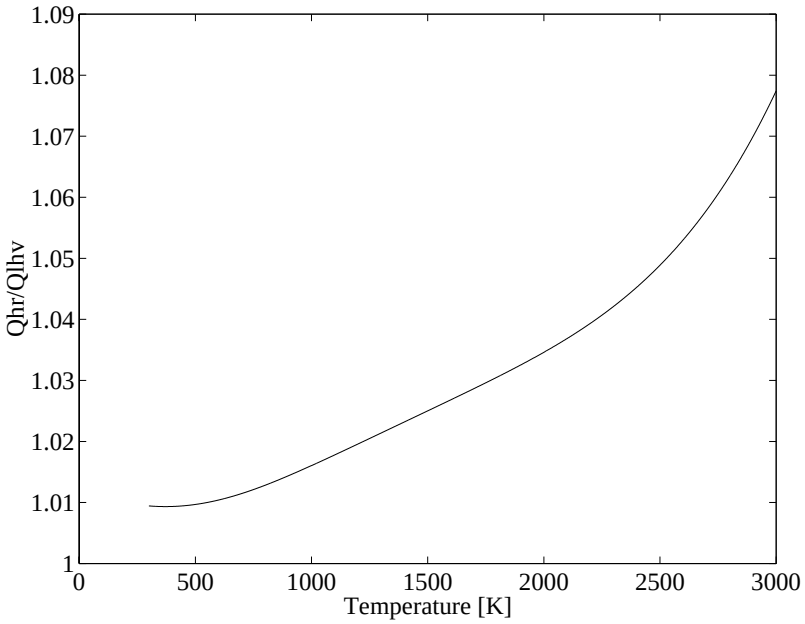

Figure 4.2: $\tilde{Q}_{hr}/\tilde{Q}_{LHV}$ as a function of temperature.

4.4.1 Crevice Effects

Crevice effects are the effects of combustion chamber gases escaping into crevice volumes, e.g. the small volume between the piston and the cylinder wall above the piston rings. Gas is pushed into crevice volumes during compression and combustion, and comes back out again when the pressure drops during expansion. This affects the analysis above, because the gas temperatures are different in the crevice volumes and in the bulk volume. The temperature in the crevice volumes stays close to the temperature of the coolant, due to the fact that these volumes are small and thin.

In order to keep the notation above simple, crevice effects are not taken into account. They can however be included in the same way as for standard heat release analysis [15].

4.4.2 Heat Transfer

The term δQ in (4.15) represents heat transfer across the system boundary. Heat transfer between the cylinder gases and the cylinder walls takes place during the whole

engine cycle. During intake and early compression, heat is transferred from the cylinder walls to the gases, and during combustion and expansion, heat is transferred from the gases to the cylinder walls.

The rate of heat transfer through convection, can be calculated from

$$\frac{\mathrm{d}Q_{ht}}{\mathrm{d}t} = Ah_c(T_w - T) \tag{4.19}$$

where A is the combustion chamber surface area, h_c the heat-transfer coefficient, T_w the cylinder wall temperature, and T the gas temperature. The heat-transfer coefficient can be estimated using Woschni's correlation [52]

$$h_c[\mathrm{W/(m^2 \cdot K)}] = 3.26B[\mathrm{m}]^{-0.2}p[\mathrm{kPa}]^{0.8}T[\mathrm{K}]^{-0.55}w[\mathrm{m/s}]^{0.8} \tag{4.20}$$

where B is the bore of the cylinder, p is the cylinder pressure, T is the gas temperature, and w is the average cylinder gas velocity. The average cylinder gas velocity is essentially proportional to the mean piston speed.

4.5 Applications

The detailed knowledge of crank-angle-resolved mixture composition and gas temperature which are obtained by integrating (4.15) are of interest when e.g. trying to estimate the cycle-resolved combustion efficiency of an engine. The combustion efficiency estimate obtained from exhaust gas analysis is severely low-pass filtered and delayed, due to response times of instruments, and transport delays between engine cylinders and instruments.

The same detailed information is also of interest when trying to predict pollutant emissions based on cylinder-pressure measurements. The water gas reaction e.g. controls the equilibrium concentration of **CO**

$$\mathbf{CO_2 + H_2O \rightleftharpoons CO + H_2}$$

This reaction can be incorporated into the model to cover fuel-rich conditions as well. Its equilibrium constant is tabulated in JANAF [46].

Similarly, the **NO** concentration is controlled by a few equilibrium reactions, and could be predicted using the crank-angle-resolved composition and temperature information.

4.5.1 Simplifications for Real-Time Control Applications

In case the differential equation (4.15) is too time consuming to integrate for each cycle, or if the detailed knowledge about composition and temperature is not required, some different degrees of simplifications can be made.

Constant Gas Composition

If the gas composition inside the combustion chamber is assumed constant, one arrives at the standard heat release equation as observed in section 4.4. This is often sufficient, especially when detailed information about gas composition and combustion chamber temperature is not required.

No Heat Losses or Crevice Effects (Net Heat Release)

If heat loss to combustion chamber walls, and crevice effects are neglected, the heat release equation simplifies to

$$\delta Q_{ch} = \frac{\tilde{c}_v}{\tilde{R}} V \mathrm{d}p + \frac{\tilde{c}_p}{\tilde{R}} p \mathrm{d}V \tag{4.21}$$

Q_{ch} in (4.21) is called the net heat release.

Constant Specific Heat

$$\delta Q_{ch} = \frac{\tilde{c}_v}{\tilde{R}} V \mathrm{d}p + \frac{\tilde{c}_p}{\tilde{R}} p \mathrm{d}V \tag{4.22}$$

$\tilde{c}_v$ and $\tilde{c}_p$ in (4.22) are functions of temperature, but vary slowly with temperature (see figure 4.3).

$$\delta Q_{ch} = \frac{\tilde{c}_v}{\tilde{R}} (V \mathrm{d}p + p \mathrm{d}V) + \left(\frac{\tilde{c}_p}{\tilde{R}} - \frac{\tilde{c}_v}{\tilde{R}} \right) p \mathrm{d}V = \frac{\tilde{c}_v}{\tilde{R}} (V \mathrm{d}p + p \mathrm{d}V) + p \mathrm{d}V \tag{4.23}$$

$$\mathrm{d}(pV) = p \mathrm{d}V + V \mathrm{d}p \tag{4.24}$$

Equations (4.24) and (4.23) are combined to yield

$$\delta Q_{ch} = \frac{\tilde{c}_v}{\tilde{R}} \mathrm{d}(pV) + p \mathrm{d}V \tag{4.25}$$

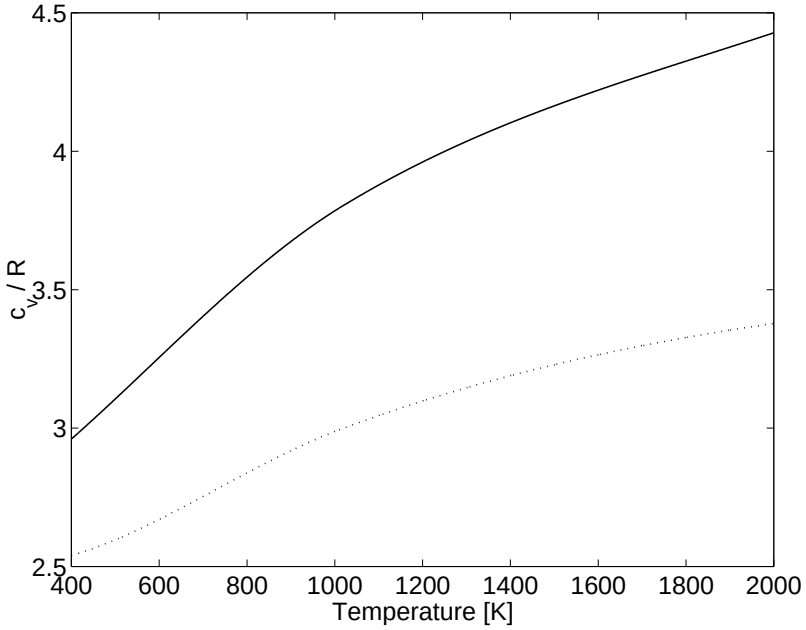

Figure 4.3: Specific heat plotted against temperature for a stoichiometric mixture of isooctane and air (solid line), and for pure air (dotted line).

Now, assuming that crank-angle resolved measurements of p are available, (4.25) can be rewritten on a form where the crank-angle dependence is explicit.

$$\frac{\mathrm{d}Q_{ch}}{\mathrm{d}\alpha} = \frac{\tilde{c}_v}{\tilde{R}} \frac{\mathrm{d}(pV)}{\mathrm{d}\alpha} + p(\alpha) \frac{\mathrm{d}V}{\mathrm{d}\alpha} \tag{4.26}$$

This can be integrated to yield the cumulative net heat release.

$$Q_{ch}(\alpha) = \int_{\alpha_0}^{\alpha} \left(\frac{\tilde{c}_v}{\tilde{R}} \frac{\mathrm{d}(pV)}{\mathrm{d}\alpha} + p(\alpha) \frac{\mathrm{d}V}{\mathrm{d}\alpha} \right) \mathrm{d}\alpha = \int_{\alpha_0}^{\alpha} \frac{\tilde{c}_v}{\tilde{R}} \frac{\mathrm{d}(pV)}{\mathrm{d}\alpha} \mathrm{d}\alpha + \int_{\alpha_0}^{\alpha} p(\alpha) \frac{\mathrm{d}V}{\mathrm{d}\alpha} \mathrm{d}\alpha \tag{4.27}$$

Now, if $\tilde{c}_v$ is assumed to be constant, the factor $\frac{\tilde{c}_v}{\tilde{R}}$ in the integrand can be moved outside the integral

$$\begin{aligned} Q_{ch}(\alpha) &= \frac{\tilde{c}_v}{\tilde{R}} \int_{\alpha_0}^{\alpha} \frac{\mathrm{d}(pV)}{\mathrm{d}\alpha} \mathrm{d}\alpha + \int_{\alpha_0}^{\alpha} p(\alpha) \frac{\mathrm{d}V}{\mathrm{d}\alpha} \mathrm{d}\alpha \\ &= \frac{\tilde{c}_v}{\tilde{R}} [p(\alpha)V(\alpha) - p(\alpha_0)V(\alpha_0)] + \int_{\alpha_0}^{\alpha} p(\alpha) \frac{\mathrm{d}V}{\mathrm{d}\alpha} \mathrm{d}\alpha \end{aligned} \tag{4.28}$$

This formulation of the heat release equation is attractive in that it avoids numerical differentiation of the measured pressure data. Numerical differentiation is particularly bad at high sample rates, which makes the signal-to-noise ratio very low. Here, the integral

containing the pressure derivative in the integrand is instead evaluated analytically. Thus, only the pressure values at the endpoints of the integral are evaluated.

4.5.2 Evaluation of the Constant Specific Heat Equation

This section will evaluate the heat release equation (4.28), which assumes constant specific heat. It will be evaluated in terms of its sensitivity with respect to the selection of specific heat, and its sensitivity with respect to offset errors in the measured pressure.

Definitions of some Heat-Release Based Cycle Parameters

Figure 4.4 shows the typical features of a heat-release profile computed using equation (4.28). It shows a decreasing trend during the part of the cycle preceding combustion. This trend is due to the heat transfer to the walls, which are not included in the model for net heat release. It shows a rapid increase due to combustion. This increase represents the conversion of chemical energy to thermal energy by combustion. Finally, it shows a somewhat steeper decreasing trend after combustion than before. This represents the accelerated heat losses due to higher temperature and turbulence intensity compared to before the combustion event.

Figure 4.28 also defines some heat-release based cycle parameters which will be used in the evaluation of the heat-release equation.

Q_{min} and Q_{max} represent the minimum and maximum of $Q_{ch}(\alpha)$ respectively.

$$Q_{min} = \min_{\alpha}[Q_{ch}(\alpha)] \tag{4.29}$$

$$Q_{max} = \max_{\alpha}[Q_{ch}(\alpha)] \tag{4.30}$$

The total heat release, Q_{tot}, represents the increase in $Q_{ch}(\alpha)$ due to combustion, and is approximately equal to the amount of chemical energy which is converted to thermal energy during combustion.

$$Q_{tot} = Q_{max} - Q_{min} \tag{4.31}$$

The crank angle of 10% burnt (or 10% heat release), $\alpha_{10\%}$, approximately represents the crank angle when combustion starts. The reason for choosing 10% instead of 0%

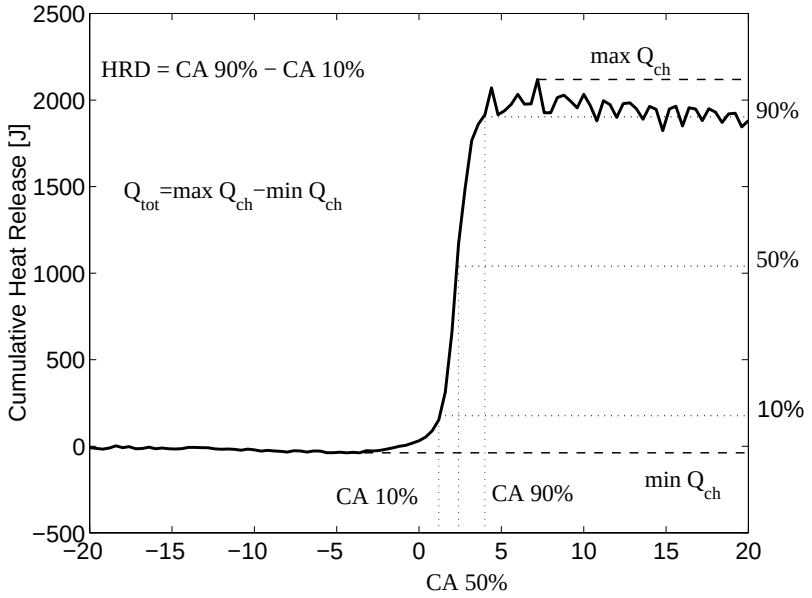

Figure 4.4: Definitions of some heat-release based cycle parameters.

is that it provides a more well-defined crank-angle measure. $\alpha_{10\%}$ is defined by

$$Q_{ch}(\alpha_{10\%}) = Q_{min} + 0.1 \cdot Q_{tot} \tag{4.32}$$

Similarly, the crank angle of 50% heat release, $\alpha_{50\%}$, is defined to indicate at what crank angle the bulk of the combustion takes place. $\alpha_{50\%}$ is defined by

$$Q_{ch}(\alpha_{50\%}) = Q_{min} + 0.5 \cdot Q_{tot} \tag{4.33}$$

The crank angle of 90% heat release, $\alpha_{90\%}$, indicates the end of combustion in the same way that α_{10} indicates the start of combustion. $\alpha_{90\%}$ is defined by

$$Q_{ch}(\alpha_{90\%}) = Q_{min} + 0.9 \cdot Q_{tot} \tag{4.34}$$

Finally, the heat release duration, $\Delta\alpha_b$, represents the duration of the combustion event in crank angle degrees.

$$\Delta\alpha_b = \alpha_{90\%} - \alpha_{10\%} \tag{4.35}$$

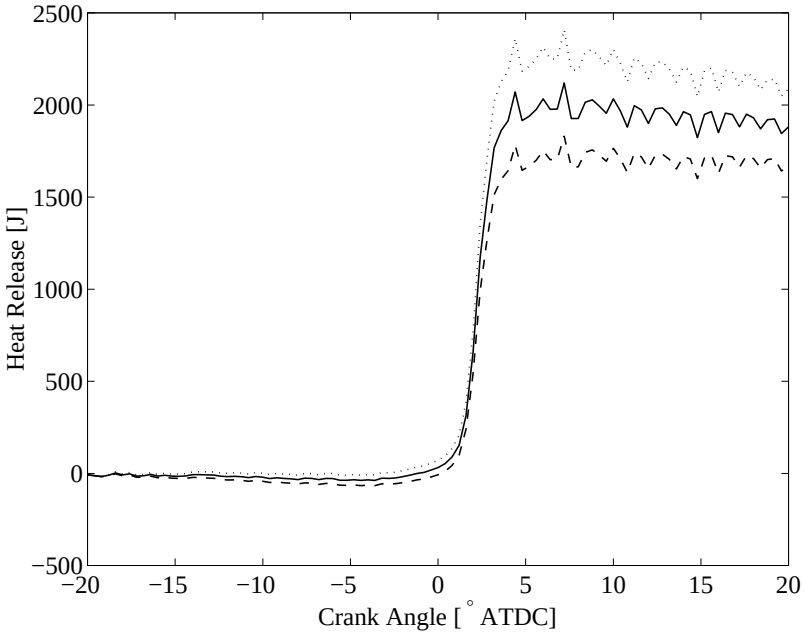

Figure 4.5: Heat release profile for one cycle using $\frac{\tilde{c}_v}{\tilde{R}} = 3.5$ (dashed line), and $\frac{\tilde{c}_v}{\tilde{R}} = 4.0$ (solid line), and $\frac{\tilde{c}_v}{\tilde{R}} = 4.5$ (dotted line).

Sensitivity with respect to Specific Heat

Figures 4.5 – 4.11 indicate how sensitive this form of the heat release equation is to changes in the specific heat, $\frac{\tilde{c}_v}{\tilde{R}}$, used in the computations. Figure 4.5 shows that the absolute level of the heat release is quite sensitive. In fact, an expression for the sensitivity of the cumulative heat release, at crank angle α, can be derived.

$$\frac{\mathrm{d}Q_{ch}}{\mathrm{d}(\tilde{c}_v/\tilde{R})} = p(\alpha)V(\alpha) - p(\alpha_0)V(\alpha_0) \tag{4.36}$$

In figure 4.7 the sensitivity is plotted versus crank angle for the same cycle used in figure 4.5, and the difference between the two heat release profiles is completely explained by the sensitivity function.

For reference, figure 4.6 shows heat release profiles for a motored (no combustion) cycle using different values for specific heat. Since the heat release model assumes no heat losses to the cylinder walls, the losses that actually do occur show up as a steady decrease in the cumulative heat release. The same decrease can be seen in the cycle with combustion (figure 4.5), although it is small compared to the increase caused by combustion.

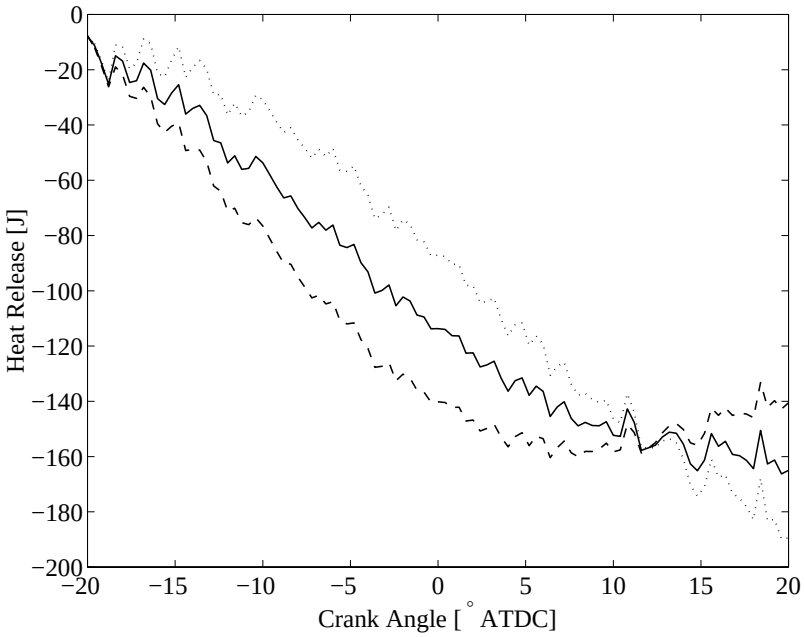

Figure 4.6: Heat release profile for a motored cycle using $\frac{\tilde{c}_v}{\tilde{R}} = 2.5$ (dashed line), and $\frac{\tilde{c}_v}{\tilde{R}} = 3.0$ (solid line), and $\frac{\tilde{c}_v}{\tilde{R}} = 3.5$ (dotted line).

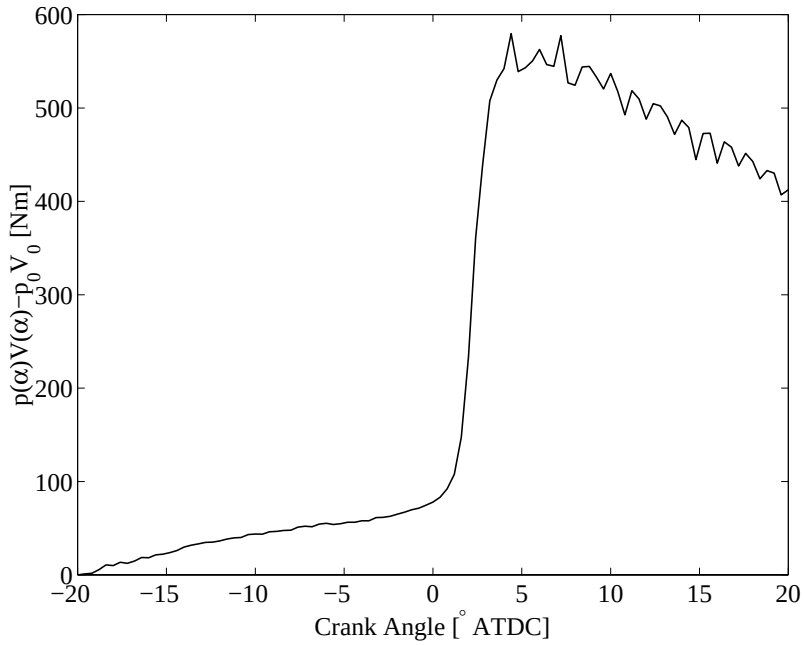

Figure 4.7: Sensitivity function for the heat release with respect to specific heat, $\frac{\tilde{c}_v}{\tilde{R}}$. Same cycle as in figure 4.5.

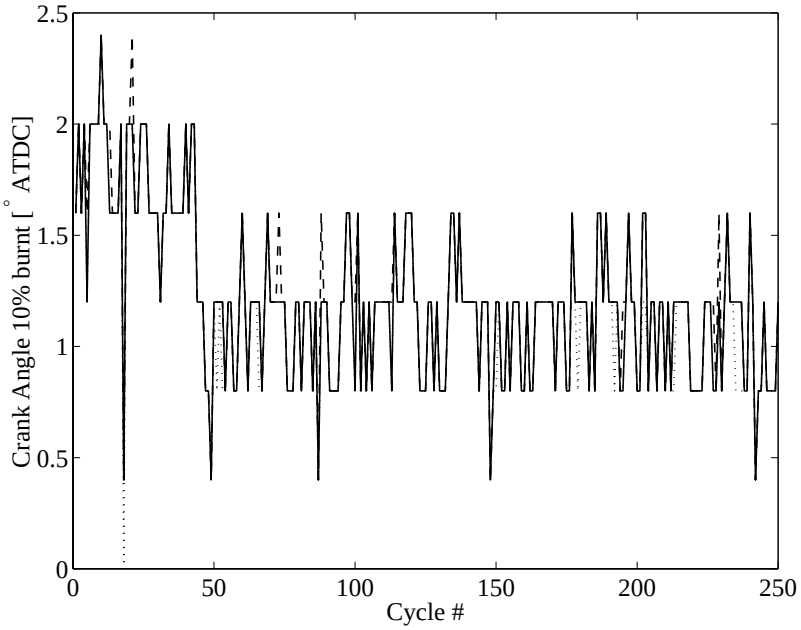

Figure 4.8: Crank angle of 10% burnt for 250 consecutive cycles using $\frac{\tilde{c}_v}{R} = 3.5$ (dashed line), and $\frac{\tilde{c}_v}{R} = 4.0$ (solid line), and $\frac{\tilde{c}_v}{R} = 4.5$ (dotted line).

Figures 4.8 – 4.11 show that the burn profile in the crank angle domain is quite insensitive.

Sensitivity with respect to Pressure Offset

As will be discussed in chapter 5, cylinder pressure measurements are always relative in the sense that the DC offset varies from cycle to cycle. Chapter 5 will also present ways of removing this offset. These methods are not exact however, and this means that the pressure measurements which are used in the heat release equation (4.28) have a small but unknown offset. This section will evaluate the sensitivity of the computed heat release with respect to this offset.

Assume that the cylinder pressure measurements can be expressed as

$$p_m(\alpha) = p(\alpha) + \Delta p \tag{4.37}$$

where $p_m(\alpha)$ is the measured cylinder pressure, $p(\alpha)$ is the real cylinder pressure, and Δp

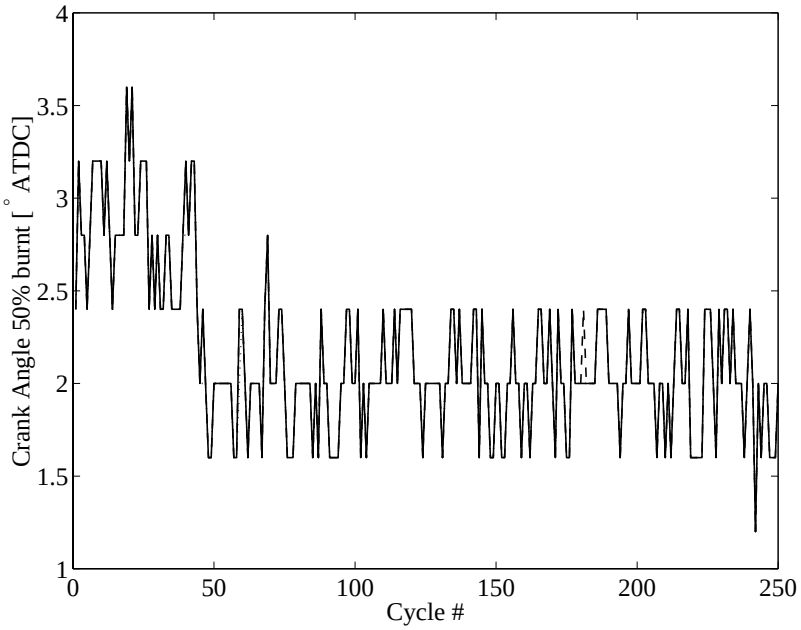

Figure 4.9: Crank angle of 50% burnt for 250 consecutive cycles using $\frac{\tilde{c}_v}{R} = 3.5$ (dashed line), and $\frac{\tilde{c}_v}{R} = 4.0$ (solid line), and $\frac{\tilde{c}_v}{R} = 4.5$ (dotted line).

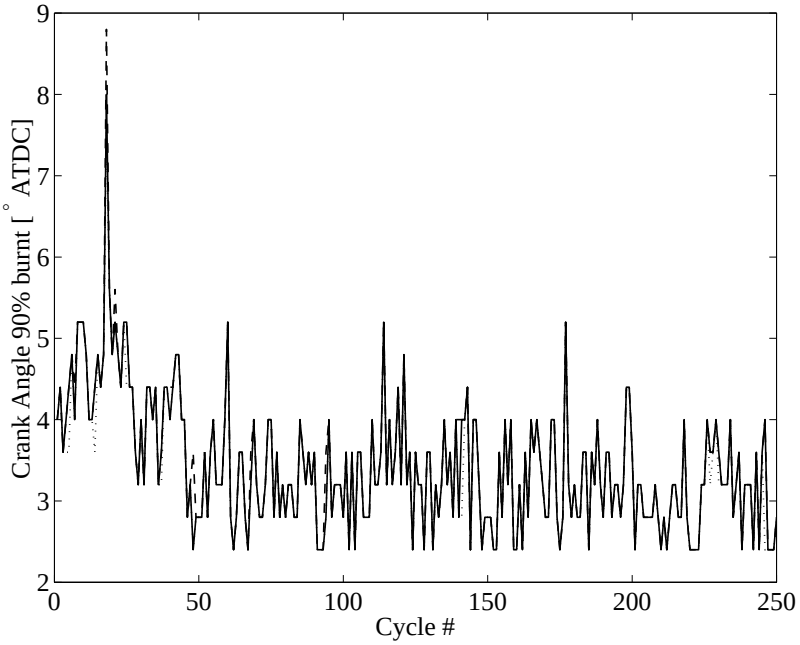

Figure 4.10: Crank angle of 90% burnt for 250 consecutive cycles using $\frac{\tilde{c}_v}{R} = 3.5$ (dashed line), and $\frac{\tilde{c}_v}{R} = 4.0$ (solid line), and $\frac{\tilde{c}_v}{R} = 4.5$ (dotted line).

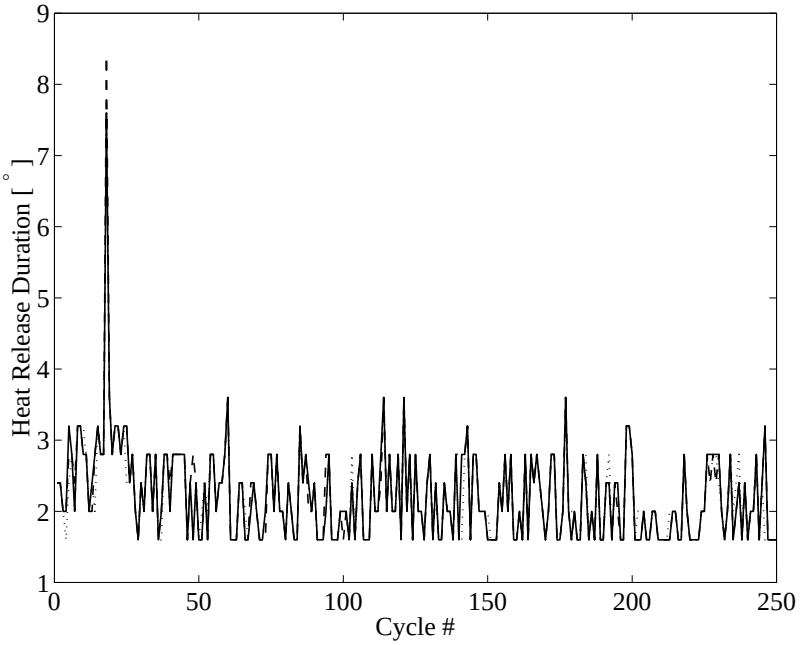

Figure 4.11: Heat release duration in crank angle degrees for 250 consecutive cycles using $\frac{\tilde{c}_v}{\tilde{R}} = 3.5$ (dashed line), and $\frac{\tilde{c}_v}{\tilde{R}} = 4.0$ (solid line), and $\frac{\tilde{c}_v}{\tilde{R}} = 4.5$ (dotted line).

is a constant measurement error. Then (4.28) can be rewritten according to

$$Q_{ch}(\alpha) = \frac{\tilde{c}_v}{\tilde{R}}[(p_m(\alpha) + \Delta p)V(\alpha) - (p_{m0} + \Delta p)V_0] + \int_{\alpha_0}^{\alpha}(p_m(\alpha) + \Delta p)\frac{\mathrm{d}V}{\mathrm{d}\alpha}\mathrm{d}\alpha \tag{4.38}$$

Separating out the dependence on Δp yields

$$\begin{aligned} Q_{ch}(\alpha) &= \frac{\tilde{c}_v}{\tilde{R}}(p_m(\alpha)V(\alpha) - p_{m0}V_0) + \int_{\alpha_0}^{\alpha} p_m(\alpha)\frac{\mathrm{d}V}{\mathrm{d}\alpha}\mathrm{d}\alpha \\ &\quad + \left[\frac{\tilde{c}_v}{\tilde{R}}(V(\alpha) - V_0) + \int_{\alpha_0}^{\alpha}\frac{\mathrm{d}V}{\mathrm{d}\alpha}\mathrm{d}\alpha\right]\Delta p \\ &= Q_{chm} + \left[\frac{\tilde{c}_v}{\tilde{R}}(V(\alpha) - V_0) + V(\alpha) - V_0\right]\Delta p \\ &= Q_{chm} + \left(\frac{\tilde{c}_v}{\tilde{R}} + 1\right)(V(\alpha) - V_0)\Delta p \end{aligned} \tag{4.39}$$

Thus, the sensitivity of Q_{ch} with respect to Δp is given by

$$\frac{\mathrm{d}Q_{ch}}{\mathrm{d}(\Delta p)} = \left(\frac{\tilde{c}_v}{\tilde{R}} + 1\right)(V(\alpha) - V_0) \tag{4.40}$$

Figure 4.12 shows a plot of the pressure offset sensitivity function for a few different choices of specific heat. The maximum sensitivity is approximately $4 \cdot 10^{-4}$ m^3 at 0°. In

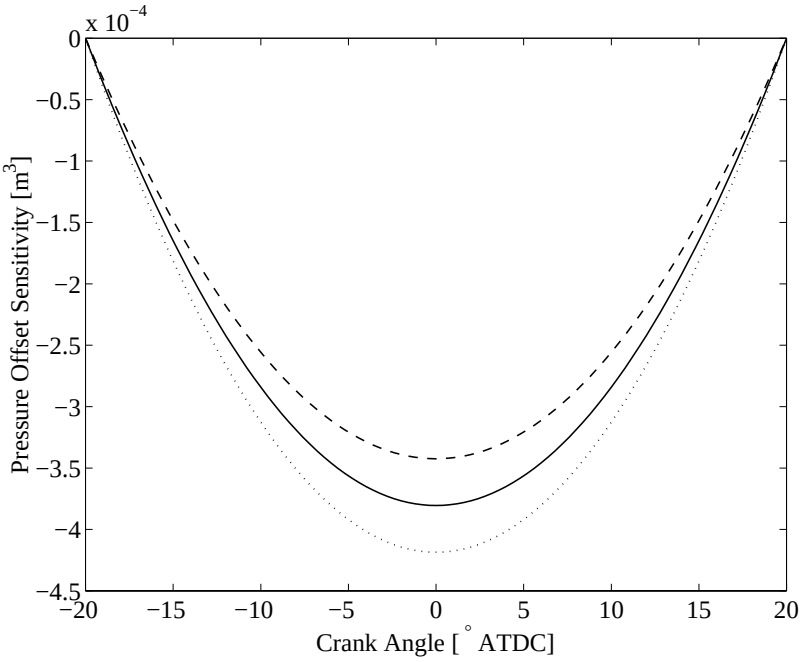

Figure 4.12: Heat release duration in crank angle degrees for 250 consecutive cycles using $\frac{\tilde{c}_v}{\tilde{R}} = 3.5$ (dashed line), and $\frac{\tilde{c}_v}{\tilde{R}} = 4.0$ (solid line), and $\frac{\tilde{c}_v}{\tilde{R}} = 4.5$ (dotted line).

chapter 5 it will be shown that the offset error after removal of the sensor offset is of the order 10^4 Pa, so the maximum error due to a pressure offset will be less than 10 J, which is negligible compared to the total heat release values of the order 10^3 J.

Computational Cost

In practice the heat release equation (4.28) is computed as a finite sum rather than a continuous integral. The finite sum representation is

$$(Q_{ch})_i = \frac{c_v}{\tilde{R}}[p_i V_i - p_0 V_0] + \sum_{j=0}^{i} p_j (\Delta V)_j \tag{4.41}$$

If it is assumed that the crank-angle window over which heat release is computed contains k pressure samples, the cost of computing the sum is k multiplications and $k-1$ additions. Additionally, for each i, two additions and two multiplications have to be performed. Thus, to produce the whole heat release profile,

$$(Q_{ch})_i,\ i = 0, \ldots k-1 \tag{4.42}$$

requires approximately $3k$ multiplications and $3k$ additions. For example, using a 90-degree heat-release window, and a crank resolution of 1 sample per crank angle degree, the computational cost of producing the whole heat release profile is 540 arithmetic operations.

Chapter 5

Estimation of Cylinder-Pressure Sensor Offset

5.1 Introduction

5.1.1 Problem Statement

Crank angle resolved cylinder pressure measurement on internal combustion engines can be made using various kinds of transducer types, of which the piezoelectric, and the optical transducer types are the most prevalent. Both of these sensor types are available in a wide range of sizes to suit different applications. Their bandwidth limitations are adequate to capture the relevant information in the cylinder pressure trace. All suitable transducer types share one unattractive characteristic, though, in that their DC offset varies in an unpredictable way with time. Figure 5.1 shows an example of cylinder pressure data for one full cycle before the offset has been removed. Note e.g. that the indicated pressure during the whole intake stroke is negative.

5.1.2 Problem Solution

This chapter develops a method to estimate and remove the offset from the cylinder pressure measurements. The method amounts to solving the nonlinear least-squares problem of fitting the measured pressure data to a polytropic compression curve. The method, which is applicable to any least-squares problem for which the residual function shows a nonlinear dependence on exactly one of the parameters. By solving the linear least-

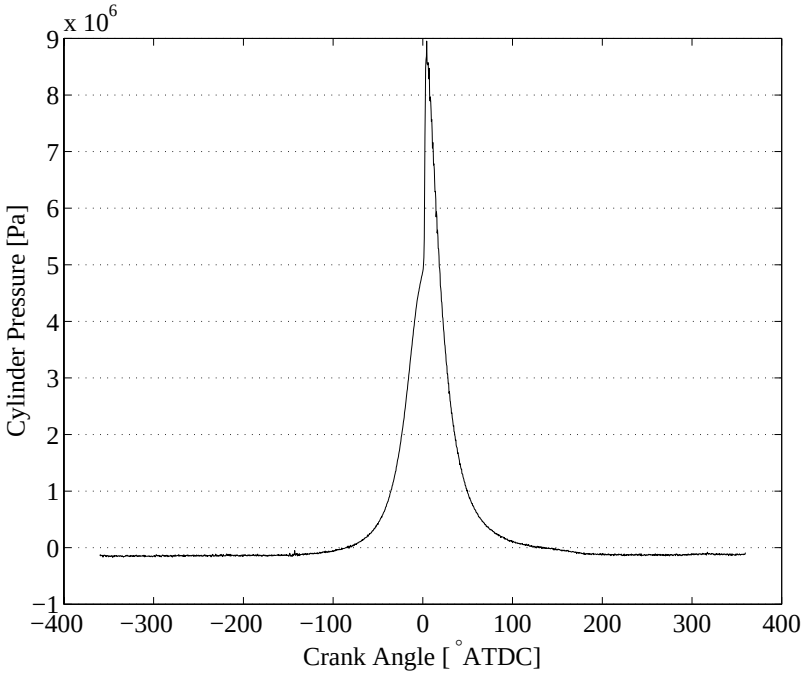

Figure 5.1: Full cycle of cylinder pressure measurements. The fact that the measurements are negative during the intake stroke clearly indicates that the sensor has an offset.

squares problem which results from assuming that the parameter causing the nonlinearity is known, the problem is reduced to minimizing a function of one variable. For this purpose, a finite difference Newton method is proposed, and its superlinear convergence properties are proved.

5.2 Transducer Types

5.2.1 The Piezoelectric Transducer

The physical principle behind piezoelectric pressure transducers is the piezoelectric effect, first discovered by Pierre and Jacques Curie in 1880. The piezoelectric effect causes a quartz crystal to become electrically charged when there is a change in the external forces acting on it (see figure 5.2).

When using a piezoelectric transducer as the sensing element in a data acquisition system, the element has to be connected to a charge amplifier, which converts the electrical charge to a voltage or a current. For the piezoelectric transducer type, the DC

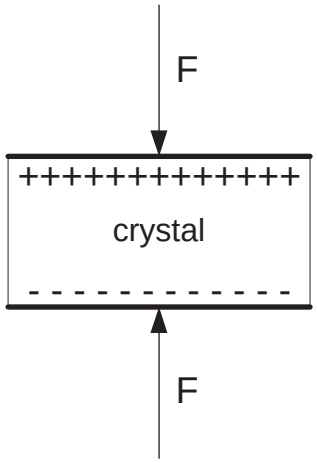

Figure 5.2: Illustration of a piezoelectric crystal (e.g. quartz) with a force being applied to it. When the force is applied to the crystal, the electrons within the crystal redistribute to make one side of the crystal positively charged and the other negatively charged.

offset variation is produced by the charge amplifier which is a necessary component in a pressure sampling system using this type of transducer. The charge amplifier necessarily has some leakage current, which causes the amplifier output to drift over time. This drift is compensated for by a high-pass filter. If the time constant of the high-pass filter is high enough, the filter dominates the drift, and the DC gain of the amplifier is zero. If, on the other hand, the time constant of the filter is low enough, the drift will eventually cause the amplifier output to saturate. Also, thermal stress on the sensing element can distort the measurements.

5.2.2 The Optical Transducer Type

An optical pressure transducer uses an LED, one or several optical fibers, and a photodetector to measure the light intensity reflected from a metal diaphragm, as it deflects under pressure [51, 50]. The optical pressure transducer has the advantage of being inexpensive compared to the piezoelectric type, since LEDs, optical fibers, and photodetectors are all inexpensive components. Furthermore it does not require a charge amplifier to interface with a data acquisition system. For this transducer type, the variation in DC offset is a mechanical phenomenon caused by e.g. thermal stress, aging, and bending of optical

fibers.

5.3 Thermodynamic Analysis of the Compression Stroke

During the compression stroke, both exhaust valves and intake valves are closed, so neglecting crevice effects, there is no mass transfer to or from the combustion chamber. The thermodynamic system which needs to be analyzed, like when analyzing the combustion process (see figure 4.1), consists of the gas contained in the combustion chamber during the compression stroke.

The same equations are valid during the compression stroke as during combustion. During compression though, no chemical reactions are taking place, so $\mathrm{d}n = 0$ identically. Thus, (4.15) simplifies to

$$\frac{\tilde{c}_v}{\tilde{R}} V \mathrm{d}p + \frac{\tilde{c}_p}{\tilde{R}} p \mathrm{d}V - \delta Q = 0 \tag{5.1}$$

During the compression stroke, temperature, pressure, and gas velocities are fairly low. Thus, according to (4.19) and (4.20), there will be little heat exchange with the cylinder walls. Consequently, in the following analysis, the δQ term in (5.1) is assumed to be zero.

Now, equation (5.1) can be rewritten as

$$\frac{\mathrm{d}p}{p} = -\gamma \frac{\mathrm{d}V}{V} \tag{5.2}$$

where γ is the specific heat ratio, $\tilde{c}_p/\tilde{c}_v$. Figure 5.3 shows how γ varies with temperature over an interval which is relevant for the compression stroke. Since γ varies only by a few percent over the whole temperature range it is assumed to be constant. With γ constant, (5.2) can be integrated analytically,

$$\int_{p_0}^{p} \frac{\mathrm{d}p}{p} = -\gamma \int_{V_0}^{V} \frac{\mathrm{d}V}{V}$$

$$\ln\left(\frac{p}{p_0}\right) = -\gamma \ln\left(\frac{V}{V_0}\right)$$

to yield

$$\frac{p}{p_0} = \left(\frac{V}{V_0}\right)^{-\gamma} \tag{5.3}$$

which is the relationship between pressure and volume for an isentropic process.

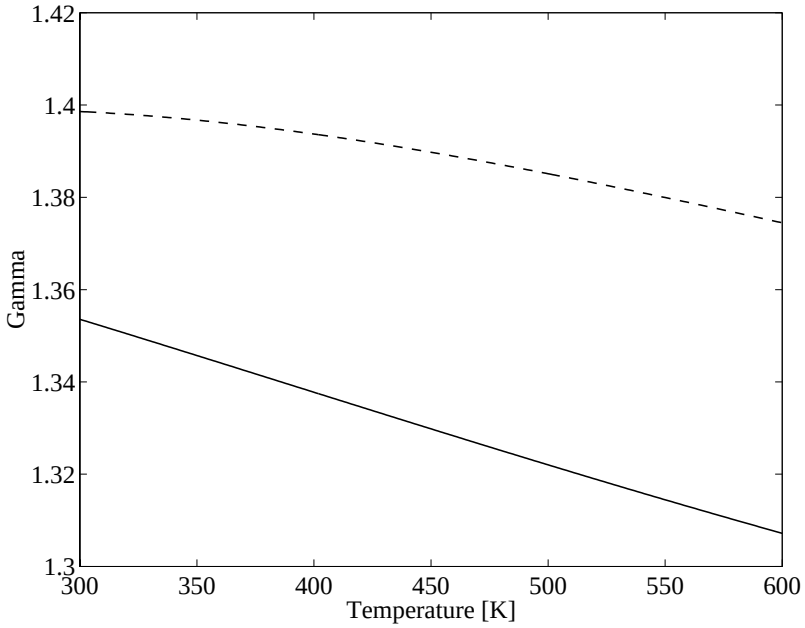

Figure 5.3: Specific heat ratio, γ, as function of temperature for a) Air (dashed line), and b) Stoichiometric mixture of iso-octane and air (solid line).

It is worth noting here, that there is a certain class of processes with $\delta Q \neq 0$, for which an equation of the form (5.2), is still satisfied. This class is defined by the condition

$$\delta Q = aV\mathrm{d}p + bp\mathrm{d}V \tag{5.4}$$

where, a and b can be functions of temperature. Applying (5.4) to equation (5.1) yields

$$\left(\frac{\tilde{c}_v}{\tilde{R}} - a\right) V\mathrm{d}p + \left(\frac{\tilde{c}_p}{\tilde{R}} - b\right) p\mathrm{d}V = 0$$

which can be rewritten as

$$\frac{\mathrm{d}p}{p} = -\kappa\frac{\mathrm{d}V}{V} \tag{5.5}$$

with

$$\kappa = \frac{\frac{\tilde{c}_p}{\tilde{R}} - b}{\frac{\tilde{c}_v}{\tilde{R}} - a}$$

A process which satisfies (5.5) is called a polytropic process, and κ is called the polytropic exponent. Important examples of polytropic processes are, isochoric (V constant), isobaric (p constant), isothermal (T constant), and adiabatic (isentropic) ($\delta Q = 0$) processes.

In the following analysis, in order to emphasize the generality, a polytropic compression process is assumed and hence, γ is replaced by κ. Experiments (see section 5.4.4) show that this model describes the compression process very well.

5.4 Identification of Compression Parameters when κ is Known

5.4.1 Problem Formulation

Assume that cylinder pressure measurements have an unknown but constant offset Δp,

$$p_m = p + \Delta p \tag{5.6}$$

Combining (5.3) and (5.6) yields

$$p_m = \Delta p + CV^{-\kappa} \tag{5.7}$$

where

$$C = p_0 V_0^{\kappa} \tag{5.8}$$

Further assume that κ is known.

Posing the problem as a system identification problem

$$y = \varphi\theta \tag{5.9}$$

where y is known as the output, φ the regressor vector, and θ the parameter vector. Here,

$$y = p_m, \qquad \varphi = \begin{pmatrix} 1 & V^{-\kappa} \end{pmatrix}, \text{and} \qquad \theta = \begin{pmatrix} \Delta p \\ C \end{pmatrix} \tag{5.10}$$

Assume crank-angle resolved data is available for cylinder pressure and combustion chamber volume during the compression stroke, and form

$$Y = \begin{pmatrix} y_1 \\ \vdots \\ y_n \end{pmatrix} = \begin{pmatrix} (p_m)_1 \\ \vdots \\ (p_m)_n \end{pmatrix} \tag{5.11}$$

$$\Phi = \begin{pmatrix} \varphi_1 \\ \vdots \\ \varphi_n \end{pmatrix} = \begin{pmatrix} 1 & V_1^{-\kappa} \\ \vdots & \vdots \\ 1 & V_n^{-\kappa} \end{pmatrix} \tag{5.12}$$

Combining (5.9), (5.11), and (5.12) yields

$$Y = \Phi\theta \tag{5.13}$$

For equation (5.13) to hold, it is necessary to select a crank angle interval for which (5.3) is valid, i.e. combustion chamber closed, and no combustion taking place. This means that all the data has to be collected between the point where the intake valve closes and the point where combustion starts.

5.4.2 The Least Squares Solution

Due to the fact that the number, n, of cylinder pressure measurements in Y, is normally larger than the number of unknown parameters in θ, which is two, equation (5.13), normally has no solution. It is however, possible, to minimize the residual,

$$D = \Phi\theta - Y$$

in some sense. One appealing way to minimize the residuals, is to minimize them in the least squares sense, i.e. solve the problem

$$\hat{\theta} = \arg\min_{\theta}(D^T D) \tag{5.14}$$

An intuitively appealing way of arriving at the solution to (5.14) is to multiply (5.13) from the left by Φ^T

$$\Phi^T Y = \Phi^T \Phi\theta$$

Assuming that Φ has full column rank, $\Phi^T\Phi$ is an invertible matrix, and multiplication by $\left(\Phi^T\Phi\right)^{-1}$ from the left yields the least squares solution for the parameter vector θ

$$\hat{\theta} = \left(\Phi^T\Phi\right)^{-1}\Phi^T Y = \Phi^+ Y \tag{5.15}$$

where Φ^+ is the Moore-Penrose pseudo inverse of Φ.

This method of solving for θ is highly intuitive, and serves as a good way to remember the expression for the least-squares solution. It does not however, prove anything. The proof that it is in fact the solution to (5.14) can be found e.g. in [14], but is for completeness included here also.

Theorem 5.4.1. *The Least Squares Solution to an Overdetermined System of Linear Equations*

Assume that $A \in \mathbb{C}^{n\times m}$, $b \in \mathbb{C}^n$, *with* $n > m$. *Further assume that* $\text{rank}(A) = m$. *Then the solution,* $\hat{x}$, *to the minimization problem*

$$\hat{x} = \arg\min_x (r^* r)$$

with

$$r = Ax - b$$

can be expressed as

$$\hat{x} = (A^*A)^{-1}A^*b$$

Proof. Let

$$x_m = (A^*A)^{-1}A^*b$$

Compare the squared residuals obtained using an arbitrary x with the squared residuals obtained using x_m

$$\begin{aligned}
\delta &= r^*r - r_m^*r_m = (Ax-b)^*(Ax-b) - (Ax_m-b)^*(Ax_m-b) \\
&= x^*A^*Ax - x^*A^*b - b^*Ax + b^*b - x_m^*A^*Ax_m \\
&+ b^*A(A^*A)^{-1}A^*b + b^*A(A^*A)^{-1}A^*b - b^*b \\
&= x^*A^*Ax - 2b^*Ax + x_m^*A^*Ax_m = x^*A^*Ax - 2b^*A(A^*A)^{-1}(A^*A)x + x_m^*A^*Ax_m \\
&= x^*A^*Ax - 2x_m^*A^*Ax + x_m^*A^*Ax_m = [A(x-x_m)]^*[A(x-x_m)]
\end{aligned}$$

So, since $\text{rank}(A) = m$, $\delta > 0\ \forall x \neq x_m$. □

For the problem at hand, the least-squares solution (5.15) translates to

$$\Phi^T\Phi = \begin{pmatrix} n & \sum_{i=1}^n V_i^{-\kappa} \\ \sum_{i=1}^n V_i^{-\kappa} & \sum_{i=1}^n V_i^{-2\kappa} \end{pmatrix} \tag{5.16}$$

Inverting (5.16) yields

$$\left(\Phi^T\Phi\right)^{-1} = \frac{1}{n\sum_{i=1}^n V_i^{-2\kappa} - \left(\sum_{i=1}^n V_i^{-\kappa}\right)^2} \begin{pmatrix} \sum_{i=1}^n V_i^{-2\kappa} & -\sum_{i=1}^n V_i^{-\kappa} \\ -\sum_{i=1}^n V_i^{-\kappa} & n \end{pmatrix} \tag{5.17}$$

Combining (5.11) and (5.12) yields

$$\Phi^T Y = \begin{pmatrix} \sum_{i=1}^n (p_m)_i \\ \sum_{i=1}^n (p_m)_i V_i^{-\kappa} \end{pmatrix} \tag{5.18}$$

Finally multiplying (5.18) by (5.17) from the left yields

$$\begin{aligned} \hat{\theta} = & \frac{1}{n\sum_{i=1}^n V_i^{-2\kappa} - \left(\sum_{i=1}^n V_i^{-\kappa}\right)^2} \cdot \\ & \cdot \begin{pmatrix} \left(\sum_{i=1}^n V_i^{-2\kappa}\right)\left(\sum_{i=1}^n (p_m)_i\right) - \left(\sum_{i=1}^n V_i^{-\kappa}\right)\left(\sum_{i=1}^n (p_m)_i V_i^{-\kappa}\right) \\ -\left(\sum_{i=1}^n V_i^{-\kappa}\right)\left(\sum_{i=1}^n (p_m)_i\right) + n\sum_{i=1}^n (p_m)_i V_i^{-\kappa} \end{pmatrix} \end{aligned} \tag{5.19}$$

For the individual parameter values, defined in (5.10), (5.19) translates to

$$\Delta p = -\frac{\left(\sum_{i=1}^n V_i^{-\kappa}\right)\left(\sum_{i=1}^n (p_m)_i V_i^{-\kappa}\right) - \left(\sum_{i=1}^n V_i^{-2\kappa}\right)\left(\sum_{i=1}^n (p_m)_i\right)}{n\sum_{i=1}^n V_i^{-2\kappa} - \left(\sum_{i=1}^n V_i^{-\kappa}\right)^2} \tag{5.20}$$

$$C = \frac{n\sum_{i=1}^n (p_m)_i V_i^{-\kappa} - \left(\sum_{i=1}^n V_i^{-\kappa}\right)\left(\sum_{i=1}^n (p_m)_i\right)}{n\sum_{i=1}^n V_i^{-2\kappa} - \left(\sum_{i=1}^n V_i^{-\kappa}\right)^2} \tag{5.21}$$

5.4.3 Statistical Properties of the Least-Squares Estimate

In order to analyze the statistics of the least-squares estimate (5.15), assume that Y is a random vector defined by

$$Y = \Phi\theta + V \tag{5.22}$$

where V is a vector of Gaussian random variables s.t.

$$E(V) = 0, \quad \text{and} \quad E(VV^T) = \sigma^2 I \tag{5.23}$$

Thus, using (5.22) and (5.23)

$$E(Y) = \Phi\theta \tag{5.24}$$

and

$$\begin{aligned} E(YY^T) &= E[(\Phi\theta + V)(\Phi\theta + V)^T] \\ &= \Phi\theta\theta^T\Phi^T + \Phi\theta E(V^T) + E(V)\theta^T\Phi^T + E(VV^T) = \Phi\theta\theta^T\Phi^T + \sigma^2 I \end{aligned} \tag{5.25}$$

The least-squares estimate $\hat{\theta}$, given by (5.15) is now considered as a random vector, and its expected value can be evaluated

$$E(\hat{\theta}) = E[\left(\Phi^T\Phi\right)^{-1}\Phi^T(\Phi\theta + V)] = \left(\Phi^T\Phi\right)^{-1}\Phi^T\Phi\theta + E(\left(\Phi^T\Phi\right)^{-1}\Phi^T V) = \theta + \left(\Phi^T\Phi\right)^{-1}\Phi^T E(V) = \theta \quad (5.26)$$

Thus the estimate is consistent.

The covariance of the estimation error can also be evaluated using (5.25) and (5.26)

$$\begin{aligned} \mathrm{Cov}(\hat{\theta} - \theta) &= E[(\hat{\theta} - \theta)(\hat{\theta} - \theta)^T] = E(\hat{\theta}\hat{\theta}^T) - \theta\theta^T \\ &= E[\left(\Phi^T\Phi\right)^{-1}\Phi^T Y Y^T \Phi \left(\Phi^T\Phi\right)^{-1}] - \theta\theta^T \\ &= \left(\Phi^T\Phi\right)^{-1}\Phi^T E(YY^T)\Phi \left(\Phi^T\Phi\right)^{-1} - \theta\theta^T \\ &= \left(\Phi^T\Phi\right)^{-1}\Phi^T[\Phi\theta\theta^T\Phi^T + \sigma^2 I]\Phi \left(\Phi^T\Phi\right)^{-1} - \theta\theta^T \\ &= \theta\theta^T + \left(\Phi^T\Phi\right)^{-1}\sigma^2 - \theta\theta^T = \left(\Phi^T\Phi\right)^{-1}\sigma^2 \end{aligned} \quad (5.27)$$

In order to understand what this means in terms of the variances of the individual estimates for ΔP and C, a closer investigation of the diagonal elements of $\left(\Phi^T\Phi\right)^{-1}$ is necessary. Using (5.17), the variance of Δp is found to be

$$\mathrm{Var}(\Delta p) = \frac{\sum_{i=1}^n V_i^{-2\kappa}}{n\sum_{i=1}^n V_i^{-2\kappa} - \left(\sum_{i=1}^n V_i^{-\kappa}\right)^2}\sigma^2 \quad (5.28)$$

and the variance of C is

$$\mathrm{Var}(C) = \frac{n}{n\sum_{i=1}^n V_i^{-2\kappa} - \left(\sum_{i=1}^n V_i^{-\kappa}\right)^2}\sigma^2 \quad (5.29)$$

Analyzing the denominator, d, of these expressions yields

$$d = n\sum_{i=1}^n V_i^{-2\kappa} - \left(\sum_{i=1}^n V_i^{-\kappa}\right)^2 = \sum_{i=2}^n\sum_{j=1}^{i-1}(V_i^{-\kappa} - V_j^{-\kappa})^2 \quad (5.30)$$

An approximation for this expression can be obtained by investigating the case of the $V_i^{-\kappa}$'s being evenly spaced between $V_1^{-\kappa}$ and $V_n^{-\kappa}$. Then, with r defined by

$$r = \frac{V_n^{-\kappa} - V_1^{-\kappa}}{n-1} \quad (5.31)$$

$$\begin{aligned} d &= \sum_{i=2}^{n}\sum_{j=1}^{i-1}(jr)^2 = r^2\sum_{i=2}^{n}\sum_{j=1}^{i-1}j^2 = r^2\sum_{i=2}^{n}\left[\frac{(i-1)^3}{3}+\frac{(i-1)^2}{2}+\frac{i-1}{6}\right] \\ &= r^2\sum_{i=1}^{n-1}\left(\frac{i^3}{3}+\frac{i^2}{2}+\frac{i}{6}\right) = r^2 O(n^4) \end{aligned} \tag{5.32}$$

Thus, by applying (5.31)

$$d = O(n^2) \tag{5.33}$$

Now, since the combustion chamber volume decreases during compression, $V_i^{-\kappa} \leq V_n^{-\kappa}\ \forall i$, so

$$\mathrm{Var}(\Delta p) = O\left(\frac{1}{n}\right)\sigma^2 \tag{5.34}$$

and

$$\mathrm{Var}(C) = O\left(\frac{1}{n}\right)\sigma^2 \tag{5.35}$$

Figures 5.4 and 5.5 show standard deviations of the estimates for Δp and p_0 respectively predicted from (5.28), (5.29), and (5.8). The dependence of these standard deviations on n, predicted by the approximate formulas (5.34) and (5.35) are also plotted for comparison. It can be seen that these approximations are quite accurate for large values of n, and can thus be used for a quick approximation of how many samples are required for the desired accuracy.

5.4.4 Experimental Results

Figure 5.6 shows the result of applying the presented offset estimation method to the compression stroke of an HCCI engine, with compression ratio 18:1. Estimation is performed based on cylinder- pressure measurements between 135° and 40° before top dead center, and the crank-angle resolution of the pressure sampling is 2.5 samples per degree. The standard deviation of the residual is approximately 500 Pa (see figure 5.7) which is roughly the noise level of the measured pressure signal. Figure 5.8 shows the cylinder pressure during the intake stroke of the same cycle, compared with the pressure measured in the intake manifold. The correspondence between the pressure measured in the intake manifold and the pressure measured in the cylinder is good. The spike in the cylinder pressure around $-140\,^\circ$ is noise from when the intake valve closes.

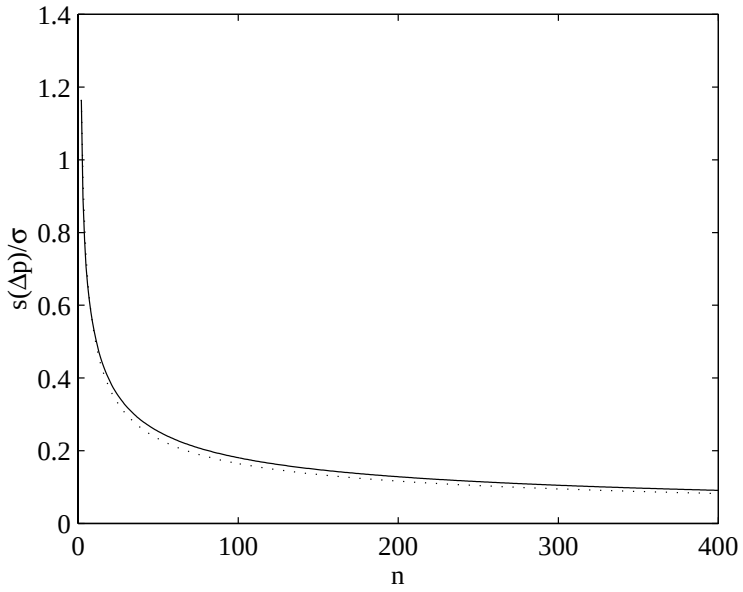

Figure 5.4: Standard deviation of Δp divided by standard deviation of pressure samples (solid line) plotted versus the number of samples, n. Dotted line plots $a/\sqrt{n}$ with a suitable constant a for comparison.

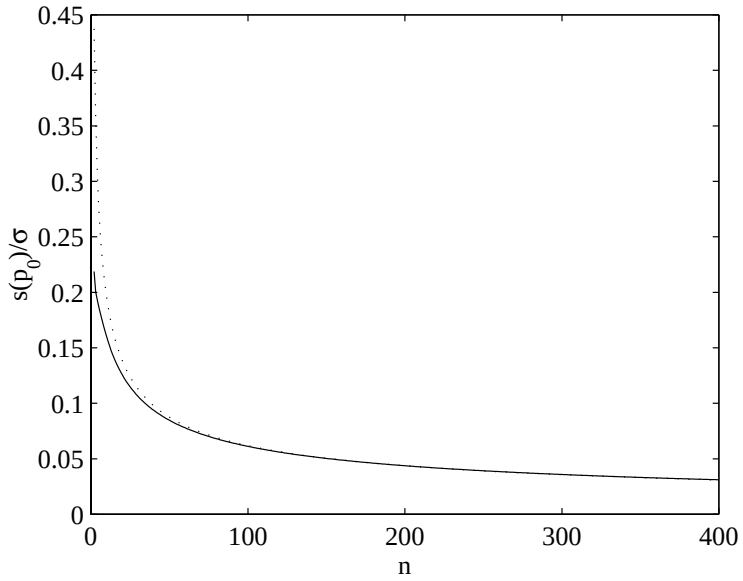

Figure 5.5: Standard deviation of initial pressure , p_0, divided by standard deviation of pressure samples (solid line) plotted versus the number of samples, n. Dotted line plots $a/\sqrt{n}$ with a suitable constant a for comparison.

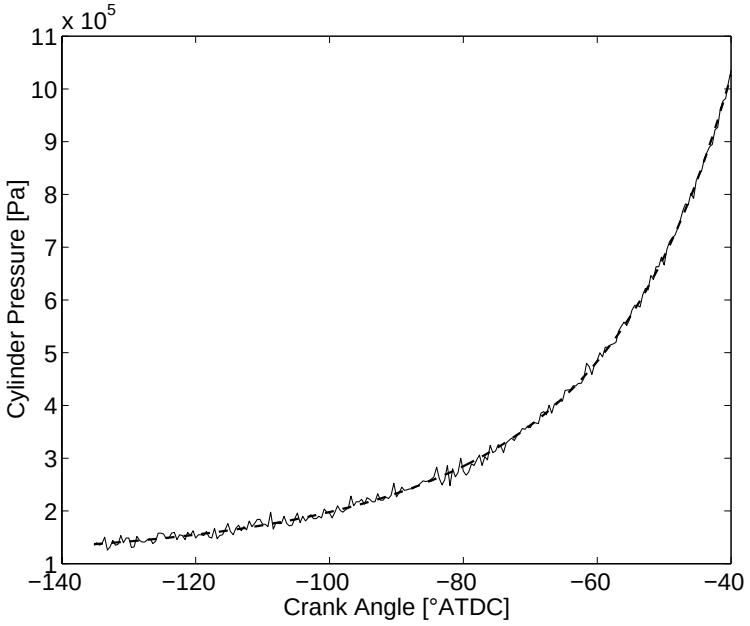

Figure 5.6: Cylinder pressure (solid line), fitted to adiabatic compression curve (dashed line). HCCI Engine with compression ratio 18:1. $\kappa = 1.321$. Fuel mixture of iso-octane and n-heptane.

Even though κ can, with good precision, be assumed to be constant during the compression stroke, it is not constant from cycle to cycle. These variations can be caused e.g. by changes in inlet conditions or operating conditions, such as addition of EGR. Since the dependence of κ on operating conditions can be fairly complex, it may be necessary to estimate κ also. This is covered in section 5.5.

5.5 Estimation of the Polytropic Exponent

5.5.1 Definition of the Loss Function

As mentioned above, it is likely that κ is not known *a priori*. In this case it will be necessary to estimate κ as well. One way of estimating κ is to minimize the RMS error of the pressure trace with respect to κ, i.e.

$$\hat{\kappa} = \arg\min_{\kappa} \left(D^T D \right), \tag{5.36}$$

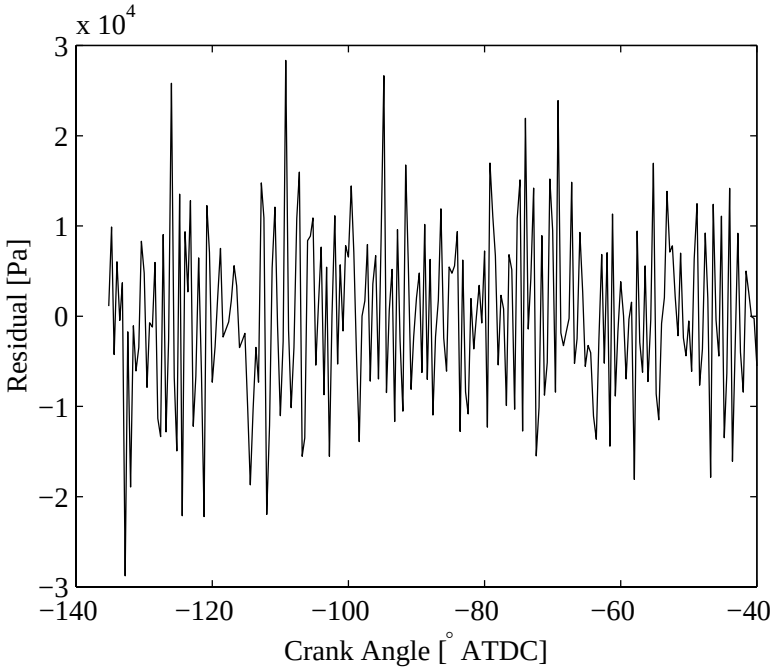

Figure 5.7: Residual of the least-squares fit of figure 5.6.

where

$$D = Y - \Phi\theta = Y - \Phi\left(\Phi^T\Phi\right)^{-1}\Phi^T Y = \left[I - \Phi\left(\Phi^T\Phi\right)^{-1}\Phi^T\right]Y = PY \tag{5.37}$$

and

$$P = \left[I - \Phi\left(\Phi^T\Phi\right)^{-1}\Phi^T\right] \tag{5.38}$$

It is noted here that P is a symmetric projection matrix, i.e.

$$P^T = P \tag{5.39}$$

and

$$\begin{aligned} P^2 &= \left[I - \Phi\left(\Phi^T\Phi\right)^{-1}\Phi^T\right]\left[I - \Phi\left(\Phi^T\Phi\right)^{-1}\Phi^T\right] \\ &= \left[I - 2\Phi\left(\Phi^T\Phi\right)^{-1}\Phi^T + \Phi\left(\Phi^T\Phi\right)^{-1}\Phi^T\Phi\left(\Phi^T\Phi\right)^{-1}\Phi^T\right] \\ &= \left[I - \Phi\left(\Phi^T\Phi\right)^{-1}\Phi^T\right] = P \end{aligned} \tag{5.40}$$

Using (5.37) and (5.39), define the loss function

$$J = D^T D = Y^T P^T P Y = Y^T P Y \tag{5.41}$$

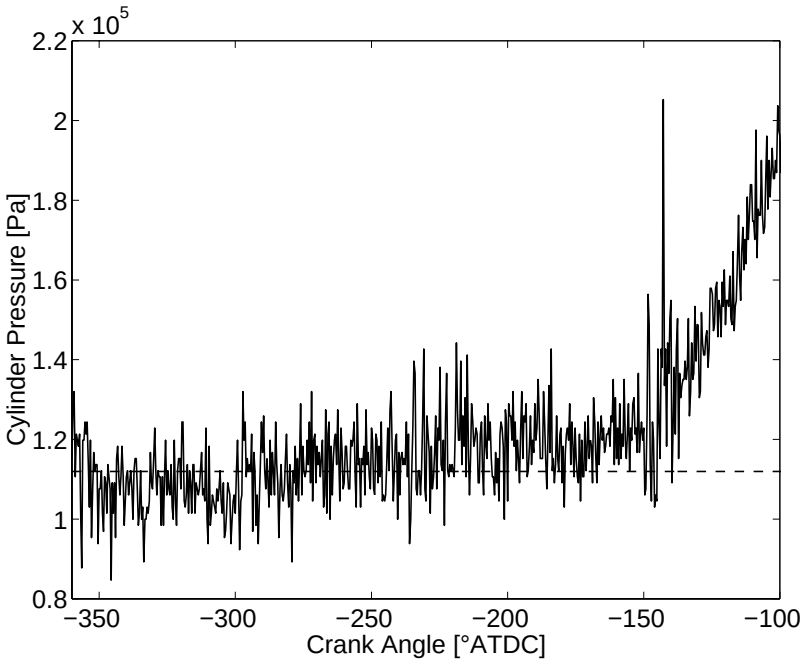

Figure 5.8: Cylinder pressure (solid line) during the intake stroke of the same cycle as in figure 5.6. The dashed line shows the average pressure measured in the intake manifold.

5.5.2 Differential Analysis of the Loss Function

The minimum of J can be characterized by

$$\left.\frac{\mathrm{d}J}{\mathrm{d}\kappa}\right|_{\kappa=\hat{\kappa}} = 0 \tag{5.42}$$

Differentiate J, noting that Y is independent of κ

$$\frac{\mathrm{d}J}{\mathrm{d}\kappa} = Y^T \frac{\mathrm{d}P}{\mathrm{d}\kappa} Y \tag{5.43}$$

$$\begin{aligned}
\frac{\mathrm{d}P}{\mathrm{d}\kappa} = -\frac{\mathrm{d}}{\mathrm{d}\kappa}\left[\Phi\left(\Phi^T\Phi\right)^{-1}\Phi^T\right] = \\
-\frac{\mathrm{d}\Phi}{\mathrm{d}\kappa}\left(\Phi^T\Phi\right)^{-1}\Phi^T + \Phi\left(\Phi^T\Phi\right)^{-1}\left(\frac{\mathrm{d}\Phi^T}{\mathrm{d}\kappa}\Phi + \Phi^T\frac{\mathrm{d}\Phi}{\mathrm{d}\kappa}\right) - \Phi\left(\Phi^T\Phi\right)^{-1}\frac{\mathrm{d}\Phi^T}{\mathrm{d}\kappa} = \\
-\frac{\mathrm{d}\Phi}{\mathrm{d}\kappa}\left(\Phi^T\Phi\right)^{-1}\Phi^T + \Phi\left(\Phi^T\Phi\right)^{-1}\Phi^T\frac{\mathrm{d}\Phi}{\mathrm{d}\kappa}\left(\Phi^T\Phi\right)^{-1}\Phi^T \\
-\Phi\left(\Phi^T\Phi\right)^{-1}\frac{\mathrm{d}\Phi^T}{\mathrm{d}\kappa} + \Phi\left(\Phi^T\Phi\right)^{-1}\frac{\mathrm{d}\Phi^T}{\mathrm{d}\kappa}\Phi\left(\Phi^T\Phi\right)^{-1}\Phi^T = \\
-P\frac{\mathrm{d}\Phi}{\mathrm{d}\kappa}\left(\Phi^T\Phi\right)^{-1}\Phi^T - \Phi\left(\Phi^T\Phi\right)^{-1}\frac{\mathrm{d}\Phi^T}{\mathrm{d}\kappa}P
\end{aligned} \tag{5.44}$$

Define A,

$$A = \frac{\mathrm{d}\Phi}{\mathrm{d}\kappa}\left(\Phi^T\Phi\right)^{-1}\Phi^T \tag{5.45}$$

then $\mathrm{d}J/\mathrm{d}\kappa$ can be expressed as

$$\frac{\mathrm{d}J}{\mathrm{d}\kappa} = -Y^T\left(PA + A^TP\right)Y = -2Y^TPAY \tag{5.46}$$

Combining (5.43), (5.44), and (5.15) results in a simple expression for $\mathrm{d}J/\mathrm{d}\kappa$.

$$\frac{\mathrm{d}J}{\mathrm{d}\kappa} = -2Y^TP\frac{\mathrm{d}\Phi}{\mathrm{d}\kappa}\left(\Phi^T\Phi\right)^{-1}\Phi^TY = -2D^T\frac{\mathrm{d}\Phi}{\mathrm{d}\kappa}\theta \tag{5.47}$$

Using (5.12),

$$\frac{\mathrm{d}\Phi}{\mathrm{d}\kappa} = \begin{pmatrix} 0 & -V_1^{-\kappa}\ln V_1 \\ \vdots & \vdots \\ 0 & -V_n^{-\kappa}\ln V_n \end{pmatrix} \tag{5.48}$$

So finally, using (5.10)

$$\frac{\mathrm{d}J}{\mathrm{d}\kappa} = 2CD^T\begin{pmatrix} V_1^{-\kappa}\ln V_1 \\ \vdots \\ V_n^{-\kappa}\ln V_n \end{pmatrix} \tag{5.49}$$

Figures 5.9 and 5.10 show J and $\mathrm{d}J/\mathrm{d}\kappa$ respectively plotted versus κ. The dependence of J on κ is nearly quadratic, so a Newton method should converge to the minimum in just a few steps.

An analytic expression for $\mathrm{d}^2J/\mathrm{d}\kappa^2$ is required for solving the optimization problem using the original Newton method. The analytic expression for $\frac{\mathrm{d}(PA)}{\mathrm{d}\kappa}$ is shown in equation (5.50).

$$\frac{\mathrm{d}\left(PA\right)}{\mathrm{d}\kappa} = -2PA^2 - A^TPA + P\frac{\mathrm{d}^2J}{\mathrm{d}\kappa^2}\left(\Phi^T\Phi\right)^{-1}\Phi^T + P\frac{\mathrm{d}\Phi}{\mathrm{d}\kappa}\left(\Phi^T\Phi\right)^{-1}\frac{\mathrm{d}\Phi^T}{\mathrm{d}\kappa}P \tag{5.50}$$

Then $\mathrm{d}^2J/\mathrm{d}\kappa^2$ can be obtained as

$$\frac{\mathrm{d}^2J}{\mathrm{d}\kappa^2} = -2Y^T\frac{\mathrm{d}\left(PA\right)}{\mathrm{d}\kappa}Y \tag{5.51}$$

This analytic expression for $\mathrm{d}^2J/\mathrm{d}\kappa^2$ is of limited use though, because of the computational cost.

Figure 5.11 shows $\mathrm{d}^2J/\mathrm{d}\kappa^2$ as a function of κ, and it can be seen that it is almost constant. The variation in $\mathrm{d}^2J/\mathrm{d}\kappa^2$ over the relevant range of κ is less than 5%. Thus a finite difference Newton method [14], which estimates the second derivative by a finite difference of first derivatives should perform well at finding the minimizer.

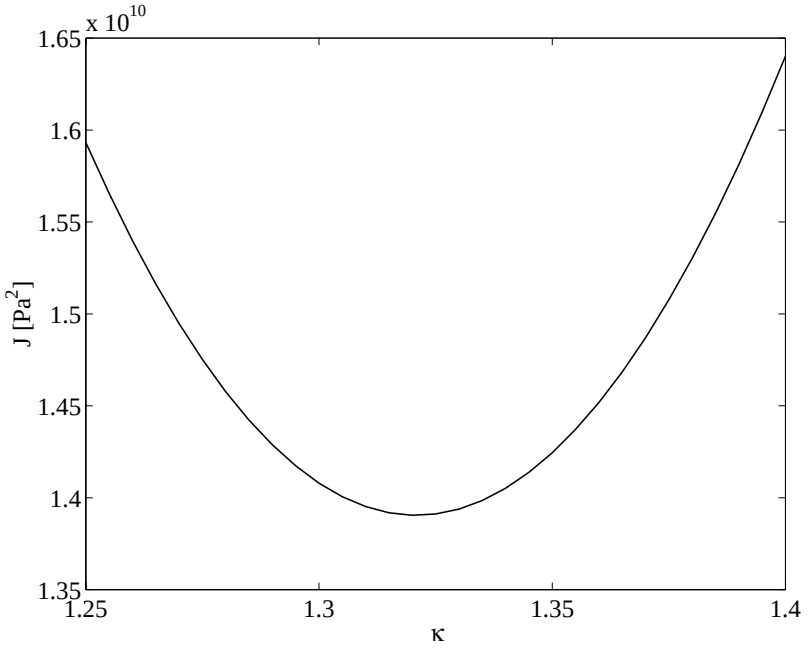

Figure 5.9: J plotted versus κ.

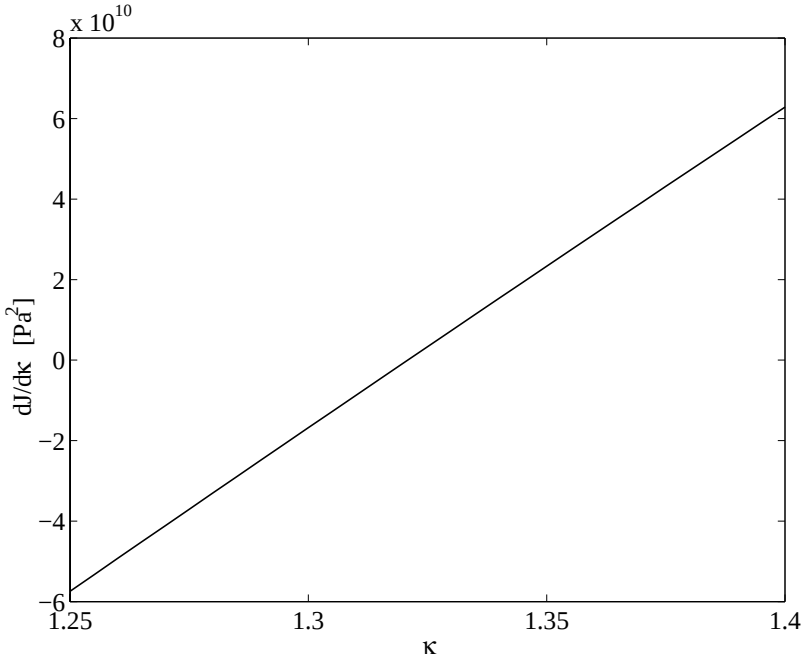

Figure 5.10: $\mathrm{d}J/\mathrm{d}\kappa$ plotted versus κ.

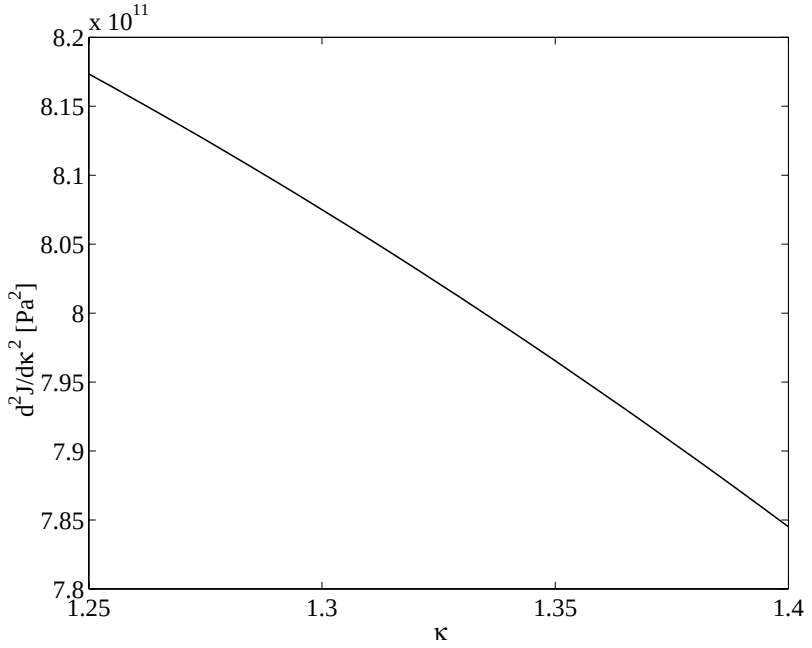

Figure 5.11: $\mathrm{d}^2J/\mathrm{d}\kappa^2$ plotted versus κ.

5.5.3 Newton Methods for Optimization

The Newton Method

The Newton optimization method applied to a scalar-valued, multivariable function $f(\mathbf{x})$, approximates $f(\mathbf{x})$ at step k, with its second order Taylor polynomial

$$f(\mathbf{x}^{(k)} + \boldsymbol{\delta}) \approx \tilde{f}(\boldsymbol{\delta}) = f(\mathbf{x}^{(k)}) + \mathbf{g}(\mathbf{x}^{(k)})\boldsymbol{\delta} + \frac{1}{2}\boldsymbol{\delta}^T\mathbf{G}(\mathbf{x}^{(k)})\boldsymbol{\delta} \tag{5.52}$$

where

$$\mathbf{g} = \frac{\partial f}{\partial \mathbf{x}}$$
$$\mathbf{G} = \frac{\partial g^T}{\partial \mathbf{x}}$$

The method assumes that $\mathbf{x}$ is "close" enough to a local minimum, $\mathbf{x}^*$, in which case the Hessian matrix, $\mathbf{G}(\mathbf{x}^{(k)}) > 0$, i.e. positive definite. $\mathbf{G}(\mathbf{x}^{(k)}) > 0$ implies that $\tilde{f}(\boldsymbol{\delta})$ has a unique minimum.

To find the minimum, calculate the gradient of $\tilde{f}$

$$\frac{\partial \tilde{f}}{\partial \boldsymbol{\delta}} = \mathbf{g}(\mathbf{x}^{(k)}) + \mathbf{G}(\mathbf{x}^{(k)})\boldsymbol{\delta}\ , \tag{5.53}$$

and solve for $\frac{\partial \tilde{f}}{\partial \boldsymbol{\delta}} = 0$. The solution will define the next step in the iteration,

$$\boldsymbol{\delta}^{(k)} = -[\mathbf{G}(\mathbf{x}^{(k)})]^{-1}\mathbf{g}(\mathbf{x}^{(k)}) \,, \tag{5.54}$$

and $\mathbf{x}^{(k+1)}$ is selected as

$$\mathbf{x}^{(k+1)} = \mathbf{x}^{(k)} + \boldsymbol{\delta}^{(k)} \tag{5.55}$$

In [14], it is proved that if $\mathbf{x}^{(k)}$ is sufficiently close to a local minimum, $\mathbf{x}^*$, and $\mathbf{G}(\mathbf{x})$ is locally Lipschitz in a neighborhood of $\mathbf{x}^*$, Newton's method converges to the minimum at second order, i.e.

$$\begin{aligned} &\|\boldsymbol{\epsilon}^{(k+1)}\| \leq a\|\boldsymbol{\epsilon}^{(k)}\|, \quad \text{with} \quad 0 < a < 1, \quad \text{and} \\ &\|\boldsymbol{\epsilon}^{(k+1)}\| \leq c\|\boldsymbol{\epsilon}^{(k)}\|^2 \end{aligned} \tag{5.56}$$

where the error is defined as

$$\boldsymbol{\epsilon}^{(k)} = \mathbf{x}^{(k)} - \mathbf{x}^* \tag{5.57}$$

Below, in theorem 5.5.1, this result is restated and proved, at a higher level of mathematical stringency compared to the treatment in [14].

Theorem 5.5.1. *Convergence of the Newton Method*

Assume that $f \in \mathbb{C}^2$ and that the Hessian matrix, $\mathbf{G}$, satisfies a Lipschitz condition $\|\mathbf{G}(\mathbf{y})-\mathbf{G}(\mathbf{x})\|_2 \leq l\|\mathbf{y}-\mathbf{x}\|_2$ in a neighborhood, N, of a local minimizer, $\mathbf{x}^*$. Further assume that $mI < \mathbf{G}(\mathbf{x}^*) < MI$. Then, if $\mathbf{x}^{(0)} \in N$ satisfies $\|\boldsymbol{\epsilon}^{(0)}\|_2 \leq m/(2l)$, the Newton method converges at a quadratic rate.

Proof. Applying the mean value theorem and the fact that $\mathbf{x}^*$ is a local minimum,

$$0 = \mathbf{g}(\mathbf{x}^*) = \mathbf{g}(\mathbf{x}^{(k)} - \boldsymbol{\epsilon}^{(k)}) = \mathbf{g}(\mathbf{x}^{(k)}) - \mathbf{G}(\boldsymbol{\theta})\boldsymbol{\epsilon}^{(k)} \tag{5.58}$$

where $\boldsymbol{\theta} = s\mathbf{x}^* + (1-s)\mathbf{x}^{(k)}$, and $0 \leq s \leq 1$. Rearranging yields,

$$0 = \mathbf{g}(\mathbf{x}^{(k)}) - \mathbf{G}(\mathbf{x}^{(k)})\boldsymbol{\epsilon}^{(k)} + [\mathbf{G}(\boldsymbol{\theta}) - \mathbf{G}(\mathbf{x}^{(k)})]\boldsymbol{\epsilon}^{(k)} \tag{5.59}$$

Multiplication by $(\mathbf{G}(\mathbf{x}^{(k)}))^{-1}$ from the left yields

$$\begin{aligned} 0 &= [\mathbf{G}(\mathbf{x}^{(k)})]^{-1}\mathbf{g}(\mathbf{x}^{(k)}) - \boldsymbol{\epsilon}^{(k)} + [\mathbf{G}(\mathbf{x}^{(k)})]^{-1}[\mathbf{G}(\boldsymbol{\theta}) - \mathbf{G}(\mathbf{x}^{(k)})]\boldsymbol{\epsilon}^{(k)} \\ &= -\boldsymbol{\delta}^{(k)} - \boldsymbol{\epsilon}^{(k)} + [\mathbf{G}(\mathbf{x}^{(k)})]^{-1}[\mathbf{G}(\boldsymbol{\theta}) - \mathbf{G}(\mathbf{x}^{(k)})]\boldsymbol{\epsilon}^{(k)} \\ &= -\boldsymbol{\epsilon}^{(k+1)} + [\mathbf{G}(\mathbf{x}^{(k)})]^{-1}[\mathbf{G}(\boldsymbol{\theta}) - \mathbf{G}(\mathbf{x}^{(k)})]\boldsymbol{\epsilon}^{(k)} \end{aligned} \tag{5.60}$$

Taking norms yields

$$\begin{aligned}\|\boldsymbol{\epsilon}^{(k+1)}\|_2 &\leq \|[\mathbf{G}(\mathbf{x}^{(k)})]^{-1}\|_2 \cdot \|\mathbf{G}(\boldsymbol{\theta}) - \mathbf{G}(\mathbf{x}^{(k)})\|_2 \cdot \|\boldsymbol{\epsilon}^{(k)}\|_2 \\ &\leq \|[\mathbf{G}(\mathbf{x}^{(k)})]^{-1}\|_2 \cdot l \cdot \|\boldsymbol{\epsilon}^{(k)}\|_2^2 \leq \frac{l}{m - l\|\boldsymbol{\epsilon}^{(k)}\|_2}\|\boldsymbol{\epsilon}^{(k)}\|_2^2\end{aligned} \tag{5.61}$$

Now, if $\|\boldsymbol{\epsilon}^{(k)}\|_2 < am/[(a+1)l]$, (5.61) yields

$$\|\boldsymbol{\epsilon}^{(k+1)}\|_2 \leq a\|\boldsymbol{\epsilon}^{(k)}\|_2 \tag{5.62}$$

So, selecting $0 < a < 1$, convergence is ensured by induction. Furthermore,

$$\|\boldsymbol{\epsilon}^{(k+1)}\|_2 \leq \frac{2l}{m}\|\boldsymbol{\epsilon}^{(k)}\|_2^2 \tag{5.63}$$

which ensures quadratic convergence. □

The Finite Difference Newton Method

In the case that an analytic expression for the second derivative is not available or, as in this case, it is too expensive to compute, a modified version of the Newton method can be applied. The method used here is called the finite difference Newton method, and estimates the second derivative by a finite difference of first derivatives. Thus, the second derivative at x_k is approximated by

$$G(x_k) \approx \frac{g(x_k) - g(x_{k-1})}{\delta_{k-1}} \tag{5.64}$$

Since $g(x_k)$ and $g(x_{k-1})$ are computed anyway, the additional computational effort required for estimating the second derivative is very small.

It remains to be shown that the finite difference Newton method converges. This is done in theorem 5.5.2. Note that this theorem is valid for functions of one variable only. First, the method is defined

$$\begin{aligned}H_k &= \frac{g(x_k) - g(x_{k-1})}{\delta_{k-1}} \\ \delta_k &= -\frac{g(x_k)}{H_k}\end{aligned}$$

Theorem 5.5.2. *Convergence of the finite difference Newton method.*

Assume that $f \in \mathbb{C}^2$, and that the second derivative, G, satisfies a Lipschitz condition, $|G(y) - G(x)| \leq l|y - x|$, in a neighborhood, N, of a local minimizer, x^*. Assume that

$m < G(x^*) < M$, with $0 < m < M$. If $x_0 \in N$, δ_0 is restricted to $0 < |\delta_0| \leq r$, $r < m/(2l)$, and x_0 is selected s.t. $|\epsilon_0| \leq m/(2l) - r$. Then the finite difference Newton method is well defined for all k, and converges superlinearly.

Proof. Applying the mean-value theorem to g,

$$g(x_{k-1}) = g(x_k) - G(\theta)\delta_{k-1}, \quad \text{with} \quad \theta \in [x_k, x_{k-1}]$$

Rearrange,

$$g(x_{k-1}) = g(x_k) - G(x_k)\delta_{k-1} - [G(\theta) - G(x_k)]\delta_{k-1}$$

Solve for $G(x_k)$,

$$G(x_k) = \frac{g(x_k - g(x_{k-1}}{\delta_{k-1}} - [G(\theta) - G(x_k)] = H_k - [G(\theta) - G(x_k)]$$

Now, apply the mean-value theorem on g a second time

$$0 = g(x^*) = g(x_k - \epsilon_k) = g(x_k) - G(\phi)\epsilon_k, \quad \text{with} \quad \phi \in [x^*, x_k]$$

Rearrange,

$$\begin{aligned} 0 &= g(x_k) - G(x_k)\epsilon_k - [G(\phi) - G(x_k)]\epsilon_k \\ &= g(x_k) - H_k\epsilon_k + [G(\theta) - G(x_k)]\epsilon_k - [G(\phi) - G(x_k)]\epsilon_k \\ &= g(x_k) - H_k\epsilon_k + [G(\theta) - G(\phi)]\epsilon_k \end{aligned}$$

Divide by H_k, assuming that $H_k > 0$

$$\begin{aligned} 0 &= \frac{g(x_k)}{H_k} - \epsilon_k + \frac{\epsilon_k}{H_k}[G(\theta) - G(\phi)] = -\delta_k - \epsilon_k + \frac{\epsilon_k}{H_k}[G(\theta) - G(\phi)] \\ &= -\epsilon_{k+1} + \frac{\epsilon_k}{G(x_k) + [G(\theta) - G(\phi)]}[G(\theta) - G(\phi)] \end{aligned}$$

Take absolute values

$$\begin{aligned} |\epsilon_{k+1}| &= \frac{|\epsilon_k|}{G(x_k) + [G(\theta) - G(\phi)]}|G(\theta) - G(\phi)| \leq \frac{|\epsilon_k|}{m - l|\theta - \phi|} l|\theta - \phi| \\ &\leq \frac{|\epsilon_k|}{m - l(|\epsilon_k| + |\epsilon_{k-1}|)} l(|\epsilon_k| + |\epsilon_{k-1}|) \end{aligned} \tag{5.65}$$

Select

$$|\epsilon_0| \leq \frac{am}{(a+1)l} - r \quad \text{with} \quad 0 < a < 1$$

and combine with (5.65)

$$|\epsilon_2| \leq a|\epsilon_1|$$

So, by induction x_k converges. Also, for $k > 0$, from (5.65)

$$|\epsilon_{k+2}| \leq \frac{l}{m - l(|\epsilon_0| + r)}|\epsilon_{k+1}| \cdot |\epsilon_k| \leq \frac{2al}{m}|\epsilon_k|^2$$

Thus, superlinear convergence is guaranteed. □

5.5.4 Evaluation of the Finite Difference Newton Method Applied to the κ-Estimation Problem

Convergence Evaluation

The finite difference Newton method is applied to the cycle used for figures 5.8–5.11. The constants m and l, defined in theorem 5.5.2, are selected based on figure 5.11.

$$m = 7 \cdot 10^{11} \text{ Pa}^2$$
$$l = 3 \cdot 10^{11} \text{ Pa}^2$$

The limit on the first step, r, and the initial error, ϵ_0, should satisfy

$$r < \frac{m}{2l} = 1.17$$
$$\epsilon_0 \leq \frac{m}{2l} - r = 1.17 - r$$

Here it should also be noted, though, that a tighter restriction on the initial step size (i.e. smaller r), allows a larger uncertainty in the initial estimate, ϵ_0. Also, since $\kappa \in [1.25, 1.45]$, it makes no sense to select $r > 0.2$.

Figure 5.12 shows how the estimated κ changes with iteration number, and figures 5.13 and 5.14 show how the estimation error evolves with each iteration. The cycle used here is the same cycle that was used to produce figures 5.8–5.11. It is observed that the estimation error converges so fast, that for all practical purposes, only two iterations are necessary.

For figure 5.15, the initial guess for κ is intentionally selected to be far from the optimal κ, in order to better show the superlinear convergence which is proved in theorem 5.5.2. The plot shows the error convergence for 10 consecutive cycles.

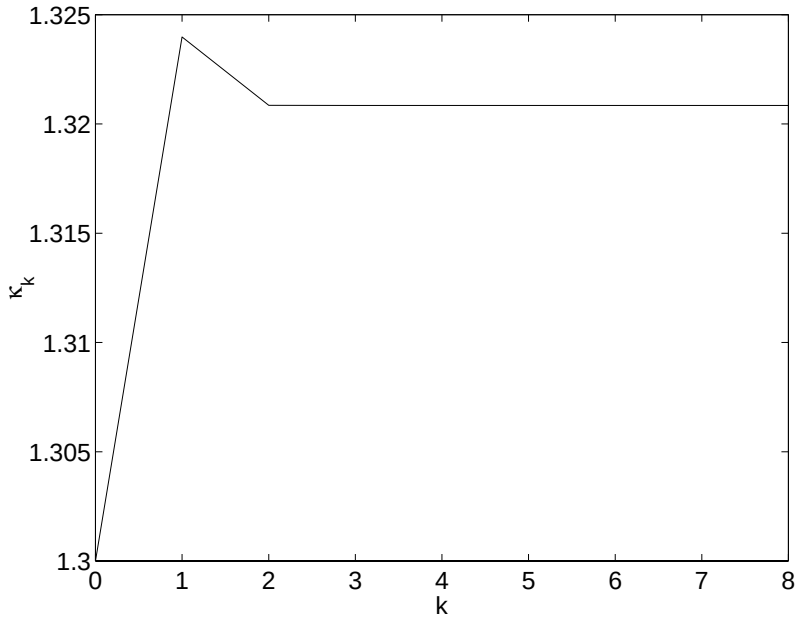

Figure 5.12: Convergence of κ.

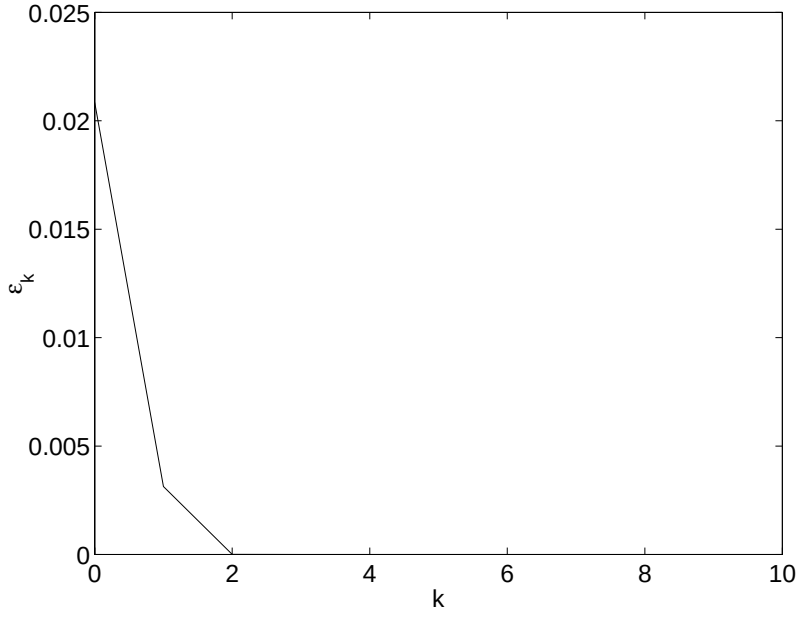

Figure 5.13: Convergence of ϵ_k.

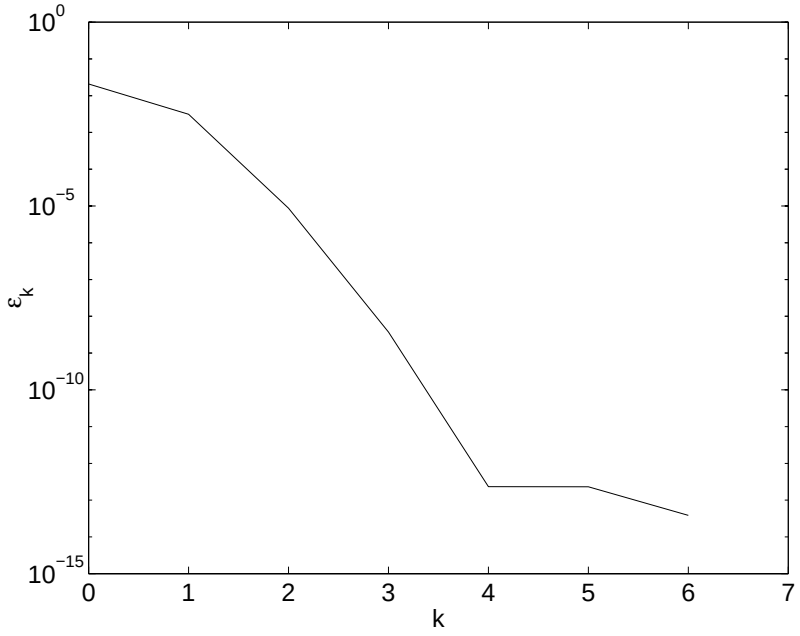

Figure 5.14: Lin-log plot of the convergence of ϵ_k.

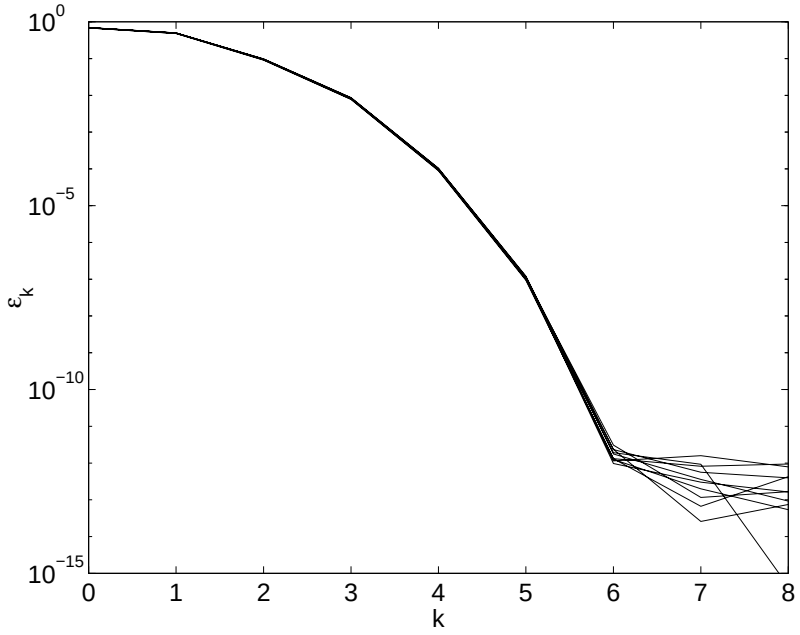

Figure 5.15: Lin-log plot of ϵ_k for 10 consecutive cycles, clearly indicating the superlinear convergence from theorem 5.5.2.

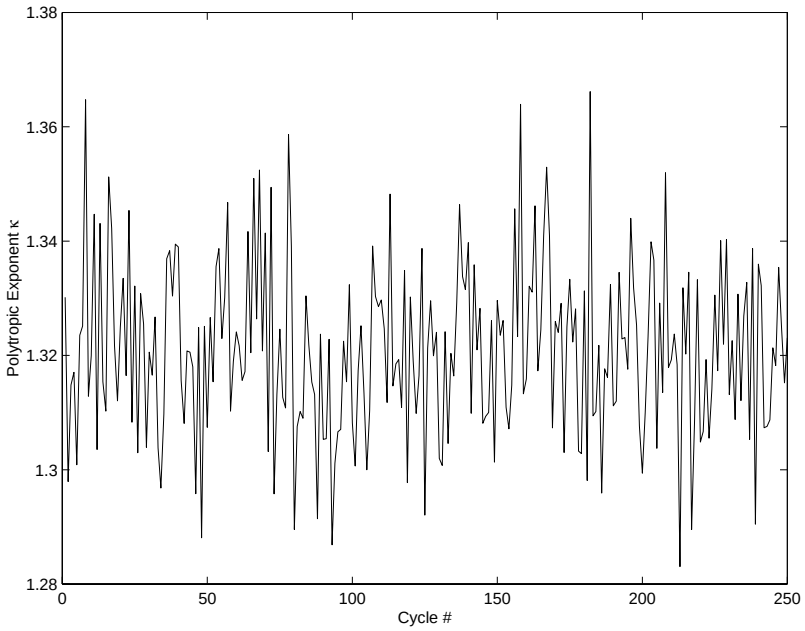

Figure 5.16: Optimal κ for 250 consecutive cycles.

Figures 5.16–5.18 show respectively, the optimal polytropic exponent, the optimal pressure offset, and the cycle-cycle change of the pressure offset. The initial 50 cycles in figure 5.17 indicate that there can indeed be a significant change in the pressure offset over time. The standard deviation of the cycle-cycle sensor-offset change (figure 5.18) is 9 kPa, though, which is approximately the same as the noise level of the pressure signal, see e.g. figure 5.8.

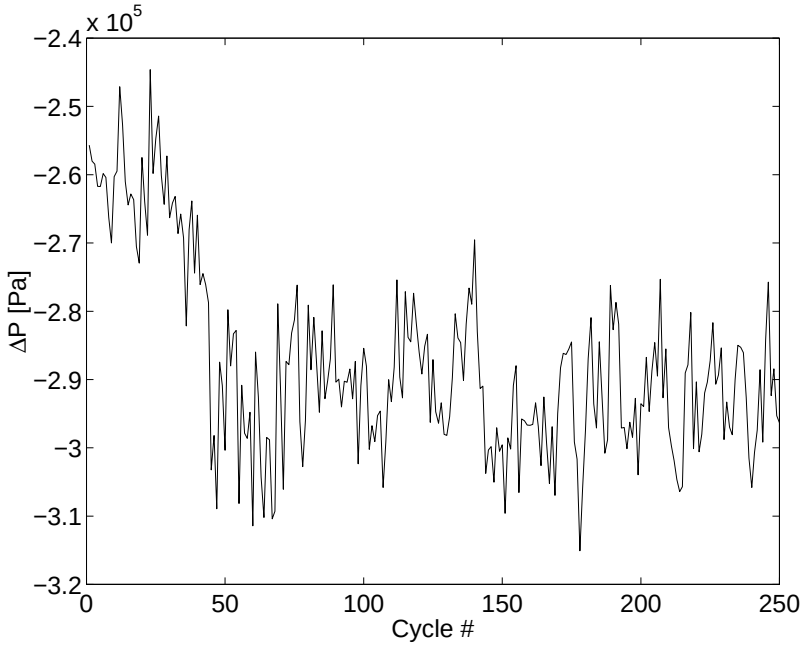

Figure 5.17: Estimated pressure sensor offset for 250 consecutive cycles.

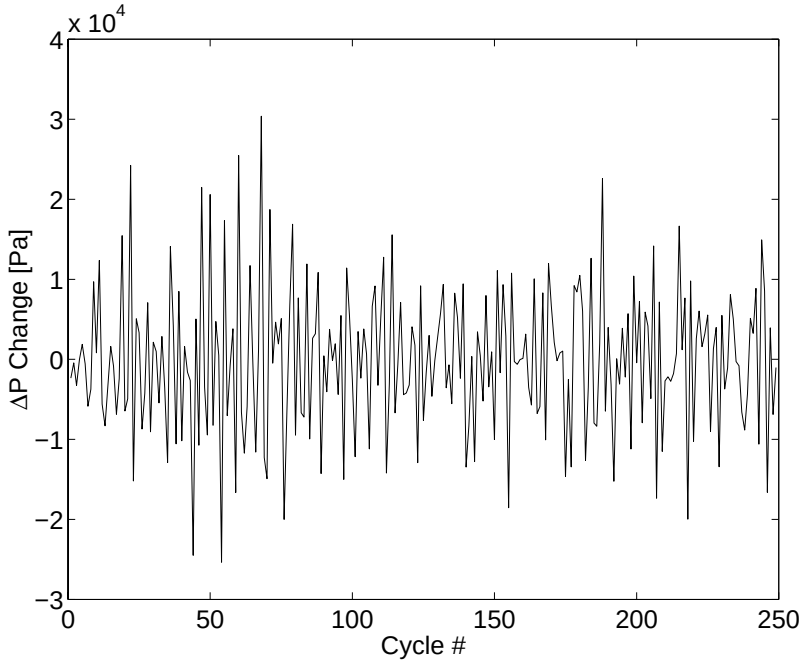

Figure 5.18: Cycle-cycle change in pressure sensor offset for 250 consecutive cycles.

Sensitivity Analysis

Using the definitions of $\hat{\theta}$, P, and E, from equations (5.15), (5.38), and (5.37) respectively, the sensitivity of the least-squares estimates with respect to κ can be calculated.

$$\begin{aligned}\frac{\mathrm{d}\hat{\theta}}{\mathrm{d}\kappa} &= \frac{\mathrm{d}\left(\Phi^T\Phi\right)^{-1}}{\mathrm{d}\kappa}\Phi^T Y + \left(\Phi^T\Phi\right)^{-1}\frac{\mathrm{d}\Phi^T}{\mathrm{d}\kappa}Y \\ &= -\left(\Phi^T\Phi\right)^{-1}\left(\frac{\mathrm{d}\Phi^T}{\mathrm{d}\kappa}\Phi + \Phi^T\frac{\mathrm{d}\Phi}{\mathrm{d}\kappa}\right)\left(\Phi^T\Phi\right)^{-1}\Phi^T Y + \left(\Phi^T\Phi\right)^{-1}\frac{\mathrm{d}\Phi^T}{\mathrm{d}\kappa}Y \\ &= \left(\Phi^T\Phi\right)^{-1}\frac{\mathrm{d}\Phi^T}{\mathrm{d}\kappa}PY - \left(\Phi^T\Phi\right)^{-1}\Phi^T\frac{\mathrm{d}\Phi^T}{\mathrm{d}\kappa}\hat{\theta} \\ &= \left(\Phi^T\Phi\right)^{-1}\left(\frac{\mathrm{d}\Phi^T}{\mathrm{d}\kappa}E - \Phi^T\frac{\mathrm{d}\Phi^T}{\mathrm{d}\kappa}\hat{\theta}\right)\end{aligned} \tag{5.66}$$

Then, the sensitivity functions for ΔP and C are obtained from

$$\frac{\mathrm{d}(\Delta P)}{\mathrm{d}\kappa} = \begin{pmatrix} 1 & 0 \end{pmatrix}\frac{\mathrm{d}\hat{\theta}}{\mathrm{d}\kappa} \tag{5.67}$$

and

$$\frac{\mathrm{d}C}{\mathrm{d}\kappa} = \begin{pmatrix} 0 & 1 \end{pmatrix}\frac{\mathrm{d}\hat{\theta}}{\mathrm{d}\kappa} \tag{5.68}$$

From (5.8), $C = p_0 V_0^{\kappa}$, so the sensitivity of p_0 with respect to κ is given by

$$\frac{\mathrm{d}p_0}{\mathrm{d}\kappa} = \begin{pmatrix} 0 & 1 \end{pmatrix}V_0^{-\kappa}\frac{\mathrm{d}\hat{\theta}}{\mathrm{d}\kappa} \tag{5.69}$$

Figure 5.19 shows the sensitivity of the pressure-offset estimate for 250 consecutive cycles. The sensitivity is roughly 300 kPa for all cycles, and this gives an indication of how accurately κ has to be determined. If e.g. an offset error greater than 10 kPa is unacceptable, then κ has to be determined to within

$$|\mathrm{d}\kappa| = |\mathrm{d}\Delta P| / \left|\frac{\mathrm{d}(\Delta P)}{\mathrm{d}\kappa}\right| \approx 10/300 \approx 0.033$$

Figure 5.20 shows the corresponding sensitivity for the initial pressure, p_0, in the combustion chamber. This sensitivity is approximately -1.2 MPa, and if the desired accuracy for p_0 is 10 kPa also, then κ has to be determined to within

$$|\mathrm{d}\kappa| = |\mathrm{d}p_0| / \left|\frac{\mathrm{d}p_0}{\mathrm{d}\kappa}\right| \approx 10/1200 \approx 0.008$$

The next section shows that this is not possible unless the number of pressure measurements during the compression stroke is increased to 400 or more.

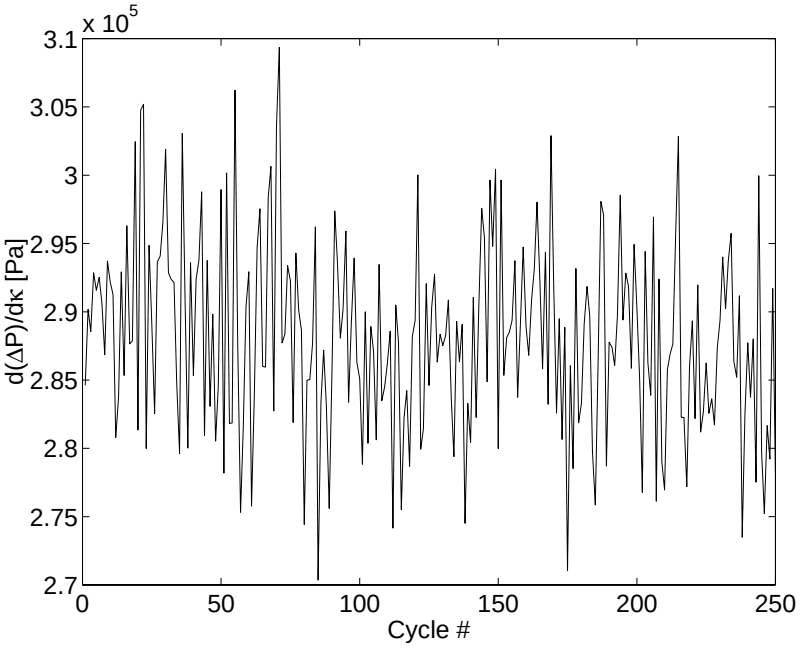

Figure 5.19: Sensitivity, $\mathrm{d}(\Delta P)/\mathrm{d}\kappa$, of the pressure sensor offset estimate, with respect to κ.

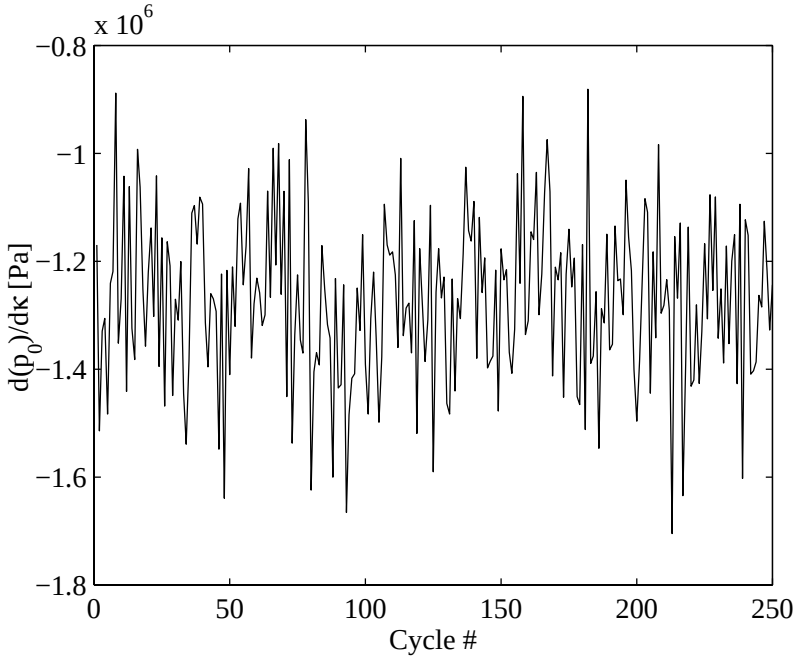

Figure 5.20: Sensitivity, $\mathrm{d}(p_0)/\mathrm{d}\kappa$, of the initial pressure estimate, with respect to κ.

Statistical Properties of the Estimates

The statistical properties of the estimates are investigated using Monte Carlo simulation. It is assumed that each cylinder-pressure measurement $p_m(\alpha)$ is a sum of the pressure obtained from polytropic compression, the sensor offset, Δp, and a zero-mean Gaussian Random variable, $V(\alpha)$, with variance σ^2.

$$p_m(\alpha) = C(V(\alpha))^{-\gamma} + \Delta p + V(\alpha) \tag{5.70}$$

The parameter estimation method is applied to fictitious measurements obtained from this model, and then the sample statistics are investigated. The values used in the simulation are

$$\begin{aligned} \Delta p &= -100 \text{ kPa} \\ p_0 &= 150 \text{ kPa} \\ \kappa &= 1.32 \end{aligned} \tag{5.71}$$

Figures 5.21–5.26 show the results of the simulations in terms of mean values and standard deviations of the estimates of Δp, p_0, and κ. It is noted that the standard deviations of sensor offset and the initial pressure are somewhat higher than for the linear least-squares estimator when the polytropic exponent is estimated as well. This is to be expected, since one more parameter is estimated from the same data. The standard deviations do, however, drop with the number of measurements in a similar manner as for the linear least-squares estimator.

5.6 Conclusions

Both methods presented in this chapter allow estimation of the pressure sensor offset. The first method assumes a constant and known polytropic exponent, whereas the second method estimates this parameter as well.

5.6.1 Linear Least-Squares Estimation

The linear least-squares estimates of pressure sensor offset , Δp, and initial combustion chamber pressure, p_0, described in section 5.4, have excellent statistical properties for the case that the polytropic exponent, κ is known. The standard deviations of the

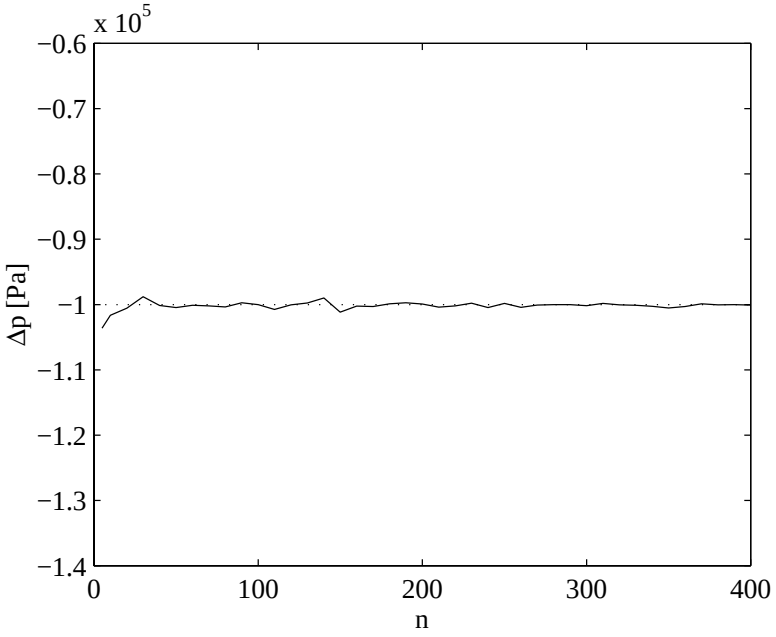

Figure 5.21: 250-cycle mean value of pressure sensor offset as function of the number of measurements. Dotted line represents the nominal value used for the simulation.

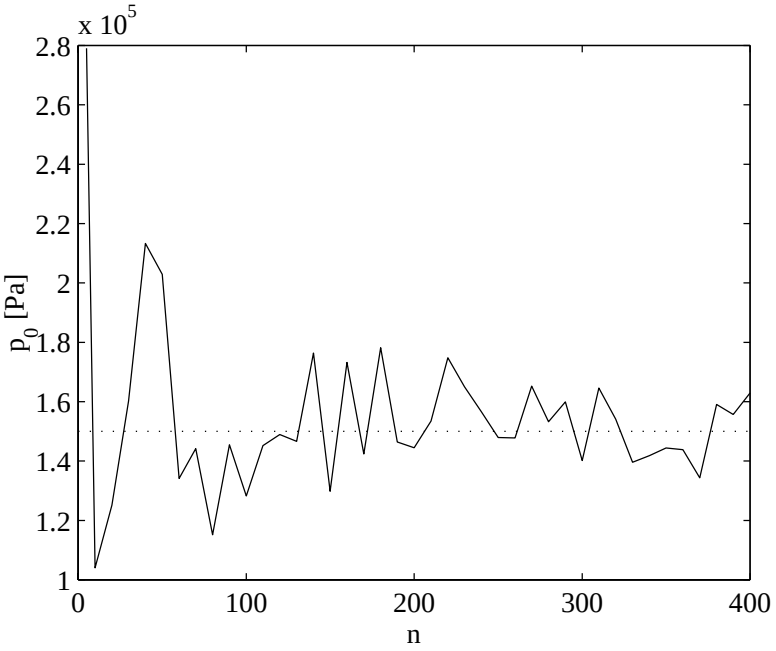

Figure 5.22: 250-cycle mean value of initial pressure estimate as function of the number of measurements. Dotted line represents the nominal value used for the simulation.

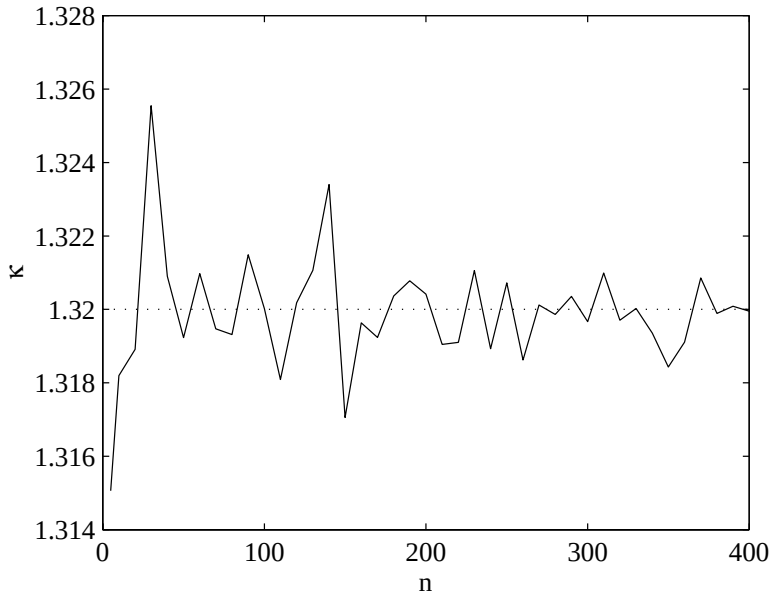

Figure 5.23: 250-cycle mean value of polytropic exponent estimate as function of the number of measurements. Dotted line represents the nominal value used for the simulation.

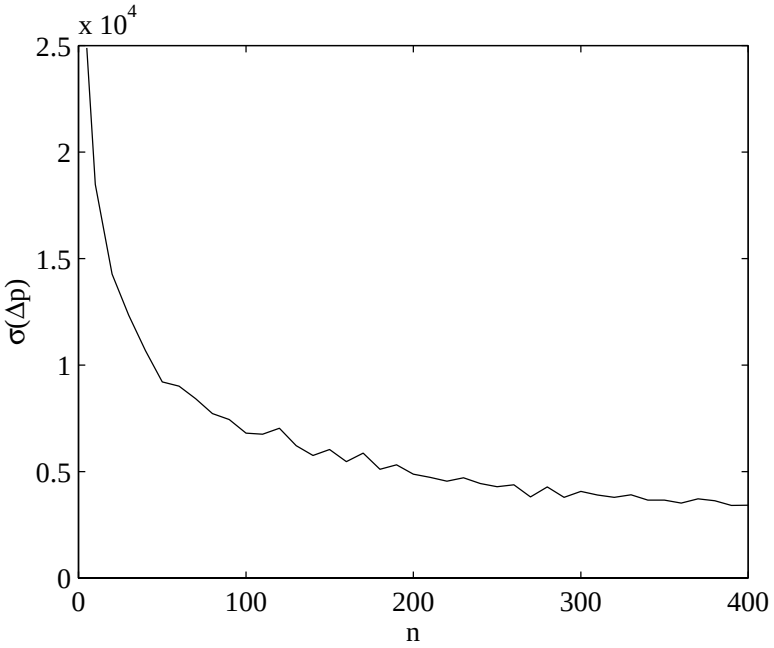

Figure 5.24: Estimated standard deviation of pressure offset estimate as function of the number of measurements. Standard deviation obtained from Monte Carlo simulations.

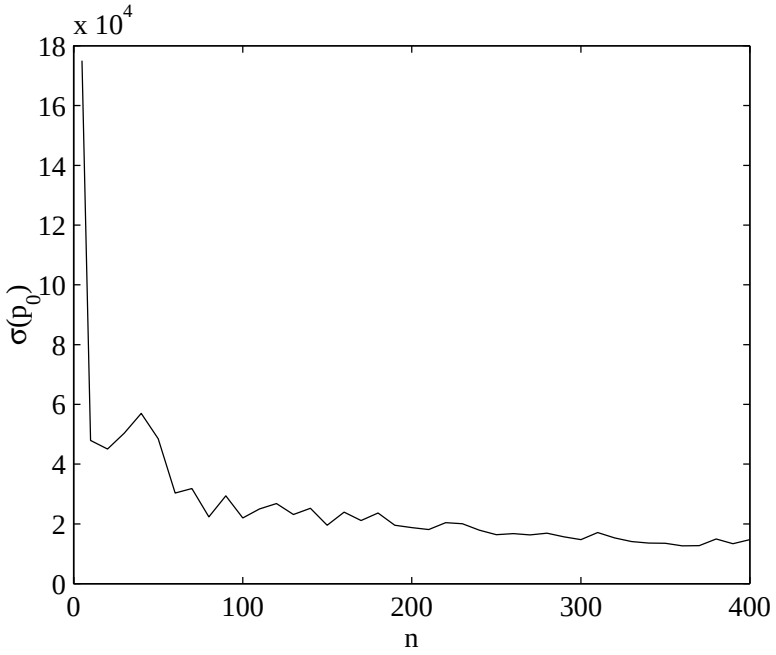

Figure 5.25: Estimated standard deviation of initial pressure estimate as function of the number of measurements. Standard deviation obtained from Monte Carlo simulations.

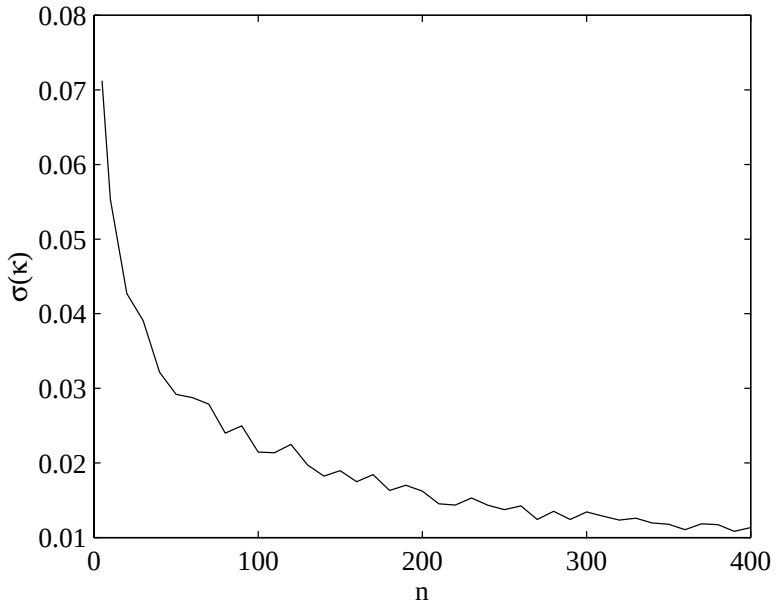

Figure 5.26: Estimated standard deviation of polytropic exponent estimate as function of the number of measurements. Standard deviation obtained from Monte Carlo simulations.

estimates roughly drop as $1/\sqrt{n}$ with the number of samples, n. This means that with as few as 50 samples, the standard deviations of the estimates are reduced to one fifth of the standard deviation obtained with the present methods based on only two samples.

The experimental residuals from the least-squares fits show a standard deviation of the same magnitude as the noise in the cylinder pressure measurements. Furthermore, there is no visible trend in the residuals, which implies that the polytropic compression model accurately describes the real compression process.

Comparison between cylinder pressure late in the intake stroke, corrected for sensor offset, and intake manifold pressure shows good agreement. The engine used for the experiments runs at low speeds ranging from 1000–2000 RPM, which means that the pressure drop between intake manifold and combustion chamber should be modest. This means that the difference between the intake manifold pressure and the cylinder pressure around the bottom dead center should be small, and the intake manifold pressure can be used to check the validity of the estimate.

5.6.2 Nonlinear Least-Squares Estimation

For the case that the polytropic exponent is unknown or varies from cycle to cycle, the nonlinear least-squares method developed in section 5.5 can be applied. Each iteration of the finite difference Newton method to find the least-squares estimate of κ involves applying the linear least-squares method once, and computing the derivative of the loss function once. The cost of computing the actual Newton step is negligible. The computational cost for computing the derivative is the same as for applying the linear least-squares method. Both problems involve solving a linear system of equations with the same left-hand side though, so information from one can be used for the other. Thus, the cost for solving both these problems is essentially the same as the cost of just applying the linear least-squares method once. Furthermore, the Newton method converges in just a few steps, so the total cost is only a few times the cost of applying the linear least-squares method.

The standard deviations of the estimates are somewhat higher for the nonlinear least-squares estimates. This is to be expected since one more parameter is estimated. If κ is known to be constant or if it varies little from cycle to cycle, the estimate for κ can be low-pass filtered, and the filtered estimate can be used for linear least-squares estimation of the other two parameters. With sufficient filtering this should take the standard deviations

down to approximately the levels of the linear least squares estimates for the case that κ is known.

Generality of the Method

This method is applicable to any nonlinear least-squares problem for which the model can be represented on the form

$$y = \varphi(\kappa)\theta \tag{5.72}$$

where y is the output, θ is a vector of unknown parameters, and φ is a vector of regressors which depend nonlinearly on the unknown parameter κ. The only requirement on φ is that it is $\mathbb{C}^2$ with respect to κ, and that an analytic expression for $\mathrm{d}\varphi/\mathrm{d}\kappa$ is available.

The first step of the method is to solve the linear least-squares problem which results if κ is treated as a known parameter.

$$\hat{\theta}(\kappa) = \left(\Phi^T\Phi\right)^{-1}\Phi^T Y \tag{5.73}$$

where Y and Φ represent a collection of observations as in (5.11) and (5.12).

Next, a loss function, J, is defined as the squared 2-norm of the residuals, D.

$$D(\kappa) = Y - \Phi\hat{\theta}(\kappa), \qquad J(\kappa) = D(\kappa)^T D(\kappa) \tag{5.74}$$

The derivative of the loss function with respect to κ is given by (5.47)

$$\frac{\mathrm{d}J}{\mathrm{d}\kappa} = -2D(\kappa)^T\frac{\mathrm{d}\Phi}{\mathrm{d}\kappa}\hat{\theta}(\kappa) \tag{5.75}$$

The final step is to apply the finite difference Newton method of theorem 5.5.2 to minimize the loss function J.

Chapter 6

Air/Fuel Ratio Estimation using Total Heat-Release Duration

6.1 Introduction

6.1.1 Method

This chapter develops a method to estimate the Air/Fuel Ratio (AFR) in a Spark-Ignition (SI) engine from cylinder pressure measurements. The method is developed from a well-established empirical model for the dependence of laminar flame speed on temperature, pressure, and AFR, and relates this model to the heat-release rate during the rapid burn phase, which is obtained from the cylinder-pressure-based net heat release profile.

Since the actual flame speed in an SI engine depends on the turbulence intensity, a turbulence model also has to be included. This model includes a simple turbulence model implicitly, by assuming that the turbulence intensity is a function of engine speed [19]

6.1.2 Results

An AFR estimator which is able to estimate cylinder AFR from cylinder pressure measurements over a wide range of operating points is developed. The variance of an individual cycle estimate is very high due to e.g. the random nature of the amount of residual gas in the cylinder, as well as the turbulent flow field which will cause the flame development to be different from cycle to cycle. Cycle-averaged AFR estimates show an RMS error of only 4.1 % though. The identification and validation experiments were performed at the

Berkeley facility (see chapter 3.

6.2 Review of the Concepts of Flame and Flame Speed

The following section is a review of the concepts of flame and flame speed, and is included for completeness. The presentation is largely based on [19].

6.2.1 Definition of Flame

A flame is a combustion reaction which propagates subsonically through space. For motion of the reaction zone to be well-defined, it is assumed that the thickness of the reaction zone is small compared to the dimensions of the space it is confined to. Propagation of the reaction zone refers to its motion relative to the unburned gas ahead of it, and thus a propagating flame can very well be stationary with respect to the observer.

Two different classes of flames can be distinguished based on where the mixing of fuel and oxidizer (air) takes place. If fuel and oxidizer are uniformly mixed when entering the reaction zone, a *premixed* flame results. A *diffusion* flame results if fuel and oxidizer have to mix as the reaction is taking place.

Similarly, flames can be characterized based on the gas flow characteristics in the reaction zone. Flames can be either *laminar* (stream lined flow), or *turbulent* (vortex motion).

Flames can be classified as *unsteady* or *steady* depending on whether their overall motion or structure change with time or not.

Finally, the initial phase of the fuel, when it enters the reaction zone can be used for classification of the flame. It can be either *solid, liquid* or *gaseous*.

The flame in an SI engine is premixed, turbulent, and unsteady, and the fuel is gaseous when it enters the reaction zone.

6.2.2 Laminar Flame Speed

The laminar flame speed is defined as the velocity, relative and normal to the flame front, with which the unburned gas moves into the front and is converted into products under laminar flow conditions (see figure 6.1). This definition originates from experiments with burners, where the flame is stationary, the unburned gas moves into the flame, and the

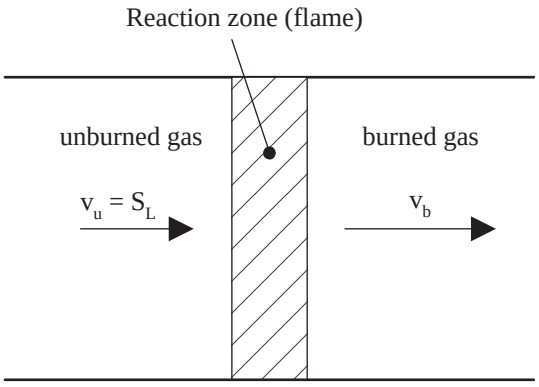

Figure 6.1: Illustration of a stationary laminar flame with unburned gas entering the reaction zone at the laminar flame speed, $S_L = v_u$, and leaving the reaction zone at a velocity, $v_b > v_u$.

burned gas moves out of and away from the flame. The density of the burned gas is, in general, lower than the density of the unburned gas, and consequently the burned gas will have a higher velocity than the unburned gas.

A situation more relevant to engines, is that the unburned gas is stationary, and the reaction zone propagates through the gas. In this case the laminar flame speed is actually the speed at which the flame front propagates (see figure 6.2). The laminar flame speed under engine pressure and temperature is of the order 0.5 m/s. In reality, the unburned gas in an engine actually moves away from the flame front, due to the expansion of the burned gas and compression of the unburned gas.

One might be tempted to claim that the laminar flame speed is of limited interest for internal combustion engines, since the flow conditions in any practical engine are highly turbulent. It turns out however, that one important way of modeling the turbulent flame development (see section 6.2.3) which actually takes place in an internal combustion engine, includes the laminar flame concept as a submodel.

6.2.3 Turbulent Flame Speed

The presence of turbulence tends to distort and wrinkle the flame front, and in the case of intense turbulence, transforms the flame into a thick convoluted brush with unburned mixture trapped in it.

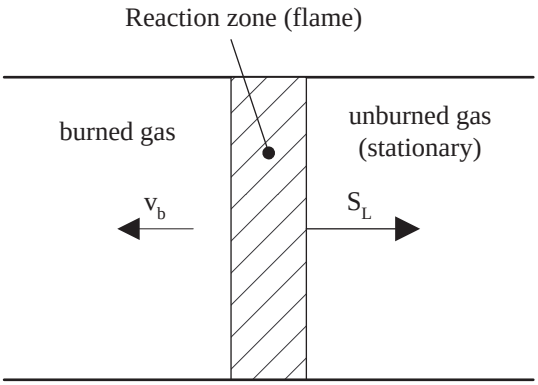

Figure 6.2: Illustration of a propagating laminar flame. The flame front moves at the laminar flame speed, S_L, into the stationary unburned gas. Due to the expansion, the burned gas is pushed backwards out of the reaction zone at a velocity, v_b.

The turbulent gas motion also aids in propagating the flame, and since the local gas velocities due to turbulence can be significantly higher than the laminar flame speed, turbulence can drastically increase the actual speed with which the reaction zone propagates. This speed is called the turbulent flame speed. In [17] Groff and Matekunas show that the turbulent flame speed is proportional to the laminar flame speed, and a factor which increases monotonically with the turbulence intensity.

6.3 Flame Speed Models

6.3.1 A Laminar Flame Speed Model

The laminar flame speed of a premixed gasoline/air flame increases monotonically with temperature, decreases monotonically with pressure, and peaks for equivalence ratios slightly rich of stoichiometric. This behavior can be modeled empirically by

$$S_L = S_{L,0} \left(\frac{T_u}{T_0} \right)^{\mu} \left(\frac{p}{p_0} \right)^{\beta} \tag{6.1}$$

where $S_{L,0}$ is the laminar flame speed at $T_0 = 298$ K and $p_0 = 1$ atm. The parameters α and β depend slightly on the equivalence ratio.

The laminar flame speed at normal pressure and temperature, $S_{L,0}$ can be modeled

by

$$S_{L,0} = B_m + B_\phi(\phi - \phi_m)^2 \tag{6.2}$$

Here, B_m represents the maximum flame speed attained at equivalence ratio ϕ_m. The following values were experimentally identified by Metgalchi and Keck [35] for the laminar flame speed of a gasoline/air flame

$$\phi_m = 1.21$$
$$B_m = 0.305 \text{ m/s}$$
$$B_\phi = -0.549 \text{ m/s}$$

The range of equivalence ratios relevant for an SI engine intended for stoichiometric operation is roughly $[0.9, 1.1]$, which means that the laminar flame speed varies approximately $\pm 8\%$ relative to the stoichiometric value.

6.3.2 Modeling the Turbulent Flame Speed

It is discussed in [19] that the rapid burn angle $\Delta\alpha_b$ increases only slightly with engine speed. This implies that the turbulence intensity increases with engine speed, which causes an increase in the flame speed. Measurements in Hires [21] indicate that the rapid burn angle, with inlet pressure and equivalence ratio constant, follows approximately a power law with respect to engine speed

$$\Delta\alpha_b \sim N^{0.37} \tag{6.3}$$

Since the way the turbulent flow characteristics change with engine speed depends on the engine geometry, the exponent in the previous equation is considered as an unknown, η, which has to be determined from experiments. Thus

$$\Delta\alpha_b = kN^\eta \tag{6.4}$$

The time it takes for the flame to propagate from the spark gap to the farthest end of the combustion chamber can be expressed as

$$\Delta t_b = \frac{sB}{u_f} \tag{6.5}$$

where B is the cylinder bore, s is a factor which depends on the location of the spark gap, and u_f is the flame speed. A simple relationship based on the engine speed relates Δt_b and $\Delta\alpha_b$

$$\Delta\alpha_b = \frac{\mathrm{d}\alpha}{\mathrm{d}t}\Delta t_b = \frac{2\pi N}{60}\Delta t_b \tag{6.6}$$

Thus, the flame speed can be expressed in terms of the crank-angle burn duration

$$u_f = \frac{2\pi sBN}{60\Delta\alpha_b} \tag{6.7}$$

Combining (6.4) and (6.7) yields

$$u_f = u_0\left(\frac{N}{N_0}\right)^{1-\eta} \tag{6.8}$$

where

$$u_0 = \frac{2\pi sBN_0^{1-\eta}}{60k} \tag{6.9}$$

and N_0 is some arbitrary engine speed. It should be noted here that u_0 will depend on equivalence ratio, pressure, and temperature in the same way as the laminar flame speed according to (6.2). Now, assuming that ϕ is close enough to ϕ_m,

$$u_0 = u_{00}\left(\frac{T_u}{T_0}\right)^{\mu}\left(\frac{p}{p_0}\right)^{\beta} \tag{6.10}$$

6.4 Incorporating the Cylinder-Pressure-Based Heat Release into the Flame Speed Models

6.4.1 Relating Burn Rate to Flame Speed

Spherical Flame Front

Assuming that the flame grows spherically from the spark gap, the enflamed volume can be expressed as

$$V_f = \frac{4\pi r_f^3}{3} \tag{6.11}$$

where the flame radius can be expressed as a function of time using the flame speed, u_f

$$r_f = u_f t \tag{6.12}$$

The rate at which the enflamed volume grows can be expressed as

$$\frac{\mathrm{d}V_f}{\mathrm{d}t} = \frac{4\pi u_f^3}{3} \cdot 3t^2 = 4\pi u_f^3 t^2 \tag{6.13}$$

The rate at which fuel is consumed can now be expressed using the expression for the derivative of the enflamed volume (6.13)

$$\frac{\mathrm{d}m_f}{\mathrm{d}t} = \frac{m_f}{V}\frac{\mathrm{d}V_f}{\mathrm{d}t} = \frac{m_f}{m_a}\frac{m_a}{V}\frac{\mathrm{d}V_f}{\mathrm{d}t} \approx \frac{1}{\mathrm{AFR}}\frac{p}{RT} \cdot 4\pi u_f^3 t^2 \tag{6.14}$$

The approximation is in the application of the ideal gas law. The fuel mass has been neglected in assuming

$$pV = m_a RT \tag{6.15}$$

Since the AFR in a gasoline engine is nominally 14.7 this is a reasonable approximation.

The burn rate relative to crank angle can now be determined using the relationship

$$\frac{\mathrm{d}\alpha}{\mathrm{d}t} = \omega_e = 2\pi\frac{N}{60} \tag{6.16}$$

where ω_e is the engine angular velocity, and N is the engine speed in RPM. Thus

$$\frac{\mathrm{d}m_f}{\mathrm{d}\alpha} = \left(\frac{\mathrm{d}m_f}{\mathrm{d}t}\right) / \left(\frac{\mathrm{d}\alpha}{\mathrm{d}t}\right) \tag{6.17}$$

Combining (6.14) and (6.17) yields an expression for the burn rate relative to crank angle

$$\frac{\mathrm{d}m_f}{\mathrm{d}\alpha} = \frac{1}{\mathrm{AFR}}\frac{p}{RT} \cdot \frac{120 u_f^3 t^2}{N} \tag{6.18}$$

Experimental observation of heat-release profiles support the quadratic dependence on time for the early stages of combustion. During the rapid burn phase of combustion, the burn rate is essentially constant though. An explanation for this is that the combustion chamber is finite, and the the spherical flame front gets cut off by the combustion chamber walls. Figure 6.3 shows a cross section of a cylindrical combustion chamber with a flame front propagating from a centrally located spark plug, and it can be seen that the arc length of the circular flame front (corresponding roughly to the area of the flame front in three dimensions) levels out early in the combustion process. Then the area of the flame front stays roughly constant until towards the end of combustion.

A more realistic model then, is that the area of the flame front is constant during the rapid-burn phase, which means that the enflamed volume grows at a constant rate

$$\frac{\mathrm{d}V_f}{\mathrm{d}t} = A_f u_f \tag{6.19}$$

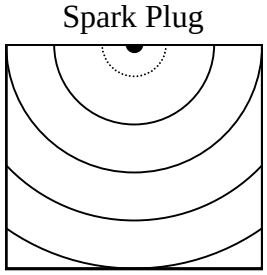

Figure 6.3: Two-dimensional illustration of flame propagation from the spark plug. The circle segments represent the flame front as it propagates radially outward from the spark gap. All flame fronts marked with solid lines are essentially of equal length.

where A_f is the constant flame front area. Substituting (6.19) for the volume derivative in (6.14) yields

$$\frac{\mathrm{d}m_f}{\mathrm{d}t} \approx \frac{p}{\mathrm{AFR} \cdot RT} \cdot A_f u_f \tag{6.20}$$

Combine (6.20) and (6.16) to get an expression for the burn rate with respect to crank angle.

$$\frac{\mathrm{d}m_f}{\mathrm{d}\alpha} = \frac{60 A_f u_f p}{2\pi N \cdot \mathrm{AFR} \cdot RT} \tag{6.21}$$

Using (6.8) for the flame speed, (6.21) can be rewritten as

$$\frac{\mathrm{d}m_f}{\mathrm{d}\alpha} = \frac{60 A_f u_0 p N^{-\eta}}{2\pi N_0^{1-\eta} \cdot \mathrm{AFR} \cdot RT} \tag{6.22}$$

Using (6.10) and consolidating the multiplicative constant, an expression for the burn rate as a function of pressure, temperature, and engine speed is obtained

$$\frac{\mathrm{d}m_f}{\mathrm{d}\alpha} = b p^{1+\mu} T^{\beta-1} N^{-\eta} \cdot \mathrm{AFR}^{-1} \tag{6.23}$$

for some constant b.

6.4.2 Relating Burn Rate to Average Heat Release Rate

During the rapid burn phase of the cycle, the heat-release rate is essentially constant in the crank-angle domain. Thus, during the bulk of the combustion event, the heat-release rate can approximately be expressed as

$$\frac{\mathrm{d}Q_{ch}}{\mathrm{d}\alpha} \approx \frac{Q_{tot}}{\Delta\alpha_b} \tag{6.24}$$

The chemical energy released when combusting a unit mass of fuel with air is the lower heating value, Q_{LHV}. Thus, the rate of fuel conversion can be expressed as

$$\frac{\Delta m_f}{\Delta \alpha} = \frac{1}{Q_{LHV}} \frac{Q_{tot}}{\Delta \alpha_b} \tag{6.25}$$

Combining the two expressions for the burn rate, (6.23) and (6.25), provides an equation from which the AFR can be determined. The pressure and temperature at the start of combustion are determined by a compression polytrope from the inlet pressure and temperature. Thus, the inlet pressure and temperature, p_0, T_0, can be used

$$b p_0^{1+\mu} T_0^{\beta-1} N^{-\eta} \cdot \mathrm{AFR}^{-1} = \frac{1}{Q_{LHV}} \frac{Q_{tot}}{\Delta \alpha_b} \tag{6.26}$$

Isolating AFR yields

$$AFR = b Q_{LHV} \frac{\Delta \alpha_b}{Q_{tot}} p_0^{1+\mu} T_0^{\beta-1} N^{-\eta} \tag{6.27}$$

So, with $c = bQ_{LHV}$

$$AFR = c \frac{\Delta \alpha_b}{Q_{tot}} p_0^{1+\mu} T_0^{\beta-1} N^{-\eta} \tag{6.28}$$

where c, μ, β, and η are unknown constants, which have to be determined from experiments.

6.5 Identification of Model Parameters

6.5.1 Identification Method

The experimental setup used for this work does not allow control of the intake air temperature, and thus only the dependence of AFR on burn rate, pressure, and engine speed are investigated. In the identification experiments, the coolant temperature is held constant, in order to prevent any influence from this temperature.

In order to identify the unknown parameters of (6.28), it is rewritten by taking logarithms

$$\ln\left(\frac{\mathrm{AFR}}{\Delta \alpha_b / Q_{tot}}\right) = \ln(c T_0^{\beta-1}) + (1+\mu)\ln p_0 + (-\eta)\ln N \tag{6.29}$$

Define the parameter vector,

$$\theta = \begin{pmatrix} \ln(c T_0^{\beta-1}) \\ 1+\mu \\ -\eta \end{pmatrix} \tag{6.30}$$

the vector of regressors

$$\varphi = \begin{pmatrix} 1 & \ln p_0 & \ln N \end{pmatrix} \tag{6.31}$$

and the output

$$y = \ln\left(\frac{\mathrm{AFR}}{\Delta\alpha_b/Q_{tot}}\right) \tag{6.32}$$

Now, it is assumed that measurements are available from n cycles. The outputs from the measurements, defined by (6.32), are collected into an output vector, Y, and the regressor vectors, defined by (6.31), are collected into a regression matrix, Φ.

$$Y = \begin{pmatrix} y_1 \\ \vdots \\ yn \end{pmatrix}, \qquad \Phi = \begin{pmatrix} \varphi_1 \\ \vdots \\ \varphi_n \end{pmatrix} \tag{6.33}$$

and solve for the least-squares estimate, $\hat{\theta}$, according to the method described in section 5.4.2

$$\hat{\theta} = \left(\Phi^T\Phi\right)^{-1}\Phi^T Y \tag{6.34}$$

The parameter estimate obtained from the linear least-squares solution above minimizes sum of squares of residuals of the form

$$r_{\ln} = \ln(\hat{\mathrm{AFR}}) - \ln(\mathrm{AFR}) = \ln\left(\frac{\hat{\mathrm{AFR}}}{\mathrm{AFR}}\right) \tag{6.35}$$

This is not the same however, as minimizing the sum of squares of the estimation error

$$r = \hat{\mathrm{AFR}} - \mathrm{AFR} \tag{6.36}$$

Since a ratio is being estimated though (the ratio of air mass to fuel mass in the cylinder), it makes more sense to minimize (6.35).

6.5.2 Identification Experiments

When applying experimental data to the estimation method described above, it has to be decided which pressure to use in the regression vector. Here, p_0 defined by (5.8) is selected, since this pressure, because of the polytropic compression relation, scales with the pressure at the onset of combustion.

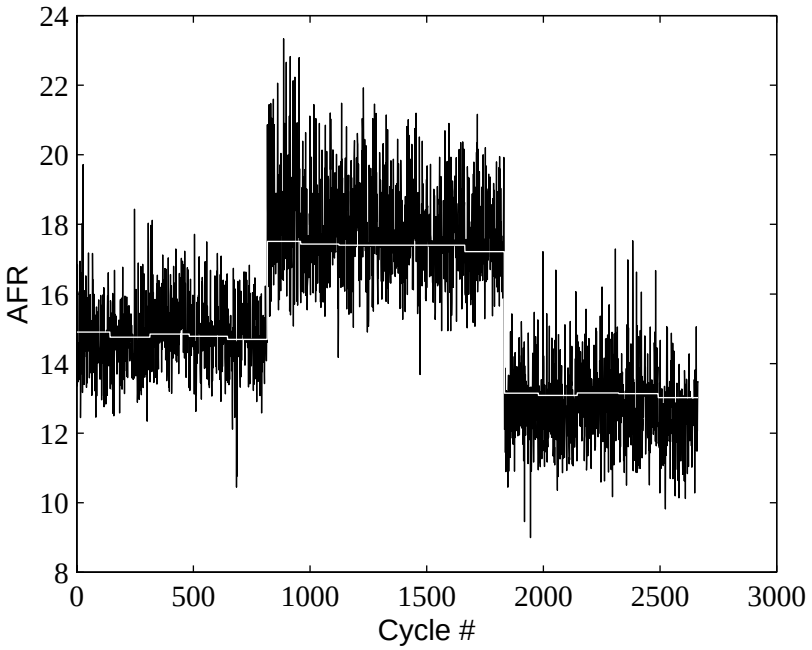

Figure 6.4: Estimated AFR (black line) and measured AFR (white line).

The experiments were carried out as steady state experiments at different loads, engine speeds, and AFR. Each steady-state experiment lasts for approximately 10 s. For each of these experiments, the mean exhaust AFR is selected as the "true" AFR for all the cycles of that experiment. The reason for this is that the true AFR for the individual cylinder cycles cannot be singled out when using exhaust AFR measurements.

Figure 6.4 shows the result of the least-squares fit applied to the identification data. The variance of the estimate is quite large, and requires some kind of filtering in order to be of practical use. Figure 6.5 shows the residuals for the same data.

6.6 Model Validation

The presented model for AFR estimation was validated by conducting similar experiments as the ones used for the identification. The result of these measurements in terms of estimated AFR versus measured exhaust AFR are shown in figure 6.6.

The plot shows that except for at very lean operating points (AFR $\geq$ 18, the estimator performs well. For the leanest operating points, the estimator tends to overestimate

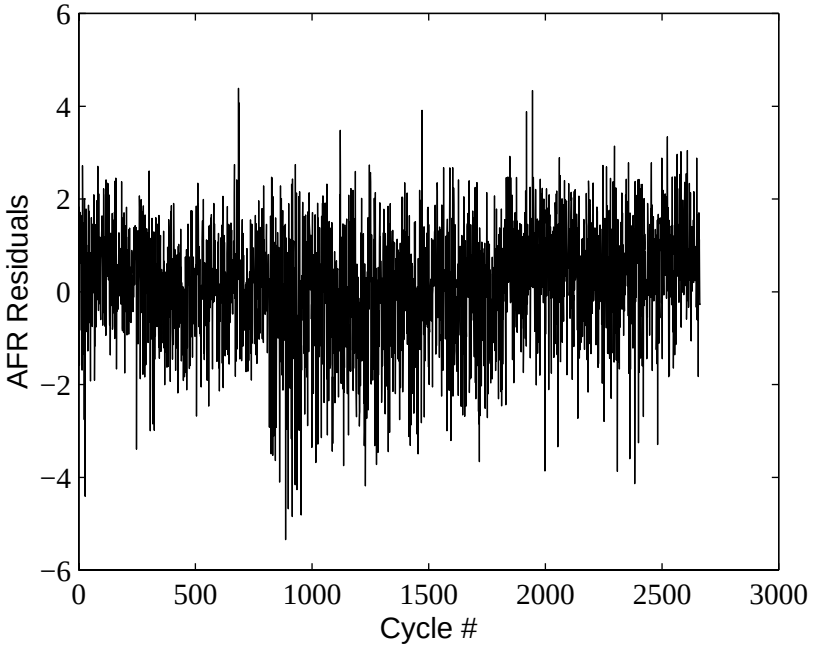

Figure 6.5: Residuals of least-squares AFR fit

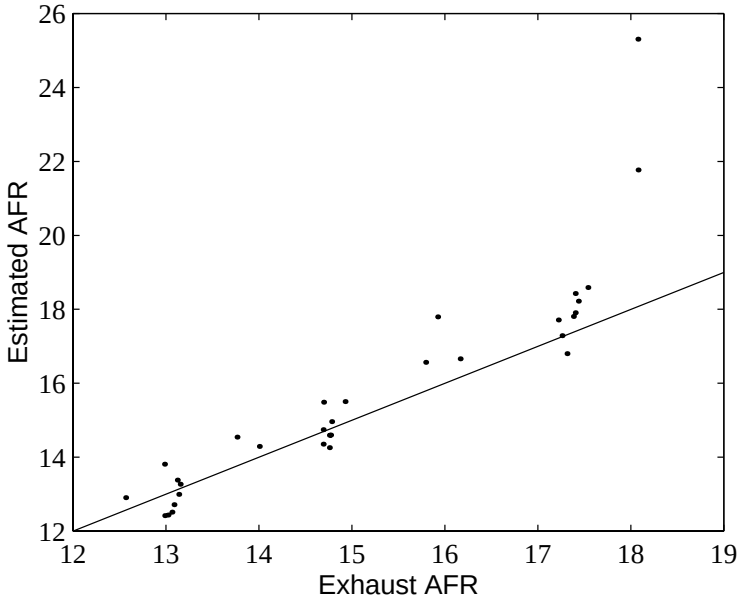

Figure 6.6: Cycle-averaged (10 s) estimated AFR plotted versus measured exhaust AFR. Experiments conducted at a range of engine speeds, loads, and Air/Fuel Ratios. The RMS error in the estimate is 4 % when excluding the two estimates at the lean limit.

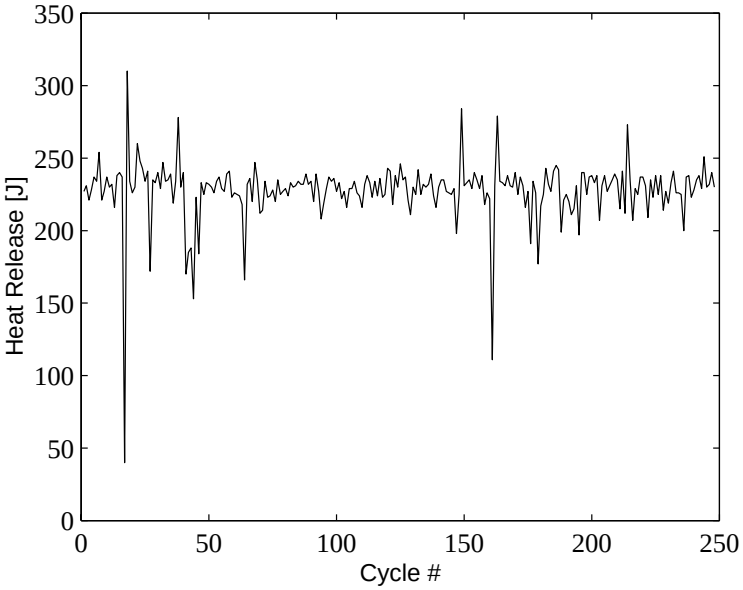

Figure 6.7: Heat release for 248 consecutive cycles at AFR = 18.1. The plot clearly indicating incomplete combustion for several cycles. The estimated AFR for these cycles is 25.3

the AFR. This is caused by the fact that the engine is operating near its lean limit. At the lean limit, combustion is either too slow to finish before the exhaust valve opens, or the gas temperature is so low that the flame extinguishes before it reaches the far cylinder wall. For both these cases, the result is that not all of the fuel is combusted, and thus the heat release is significantly lower. Since the estimated AFR is inversely proportional to the heat release, this will result in an overestimated AFR.

Figure 6.7 shows the heat release for 248 consecutive cycles with an air/fuel ratio of 18.1, and it is easily seen that combustion is incomplete for a significant number of cycles. It is interesting to note that cycles with very high values of heat release follow immediately after cycles with incomplete combustion. This indicates that the residual gas (the gas which stays in the cylinder from one cycle to the next) contains a significant amount of unburned fuel. This is further evidence that the combustion of the preceding cycle was in fact incomplete. For reference, figure 6.8 shows the heat release for 171 consecutive cycles with an air/fuel ratio of 14.76. For these cycles the heat release is almost constant from cycle to cycle.

Figure 6.9 shows a ten-cycle moving average of the AFR estimate for a steady-

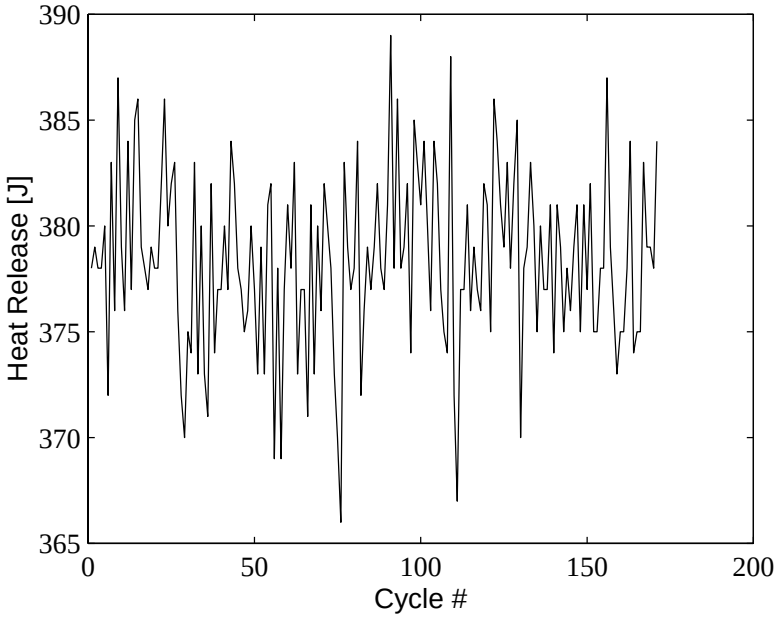

Figure 6.8: Heat release for 171 consecutive cycles at AFR = 14.76. Compared to figure 6.7 the heat release is almost constant from cycle to cycle, indicating that combustion is nearly complete.

state experiment at stoichiometric operation. The figure shows that most of the variance in the raw estimate is removed by taking the average over ten consecutive cycles.

6.7 Conclusion

The proposed model for estimating the AFR from cylinder pressure data performs well when cycle-averaging is performed. The RMS error of the AFR estimates from the validation data is 4.1 %, which is somewhat better than with the molar weight ratio method proposed in [39].

A drawback with the proposed estimator is that the variance of the estimates is large. The observed cycle-cycle variability is of such a magnitude that it cannot reflect actual variations in the cylinder AFR. The extremely simple turbulence model, used for the turbulent flame speed expression (6.8), which assumes that the turbulence intensity is completely determined by the engine speed, is a likely source of error.

An additional source of error is the assumption of a constant time derivative of

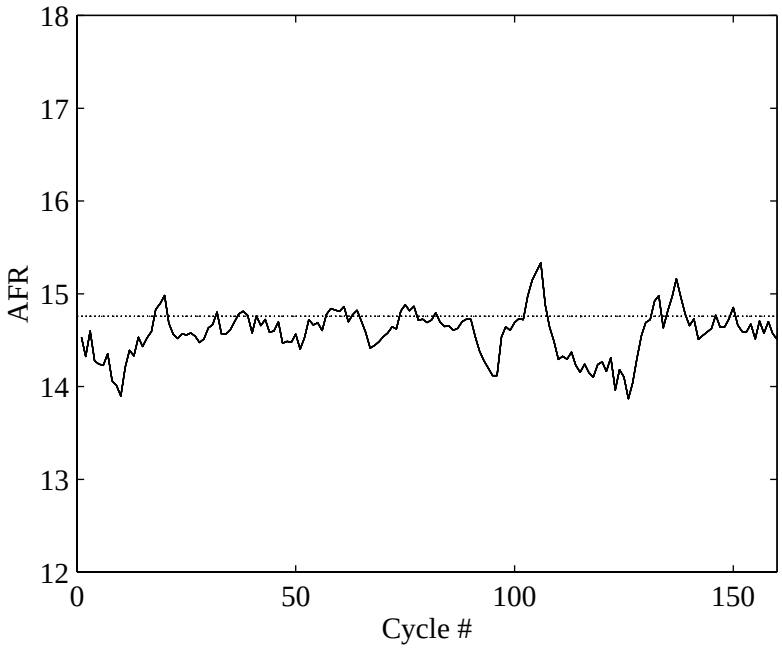

Figure 6.9: Ten cycle moving average of AFR estimate. Steady-state operation with stoichiometric AFR.

the enflamed volume (6.19). As indicated in section 6.4.1, the derivative of the enflamed volume depends on where in the combustion chamber the flame center is located. Even though the flame is initiated in the spark-plug gap, the center of the flame may move away due to the in-cylinder flow field. This will result in a different expression for the enflamed volume derivative. Thus, since the flow field differs from cycle to cycle, the burn rate will also differ from cycle to cycle, and the burn rate is the basis for the AFR estimate.

The temperature dependence in the estimation model has not been verified in this work. Investigating this dependence would require a setup where the temperature of the intake air as well as the temperature of the coolant can be controlled.

The large variation from cycle to cycle of the cylinder-AFR estimate can be reduced by applying a low-pass filter or a moving average filter to the raw estimate. This will however lower the bandwidth of the estimator.

6.8 Discussion about Applications

6.8.1 Cold Start Control

About 80 % of the unburned hydrocarbons emitted from automotive engines today are produced during the cold-start phase. The cold-start phase is defined as the first 120 minutes of operation, before the catalytic converter has reached maximum conversion efficency. During cold start, additional fuel has to be supplied, in order to compensate for poor fuel vaporization caused by condensation of fuel on cold surfaces.

In present engine control systems, fuel is supplied according to an open-loop strategy during cold start, since the exhaust is too cold for the exhaust oxygen sensor to produce measurements. The open-loop strategies use a fuel correction factor which depends on the engine coolant temperature, in order to supply more fuel when the engine is cold. This means that deviations in the fuel delivery rates from fuel injectors compared to commanded fuel delivery rates will be directly reflected in errors in the cylinder AFR. In the case of too much fuel delivery, this means increased fuel consumption and hydrocarbon emissions. In the case of too little fuel delivery on the other hand, rough engine operation and/or misfiring would result, also causing increased hydrocarbon emissions.

The proposed estimator can be used during coldstart while the exhaust gas is still too cold for the exhaust gas oxygen sensor to provide feedback. This would allow for closed-loop AFR control even during cold start. The high estimation variance is less of a problem during cold-start, since the cold-start phase consists mainly of idling, which implies nearly steady-state conditions. Thus, bandwidth is not a main concern, and the estimate can be low-pass filtered. The fact that the AFR estimator overestimates the AFR at at the lean-limit, can be accounted for in a feedback control law with sensor saturation.

The objective of closed-loop control of AFR during cold start is more complicated than during warmed-up conditions. During warmed-up conditions the AFR dependence of the conversion efficiency of the catalytic converter dictates that the AFR be kept in a narrow band about 14.7, in order for both oxidizing and reducing reactions to take place. During cold start, the objective of the closed-loop control should be to minimize the total amount of hydrocarbons emitted during the whole cold-start phase. It is not completely understood today how to achieve this optimum. The difficulty here is that the tail-pipe emissions depend on both the raw emissions from the engine, and on the state of the catalytic converter. Furthermore, the state of the catalytic converter is affected by the

exhaust that comes out of the engine.

To illustrate the complexity of the problem, two extreme cases can be considered. The first one is to keep the AFR during cold start at the level which minimizes the raw hydrocarbon emissions from the engine. Minimizing the raw hydrocarbon emissions from the engine will however slow down the heating of the catalytic converter, both through colder engine exhaust, and through less catalytic activity in the catalytic converter. The other extreme is to operate the engine rich during cold start, in order to minimize the time it takes for the catalytic converter to heat up to its normal operating temperature. This will produce high outputs of hydrocarbons during the initial stage of the cold start before the catalytic converter is hot, but allows faster transition to the normal stoichiometric operation of the engine, with high catalytic conversion efficiency. The optimum will be a trade-off between these two extremes, and will dictate a cold-start AFR trajectory which sacrifices some raw engine emissions in order to allow for faster heating of the catalytic converter, and consequently earlier transition to normal stoichiometric operation with high catalytic conversion efficiency.

6.8.2 Individual Cylinder Control

The proposed estimation technique is also valuable for estimating cylinder-specific AFR, which cannot be extracted from an exhaust gas oxygen sensor located in the exhaust manifold, where the exhaust from several cylinders is mixed. The intention is that the fuel and air delivery should be the same for all cylinders. In reality though, the difference in intake geometry for different cylinders cause differences in the air-flow rates through the intake ports. Also manufacturing tolerances and wear of fuel injectors can cause differences in fuel delivery characteristics between fuel injectors. For these reasons, the AFR may vary from cylinder to cylinder, which will result in different mechanical and thermal load on the different cylinders, as well as increased fuel consumption and exhaust emissions, and reduced mechanical power output.

Estimating cylinder-specific AFR using the proposed method, allows control of the AFR on all cylinders individually. One way to implement this is to use the existing oxygen sensor for overall engine AFR control using some existing method, and use the individual cylinder AFR estimates to balance out the differences between the cylinders. This could be

done by adding an integral term to the fuel delivery to cylinder i of the form

$$\int_0^t [(k-1)\mathrm{AFR}_i - \mathrm{AFR}_{j,1} - \ldots - \mathrm{AFR}_{j,(k-1)}]\mathrm{d}t \tag{6.37}$$

where k is the total number of cylinders and $\mathrm{AFR}_{j,1}, \ldots, \mathrm{AFR}_{j,(k-1)}$ represent the individual AFR estimates of the other cylinders. This should, in steady-state, equalize the AFR estimates for all cylinders. Here, by making the gain of the integral term small enough, the influence of the estimate variance can be made arbitrarily small.

Chapter 7

Concluding Remarks

7.1 Summary

7.1.1 Thermodynamic Modeling of Combustion in Internal Combustion Engines

A thermochemical model relating the progress of combustion in an internal combustion engine to the measured cylinder pressure has been derived. It has been shown that, particularly at high combustion temperatures, this model provides significant improvements to a heat release model without chemistry.

Different levels of simplifications to the model are suggested, in order to make the model more suitable for control purposes.

7.1.2 Cylinder-Pressure Offset Estimation

Two methods for estimating the sensor offset in cylinder-pressure measurements have been developed. Both are based on fitting the pressure measurements to a polytropic compression curve. The first method assumes a known polytropic exponent, and the second method estimates the polytropic exponent from the pressure measurements.

The first method is a generalization of the existing method in [41] where two pressure measurements during the pre-combustion compression are fitted to a polytropic compression curve with a known polytropic exponent. The linear least-squares fit presented here makes use of an arbitrary number of pressure measurements. It is also shown that the variance of the estimate drops as $1/n$ with the number of measurements n. A byproduct of

this method is an estimate of the cylinder pressure at the start of the computation crank-angle window. Its variance also, drops as $1/n$, which means that with many measurements a very accurate estimate of the intake pressure can be obtained.

The second method solves the nonlinear least-squares problem of estimating the polytropic exponent, as well as estimating the sensor offset and the intake pressure. The method separates the multivariable nonlinear least-squares problem into a linear least-squares problem, and a single-variable minimization problem. A finite-difference Newton method is derived, and its superlinear convergence properties are proved. Because of the excellent convergence properties of the minimization, the computational cost of solving the nonlinear least-squares problem is only slightly higher than the computational cost of solving the linear least-squares problem.

The method for solving the nonlinear least-squares problem is generally applicable to models of the form

$$y = \varphi(\kappa)\theta \tag{7.1}$$

where y is the output, θ is a vector of unknown parameters, and φ is a vector of regressors which depend nonlinearly on the unknown parameter κ. The only requirement on φ is that it is $\mathbb{C}^2$ with respect to κ, and that an analytic expression for $\mathrm{d}\varphi/\mathrm{d}\kappa$ is available. The general method is outlined in section 5.6.1.

7.1.3 Cylinder-Pressure Based AFR Estimation

A model for estimating cylinder AFR from cylinder-pressure measurements has been developed. It has the advantage of being based on physical models as opposed to black-box data correlation. Another advantage compared to present models is that the rapid-burn heat release rate, which is an important variable in the estimator, is proportional to the AFR, which means that the estimator is equally sensitive to changes in AFR for lean and rich operating points.

The estimator has been experimentally validated by comparing cycle-averaged steady-state AFR estimates over a range of engine operating conditions to measurements in the exhaust using a linear oxygen sensor. The RMS error of the cycle-averaged estimates is 4.1 %, which is somewhat better than the result obtain in [39] (4.85 %).

Using e.g. a moving average of AFR estimates, in order to reduce the variance, the proposed estimator could be used for feedback control of the cylinder AFR. This would allow

for cylinder-individual control of AFR, which is desirable since there are differences between individual fuel injectors and air-intake geometries. These differences result in different cylinders operating with different AFR, resulting in different mechanical and thermal load.

Using the pressure-based AFR estimates could also increase the bandwidth of a closed-loop AFR controller, since the exhaust transport delay from cylinder to oxygen sensor is removed. In present AFR control systems, this time delay results in severe lean excursions of the AFR when the throttle is opened suddenly, since it takes a while before the oxygen sensor reacts to the increased air flow. Similarly rich excursions result when the throttle is suddenly closed.

An additional application of the AFR estimator is during cold-starting conditions, when the exhaust gas is below the temperature requirement of the exhaust gas oxygen sensor. Presents cold-starting methods are open-loop methods and depend on well-calibrated components such as fuel injectors and intake manifold pressure sensors.

7.2 Future Work

7.2.1 Thermodynamic Modeling of Combustion in Internal Combustion Engines

The full thermochemical model should be verified using exhaust-gas analysis. The verification should be performed on an HCCI engine, since this is the engine type that most closely meets the homogeneity assumption. Crevice models, and heat transfer models should then be included as suggested in chapter 4.

7.2.2 Cylinder-Pressure Offset Estimation

In this work, the crank-angle measurements are assumed to be without error. Accurate crank-angle measurement requires accurate aligning of the crank-shaft encoder index with the top dead center of the engine. If the encoder axle is somehow deformed this alignment is destroyed. Incorporating the TDC offset into the estimator would make it immune to such deformation.

The TDC offset would enter as another nonlinear dependence in the nonlinear least-squares problem. Thus, the computationally efficient finite-difference Newton method cannot be used. An alternative is to estimate the TDC offset separately, assuming that the

polytropic exponent is known. Then the nonlinear dependence can be isolated to a one-variable minimization problem, and the finite difference Newton method can be applied.

7.2.3 Cylinder-Pressure Based AFR Estimation

This work does not verify the temperature dependence in the AFR model. By including intake-air heaters and coolers, the intake air temperature could be controlled, and the temperature dependence of the AFR estimate verified.

Development of more accurate flame speed models could reduce the variance of the AFR estimate. By doing so, the bandwidth of the estimator could be improved, since the estimate would not require as much filtering.

The estimator can provide feedback about the AFR during engine cold starting. This could be used for implementing a cold-start AFR trajectory, which minimizes the hydrocarbon emissions during cold starting. See section 6.8.1 for details.

Since the estimator provides cylinder-specific information about AFR, it could be used for controlling the individual AFR for each cylinder. An exhaust gas oxygen sensor can be used for the overall engine AFR control, using some existing method. The individual cylinder AFR control can then be implemented as integral control where the difference between the AFR of each cylinder and the average AFR of the other cylinders combined is integrated to provide an adjustment in the fuel injection for each cylinder.

Bibliography

[1] J. K. Ball et al. Combustion analysis and cycle-by-cycle variations in spark ignition engine combustion — part 1: an evaluation of combustion analysis routines by reference to model data. *Proceedings of the institution of mechanical engineers Part D— Journal of automobile engineering*, 212:(D5):381–399, 1998.

[2] N. C. Blizard and J. C. Keck. Experimental and theoretical investigation of turbulent burning model for internal combustion engines. *SAE Transactions*, 83, 1974. SAE Technical paper 740191.

[3] M. F. J. Brunt and A. L. Emtage. Evaluation of burn rate routines and analysis errors. SAE Technical Paper 970037, 1997.

[4] M. F. J. Brunt and C. R. Pond. Evaluation of techniques for absolute cylinder pressure correction. In *Spark-Ignition Engine Combustion and Emissions — SAE Special Publications*, volume 1267, pages 7–18, 1997. SAE Technical Paper 970036.

[5] M. F. J. Brunt, H. Rai, and A. L. Emtage. The calcutation of heat release energy from engine cylinder pressure data. SAE Technical Paper 981052, 1998.

[6] A. By and J. M. Rife. Knock in spark-ignition engines. SAE Technical paper 810147, 1981.

[7] J. E. Carryer et al. Estimating in-cylinder pre-combustion mixture temperatures using acoustic resonances. *Journal of Dynamic Systems Measurement and Control — Transactions of the ASME*, 118:(1):106–112, Mar 1996.

[8] C-F Chang et al. Engine air-fuel ratio control using an event-based observer. SAE Technical Paper 930766, 1993.

[9] C-F Chang et al. Air-fuel ratio control in spark-ignition engines using estimation theory. *IEEE Transactions on Control Systems Technology*, 3:(1):22–31, Mar 1995.

[10] D. Cho and J. K. Hedrick. A nonlinear controller-design method for fuel-injected automotive engines. *Journal of Engineering for Gas Turbines and Power — Transactions Of The ASME*, 110:(3):313–320, 1988.

[11] D. Cho and J. K. Hedrick. Sliding mode fuel-injection controller - its advantages. *Journal of Dynamic Systems Measurement and Control — Transactions of the ASME*, 113:(3):537–541, 1991.

[12] S-B Choi and J. K. Hedrick. An observer-based controller design method for improving air/fuel characteristics of spark ignition engines. *IEEE Transactions on Control Systems Technology*, 6:(3):325–334, 1998.

[13] L. Eriksson and L. Nielsen. Ionization current interpretation for ignition control in internal combustion engines. *Control Engineering Practice*, 5:(8):1107–1113, Aug 1997.

[14] R. Fletcher. *Practical Methods of Optimization, 2nd Edition*, pages 44–49. John Wiley and Sons, 1987. ISBN 0-471-91547-5.

[15] J. A. Gatowski et al. Heat release analysis of engine pressure data. *SAE Transactions*, 93, 1984. SAE paper 841359.

[16] J. C. Gilkey and J. D. Powell. Fuel-air ratio determination from cylinder pressure time histories. *Journal of Dynamic Systems Measurement and Control — Transactions of the ASME*, 107:(4):252–257, 1985.

[17] E. G. Groff and F. A. Matekunas. The nature of turbulent flame propagation in a homogeneous spark-ignited engine. SAE Technical Paper 800133, 1980.

[18] A. J. Haagen-Smit. Chemistry and physiology of Los Angeles smog. *Industrial and Engineering Chemistry*, 44:1342, 1952.

[19] John B. Heywood. *Internal Combustion Engine Fundamentals*. McGraw-Hill, 1988. ISBN 0-07-100499-8.

[20] S. D. Hires et al. Performance and NO_x emissions modelling of a jet ignition prechamber stratified charge engine. *SAE Transactions*, 85, 1976. SAE Technical paper 760161.

[21] S. D. Hires et al. The prediction of ignition delay and combustion intervals for a homogeneous charge, spark ignition engine. *SAE Transactions*, 87, 1978. SAE Technical Paper 780232.

[22] R. J. Hosey and J. D. Powell. Closed loop, knock adaptive spark timing control based on cylinder pressure. *Journal of Dynamic Systems, Measurement, and Control — Transactions Of The ASME*, 101:64–70, 1979.

[23] M. Hubbard et al. Closed loop control of spark advance using a cylinder pressure sensor. *Journal of Dynamic Systems, Measurement, and Control — Transactions Of The ASME*, pages 414–420, 1976.

[24] R. Johansson. *System modeling and identification*. Prentice-Hall information and system sciences series. Prentice Hall, Englewood Cliffs, NJ, 1993.

[25] V. K. Jones et al. Identification and air-fuel ratio control of a spark-ignition engine. *IEEE Transactions on Control Systems Technology*, 3:(1):14–21, Mar 1995.

[26] S. C. Kong. Modeling combustion in compression ignition homogeneous charge engines. SAE Technical paper 920512, 1992.

[27] J. E. Krier. *Pollution and Policy*. University of California Press, Berkeley, CA, 1977.

[28] P. Tunestål et al. In-cylinder measurement for engine cold-start control. In *Proceedings of the 1999 IEEE International Conference on Control Applications*, Aug 1999.

[29] P. Tunestål et al. Lean-limit control of a spark ignition engine using imep-based incomplete combustion detection. In *Proceedings of the Advanced Vehicle and Engine Control Conference*, 2000.

[30] D. R. Lancaster et al. Measurement and analysis of engine pressure data. *SAE Transactions*, 84, 1975. SAE Technical Paper 750026.

[31] A. Lecuona and P. A. Rodriguez. Evaluation of pressure and crank angle errors from reciprocating engine indicator diagrams. SAE Technical Paper 900170, 1986.

[32] W. E. Leisenring and S. Yurkovich. Comparative analysis of closed loop AFR control during cold start. In *Proceedings of the 1998 American Control Conference*, volume 3, pages 1377–1382, Philadelphia, PA, Jun 1998.

[33] S. Leonhardt et al. Methods for engine supervision and control based on cylinder pressure information. *IEEE Transactions on Mechatronics*, 4:(3):235–245, Sep 1999.

[34] X. Li and S. Yurkovich. I-c engine air/fuel ratio prediction and control using discrete-time nonlinear adaptive techniques. In *Proceedings of the 1999 American Control Conference*, pages 212–216, San Diego, CA, Jun 1999.

[35] M. Metgalchi and J. C. Keck. Burning velocities of mixtures of air with methanol, isooctane, and idolene at high pressure and temperature. *Combustion Flame*, 48:191–210, 1982.

[36] P. Najt and D. E. Foster. Compression-ignited homogeneous charge combustion. SAE Technical paper 830264, 1983.

[37] M. Noguchi et al. A study on gasoline engine combustion by observation of intermediate reactive products during combustion. *SAE Transactions*, 88:3, 1979. SAE Technical paper 790840.

[38] J-O Olsson et al. Experiments and simulation of a six-cylinder homogeneous charge compression ignition (hcci) engine. SAE Technical Paper 2000-01-2867, 2000.

[39] R. S. Patrick. *Air:Fuel Ratio Estimation in an Otto Cycle Engine: Two Methods and Their Performance*. PhD thesis, Stanford University, Jun 1989. Mechanical Engineering Department.

[40] J. D. Powell. Engine control using cylinder pressure — past, present, and future. *Journal of Dynamic Systems Measurement and Control — Transactions of the ASME*, 115:(2B):343–350, Jun 1993.

[41] A. L. Randolph. Methods of processing cylinder pressure transducer signals to maximize data accuracy. SAE Technical Paper 900170, 1990.

[42] G. M. Rassweiler and L. Withrow. Motion pictures of engine flames correlated with pressure cards. *SAE Transactions*, 38, 1938.

[43] M. C. Sellnau. Cylinder-pressure-based engine control using pressure-ratio-management and low-cost non-intrusive cylinder pressure sensors. SAE Technical Paper 2000-01-0932, 2000.

[44] R. A. Svehla and B. J. McBride. Fortran IV computer program for calcutation of thermodynamic and transport properties of complex chemical systems. NASA Technical Note TND-7056, 1973. NTIS number N73-15954.

[45] R. H. Thring. Homogeneous-charge compression-ignition (HCCI) engines. SAE Technical paper 892068, 1989.

[46] U.S. National Bureau of Standards. *JANAF Thermochemical Tables*, 2nd edition, Jun 1971. NSRDS-NB537.

[47] H. G. Vongarssen and V. Magori. A model-based senson for the adaptation of internal-combustion engines. *Sensors and Actuators — Physical*, 41:(1-3):207–211, Apr 1994.

[48] N. D. Whitehouse and B. K. Sareen. Prediction of heat release in a quiescent chamber diesel engine allowing for fuel air mixing. SAE Technical paper 740084, 1974.

[49] P. Wibberley and C. Clark. An investigation of cylinder pressure as feedback for control of internal combustion engines. SAE Technical Paper 890396, 1989.

[50] M. T. Wlodarczyk. In-cylinder fiber-optic pressure sensor for monitoring and control of diesel engines. SAE Future Transportation and Technology Conference, Costa Mesa, California, Aug 1998.

[51] M. T. Wlodarczyk et al. Embedded fiber-optic combustion-pressure sensors for advanced electronic engine control. In *Proceedings of Sensors Expo*, Detroit, MI, Oct 1997.

[52] G. Woschni. Universally applicable equation for the instantaneous heat transfer coefficient in the internal combustion engine. *SAE Transactions*, 76, 1967. SAE Technical paper 670931.

Appendix A

Symbols

A.1 Thermodynamics and Combustion

U	Internal energy
Q	Heat
W	Mechanical work
$\mathrm{d}U$	Internal energy differential (exact)
δQ	Infinitesimal heat
δW	Infinitesimal work
n	Number of moles
$\tilde{R}$	Universal gas constant
T	Temperature
p	Pressure
p_m	Measured cylinder pressure
Δp	Pressure sensor offset
$\tilde{c}_p$	Molar specific heat at constant pressure
$\tilde{c}_v$	Molar specific heat at constant volume
γ	Specific heat ratio
κ	Polytropic exponent
C	Polytropic constant $p_0 V_0^\kappa$
$\tilde{Q}_{LHV}$	Lower heating value of a fuel
$\mathrm{d}Q_{ht}$	Heat transfer to combustion chamber walls
$\tilde{u}$	Molar specific internal energy
h_c	Convective heat transfer coefficient
T_w	Cylinder wall temperature
w	Average cylinder gas velocity
ϕ	Fuel/air equivalence ratio

A.2 Geometry

A	Area
V	Volume
V_c	Clearance volume
V_d	Displacement volume
L	Engine stroke
B	Engine bore
a	Crank radius
l	Connecting rod length
s	Distance between piston bolt and crank center
z	Vertical piston position relative TDC

A.3 Engine Cycles

α	Crank angle
$\alpha_{10\%}$	Crank angle of 10% heat release
$\alpha_{50\%}$	Crank angle of 50% heat release
$\alpha_{90\%}$	Crank angle of 90% heat release
$\Delta\alpha_b$	Rapid-burning angle
$\Delta\alpha_d$	Flame-development angle
$\Delta\alpha_o$	Overall burning angle
$W_{c,i}$	Indicated work per cycle
$\tilde{Q}_{hr}$	Thermal energy release due to combustion (heat release)
$Q_{ch}(\alpha)$	Cumulative net heat release
Q_{min}	Minimum of $Q_{ch}(\alpha)$ over a cycle
Q_{max}	Maximum of $Q_{ch}(\alpha)$ over a cycle
Q_{tot}	Total net heat release $Q_{min} - Q_{max}$

A.4 Least Squares Analysis

φ	Regression vector
Φ	Regression matrix
θ	Parameter vector
$\hat{\theta}$	Least squares estimate of parameter vector
y	Measurement
Y	Measurement vector
D	Residual vector $Y - \Phi\theta$
P	Least squares projection matrix
J	Least squares loss function

A.5 Statistics

$E(\cdot)$	Expected value of random variable/vector
$\mathrm{Cov}(\cdot)$	Covariance matrix of random vector
$\mathrm{Var}(\cdot)$	Variance of random variable
σ	Standard deviation of random variable

A.6 Chemistry

$\mathbf{CO}$	Carbon monoxide
$\mathbf{CO_2}$	Carbon dioxide
$\mathbf{C_xH_y}$	Unspecified hydrocarbon fuel
x	Number of carbon atoms in hydrocarbon molecule
y	Number of hydrogen atoms in hydrocarbon molecule
$\mathbf{H_2O}$	Water
$\mathbf{O_2}$	Oxygen
$\mathbf{N_2}$	Nitrogen
$\mathbf{H_2}$	Hydrogen
$\mathbf{NO}$	Nitric oxide
$\mathbf{O}$	Oxygen radical
$\mathbf{H}$	Hydrogen radical
$\mathbf{OH}$	Hydroxyl radical

Appendix B

Abbreviations

AC	Alternate Current
AFR	Air/fuel-ratio
ATDC	After Top Dead Center
BTDC	Before Top Dead Center
DSP	Digital Signal Processor
EFI	Electronic fuel injection
EGO	Exhaust gas oxygen sensor
EHRD	Equivalent Heat Release Duration
EVC	Exhaust valve closing
EVO	Exhaust valve opening
FID	Flame Ionization Detector
IC	Internal combustion (engine)
ISA	Industry Standard Architecture
IVC	Intake valve closing
IVO	Intake valve opening
HCCI	Homogeneous charge compression ignition
MBT	Maximum Brake Torque (ignition timing)
RPM	Revolutions Per Minute (engine speed)
TDC	Top dead center (piston position)
TTL	Transistor-Transistor Logic
TWC	Three-way catalytic converter